

2005 FIELD TESTS OF ALLTEM AND THE PLANAR TENSOR MAGNETIC GRADIOMETER SYSTEM (TMGS) AT THE STANDARDIZED UXO TEST AREA AT THE YUMA PROVING GROUND, ARIZONA

SERDP Project MM-1328

April 1, 2006

U.S. Geological Survey

(David L. Wright, David vonG. Smith, Theodore H. Asch, Charles P. Oden)

and

Colorado School of Mines, Department of Geophysics

(Yaoguo Li, Misac N. Nabighian, Vinicio Sanchez)



ALLTEM on the Calibration Grid at YPG



TMGS on the Calibration Grid at YPG



Report Documentation Page				Form Approved OMB No. 0704-0188	
Public reporting burden for the collection of information is estimated to average 1 hour per response, including the time for reviewing instructions, searching existing data sources, gathering and maintaining the data needed, and completing and reviewing the collection of information. Send comments regarding this burden estimate or any other aspect of this collection of information, including suggestions for reducing this burden, to Washington Headquarters Services, Directorate for Information Operations and Reports, 1215 Jefferson Davis Highway, Suite 1204, Arlington VA 22202-4302. Respondents should be aware that notwithstanding any other provision of law, no person shall be subject to a penalty for failing to comply with a collection of information if it does not display a currently valid OMB control number.					
1. REPORT DATE 01 APR 2006		2. REPORT TYPE		3. DATES COVERED 00-00-2006 to 00-00-2006	
4. TITLE AND SUBTITLE 2005 Field Tests of Alltem and the Planar Tensor Magnetic Gradiometer System (TMGS) at the Standardized UXO Test Area at the Yuma Proving Ground, Arizona				5a. CONTRACT NUMBER	
				5b. GRANT NUMBER	
				5c. PROGRAM ELEMENT NUMBER	
6. AUTHOR(S)				5d. PROJECT NUMBER	
				5e. TASK NUMBER	
				5f. WORK UNIT NUMBER	
7. PERFORMING ORGANIZATION NAME(S) AND ADDRESS(ES) U.S. Geological Survey,M.S. 964, Box 25046, Federal Center,Denver,CO,80225				8. PERFORMING ORGANIZATION REPORT NUMBER	
9. SPONSORING/MONITORING AGENCY NAME(S) AND ADDRESS(ES)				10. SPONSOR/MONITOR'S ACRONYM(S)	
				11. SPONSOR/MONITOR'S REPORT NUMBER(S)	
12. DISTRIBUTION/AVAILABILITY STATEMENT Approved for public release; distribution unlimited					
13. SUPPLEMENTARY NOTES					
14. ABSTRACT					
15. SUBJECT TERMS					
16. SECURITY CLASSIFICATION OF:			17. LIMITATION OF ABSTRACT Same as Report (SAR)	18. NUMBER OF PAGES 132	19a. NAME OF RESPONSIBLE PERSON
a. REPORT unclassified	b. ABSTRACT unclassified	c. THIS PAGE unclassified			

This report was prepared under contract to the Department of Defense Strategic Environmental Research and Development Program (SERDP). The publication of this report does not indicate endorsement by the Department of Defense, nor should the contents be construed as reflecting the official policy or position of the Department of Defense. Reference herein to any specific commercial product, process, or service by trade name, trademark, manufacturer, or otherwise, does not necessarily constitute or imply its endorsement, recommendation, or favoring by the Department of Defense.

TABLE OF CONTENTS

PREFACE.....	Page 3
1.0 INTRODUCTION.....	Page 4
2.0 THE REVISED CALIBRATION GRID AREA AT YPG.....	Page 5
3.0 ALLTEM DATA AND ANALYSIS.....	Page 12
4.0 ALLTEM MODELING AND INVERSION.....	Page 45
5.0 TMGS DATA AND ANALYSIS	Page 63
6.0 TMGS MODELING AND INVERSION.....	Page 101
7.0 CONCLUSIONS AND RECOMMENDATIONS.....	Page 101
8.0 REFERENCES.....	Page 104
9.0 APPENDIX	Page 105

PREFACE

ALLTEM is a new system designed, in part, based on modeling and, in part, by observations of results from VETEM and the High Frequency Sounder. The triangle current wave excitation was recommended by Misac Nabighian. Craig Moulton carried the major responsibilities for making the ALLTEM system actually happen. He designed, built, and tested the electronics with assistance from Raymond Hutton and Roy Kipfinger. Craig also wrote the data acquisition software in LabVIEW including transmitter and receiver control, real-time data visualization, incorporation of GPS data into the data stream, recording, playback, and data preprocessing. John D. Kibler built the cart.

The TMGS planar geometry is new. The design was done by David V. Smith with assistance from Robert Bracken. Carl Stoddard fabricated the fluxgate mounts. Ray Hutton carried much of the responsibility for the entirely new, and much faster, data acquisition system with support from Roy Kipfinger and Philip Brown. Dave Smith, Rob Bracken and Phil Brown have all been involved with the challenges of deriving sufficiently accurate calibration coefficients so that meaningful tensor measurements can be derived from the TMGS raw data.

Because these systems produce data in unique formats and in prodigious quantities, and because methods appropriate for processing the UXO data from YPG were not all in place, the data processing was an immense accomplishment. Phil Brown has developed some of these methods and has converted ALLTEM data into formats that could be entered into OASIS Montaj to take advantage of some of the features of that software which is widely used in the UXO community. Dave Smith has done parallel work with the TMGS data.

To field prototype geophysical instruments of the level of complexity and sophistication of ALLTEM and the Tensor Magnetic Gradiometer System (TMGS) is difficult. The team that conducted the work described in this report consisted of engineers and geophysicists of various backgrounds. Various team members were associated more with one system than others and different sections in this report were written mainly or entirely by various individuals and this is reflected by variations in style, format, and chosen content in the various sections of the report.

We are grateful for the collaboration of our colleagues at the Colorado School of Mines, Drs. Yaoguo Li, Misac Nabighian and Mr. Vinicio Sanchez. CSM has delivered a magnetic inversion code to the USGS. In addition, Dr. Charles P. Oden, a recent Ph.D. from CSM, is working at the USGS on a new algorithm to perform inversions of ALLTEM data. It is close to completion and testing on field data (April 1, 2006).

Although the bulk of this report is occupied with results from the tests at Yuma Proving Ground, we also include preliminary conclusions and suggested directions for future development.

2005 FIELD TESTS OF ALLTEM AND THE PLANAR TENSOR MAGNETIC GRADIOMETER SYSTEM (TMGS) AT THE STANDARDIZED UXO TEST AREA AT THE YUMA PROVING GROUND, ARIZONA

1.0 INTRODUCTION

The Strategic Environmental Research and Development Program (SERDP) sponsored the tests discussed in this report under Project MM1328. The starting point for this project was three existing geophysical prototype instruments developed by the U.S. Geological Survey (USGS) for other applications. Although none of the prototypes was developed with UXO applications in mind, it was thought that with some modifications each of the prototype instruments could detect UXO objects. This expectation was tested by operation at the Yuma Proving Ground (YPG) standardized UXO test area in 2003. Based on evaluation of the data from those tests, we recommended that a new electromagnetic induction (EMI) system be designed and built and that the geometry and data acquisition system for the TMGS be replaced. This report deals with results and evaluations from the first field deployments of ALLTEM and the planar TMGS. The tests described in this report were conducted in October and November of 2005. A summary of our daily activities is included in Table 1.1.

Section 2 of this report describes characteristics of the standardized UXO test site at YPG relevant to our tests. Sections 3 and 4 describe the ALLTEM tests and modeling. Sections 5 and 6 describe the TMGS. Section 7 includes some conclusions and recommendations derived largely from the 2005 YPG tests.

Date	Day	Field Activity
Oct 17	Monday	Drive from Denver to Albuquerque, NM.
Oct 18	Tuesday	Drive from Albuquerque, NM to Phoenix, AZ.
Oct 19	Wednesday	Drive from Phoenix, AZ to YPG; Trailer tire blew when entering gate (cut?) Got badges, changed trailer tire. YPG safety training. Unload equipment and begin site & ALLTEM system setup.
Oct 20	Thursday	ALLTEM: Cont. ALLTEM setup. Setup GPS; First static system calibrations; Adjusted loop null offsets. Begin data acquisition in Cal. Grid; Adjust towing speed; Ran NS and SN lines over steel ball to calibrate GPS position offsets and latency.
Oct 21	Friday	ALLTEM: Acquire ALLTEM data in Cal Grid starting in SW corner surveying south to north every 0.5 m with data density along line of ~20 cm.; Had to stop at line 12 to replace sheared wheel bolts. ~ 1 hour loss. Recording Hz (vertical) channels.
Oct 22	Saturday	ALLTEM: No Field Work; Work on data; Replace two (1 blowout and 1 worn) tires on transport trailer.
Oct 23	Sunday	ALLTEM: No Field Work; Process data acquired to date. Compare 21-stack and 12-stack data – not a great difference. Also 20-25 cm spatial data density judged adequate for 1 m loops.
Oct 24	Monday	ALLTEM: Calibration files and begin Calibration Lanes using Hy (across track) excitation polarization. Some GPS dropouts. Some wheel bearing replacements required.

Oct 25	Tuesday	ALLTEM: Cal. Files and finish Hy lines on Calibration Grid.
Oct 26	Wednesday	ALLTEM: Tried switching, but something wrong – data corrupted. Changed amplifier channel and abandoned switching. Went to Hx (along track) excitation polarization. Lost time because front wheel bearings had disintegrated damaging front axle. Replaced axle and bearings. Numerous GPS drop-outs.
Oct 27	Thursday	ALLTEM: Tic Tac Toe over and 81 mm target.
Oct 28	Friday	ALLTEM: Tic Tac Toe over 60 & 20 mm targets. TMGS: Crew arrives; badges; safety training; unpack & inspect gear.
Oct 29	Saturday	ALLTEM: “Racetrack” over entire Calibration Grid – Multiplexed Tx switching mode now working. Last day for ALLTEM. TMGS: Equipment checks; G-858 recon for magnetically clean area.
Oct 30	Sunday	TMGS: No Field Work; TMGS data processing Software.
Oct 31	Monday	TMGS: G858 recon for Spin Calibration location.
Nov 1	Tuesday	TMGS: High-resolution survey of Spin Cal location; erect Spin Cal apparatus and test.
Nov 2	Wednesday	TMGS: Conduct Spin Calibrations.
Nov 3	Thursday	TMGS: Conduct Spin Calibrations.
Nov 4	Friday	TMGS: Conduct Spin Calibrations.
Nov 5	Saturday	TMGS: Mount TMGS on prime mover/ platform. Perform calibration and interference tests with tractor tow bar.
Nov 6	Sunday	TMGS: No Field Work: Process test data, plan week’s activities.
Nov 7	Monday	TMGS: G-858 survey of Cal Grid; tractor self-signature tests.
Nov 8	Tuesday	TMGS: Cal Grid survey south to north lines at 1m spacing
Nov 9	Wednesday	TMGS: High Density grid in Lane 8 over same 81 mm target (H08) as ALLTEM.
Nov 10	Thursday	TMGS: No Field Work: Base holiday; process data
Nov 11	Friday	TMGS: No Field Work: Base holiday; process data
Nov 12	Saturday	TMGS: No Field Work: Base holiday; process data
Nov 13	Sunday	TMGS: Process data; plan upcoming activities.
Nov 14	Monday	TMGS: High Density grid in Lane 8 over same 60 mm target (H08) as ALLTEM; latency and lag tests along radial lines over magnet.
Nov 15	Tuesday	TMGS: High Cal Grid survey south to north lines at 1m spacing, offset 0.5 m from Nov 8 survey; high-resolution survey over 20 mm target.
Nov 16	Wednesday	Drive Yuma, AZ to Benson, AZ
Nov 17	Thursday	Drive Benson, AZ to Santa Fe, NM
Nov 18	Friday	Drive Santa Fe NM to Denver, CO Arrive DFC. Stow gear.

Table 1.1. USGS Yuma Proving Ground Field Itinerary, Oct-Nov, 2005

2.0 THE REVISED CALIBRATION GRID AREA AT YPG

Figure 2.1 shows the location of YPG. Figure 2.2 shows the location of the UXO test area and the location within the test area of various grids.

2.1 Soil Properties

soil electrical conductivity influenced VETEM and HFS measurements in 2003 because both instruments were designed to respond to changes in electrical conductivity. Soil magnetic susceptibility affected the TMGS and possibly ALLTEM in 2005. Figure 2.1.

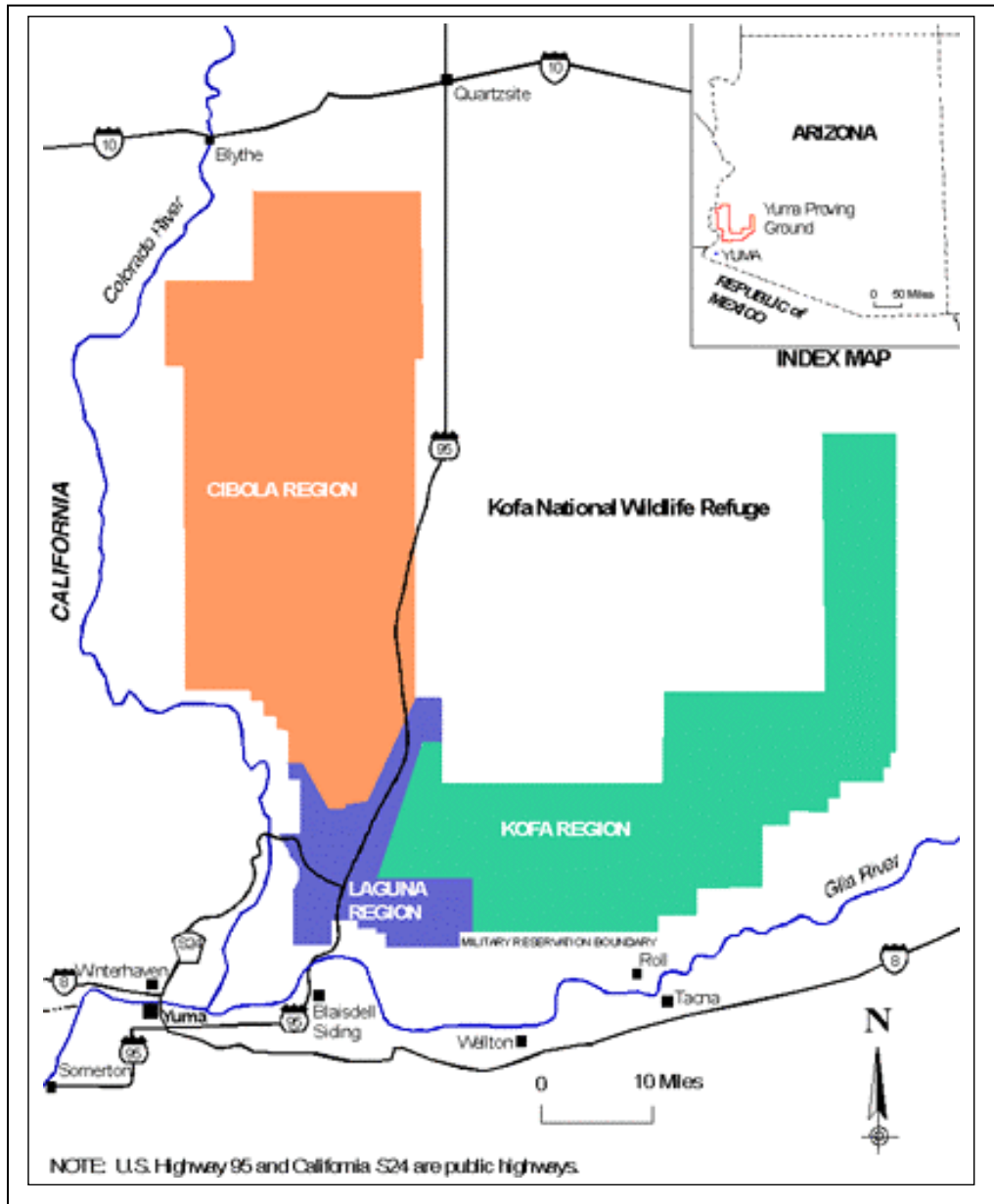


Figure 2.1. Location of YPG. The standardized UXO test area is in the Kofa region.

measurements as well. Figure 2.3 shows a map of natural magnetic anomalies. Table 2.1 is a summary of soil properties measured from samples collected by the USGS at the time of our 2003 tests. The samples were taken close to, but not on, the Calibration Grid.

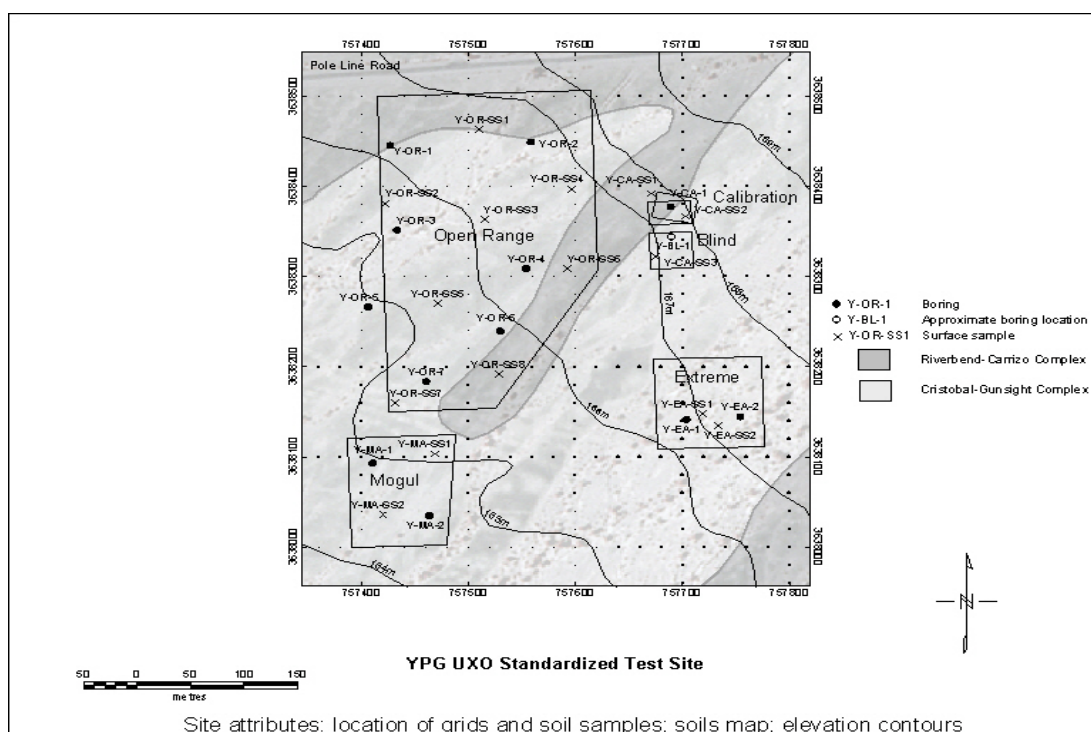


Figure 2.2. The YPG UXO Standardized Test Site contains several areas including the Calibration Grid, Blind test Grid, Mogul Area, Extreme Area, and Open Range Area. We conducted tests only in the Calibration Grid. As indicated on the map, the initial planned layout of the Calibration Grid, aligned with true north, was modified by a rotation about the SE corner to align the grid with magnetic north.

Smectite-water interactions are the probable cause of the high dielectric permittivity observed in the “as received” X-ray diffraction (XRD) data indicate that the samples contain 3 clay minerals; smectite, kaolinite and illite. Although the XRD technique is not highly quantitative, it appears kaolinite is the dominant clay mineral but is still only a minor component of the soil. Smectite and illite are present in lesser amounts.

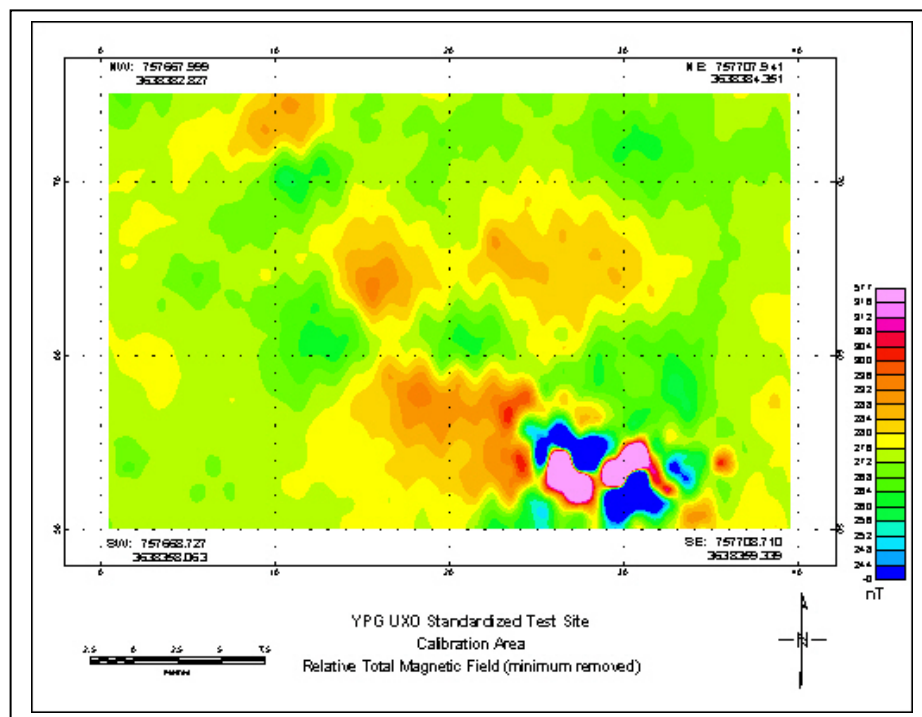


Figure 2.3. Background total magnetic field map of the Calibration Area prior to UXO object emplacement. Map courtesy of the U.S. Army.

The range of electrical conductivities (resistivities) obtained by the U.S. Army over the Calibration Area with the EM-38 is about 15 mS/m (66 ohm-m) to 5.7 mS/m (175 ohm-m) measured at the EM-38 frequency (the standard EM-38 frequency is 14.6 kHz). The USGS laboratory measurements of samples S02 and S03 in “as received” condition are consistent with the EM-38 values although measured at different frequencies. Sample S01 was notably lower in water content and correspondingly higher in resistivity than the other two samples. It might be noted that shortly prior to our use of the site in 2003 there had been an unusual amount of rain on the site. This was followed with even more rain on February 25 while we were there. The added water could only increase the soil conductivity. The samples we took were from near the surface. Conductivity at depth could be higher as was noted at another site at YPG in 1993. At that undisclosed location on YPG the surface resistivities were > 1000 ohm-m while from 20 to 50 cm depth an increase in water and clay content was observed with electrical resistivity dropping to tens of ohm-m or less (Olhoeft and others, 1994).

Yuma Electrical Properties “As Received”

Sample	Resistivity (ohm-m)		Dielectric Permittivity		Water weight percent
	100 Hz	10 MHz	100 Hz	10 MHz	
S01	1.93 X10 ⁵	922	330	3.5	1.7
S02	318	112	3.0 X 10 ⁴	4.3	4.7
S03	131	63	7.3 X 10 ⁴	-	5.5

Yuma Electrical Properties Oven Dried (105°C at 760 torr)

Sample	Resistivity (ohm-m)		Dielectric Permittivity	
	100 Hz	10 MHz	100 Hz	10 MHz
S01	1.06 X10 ⁸	1.07 X10 ⁴	3.9	2.5
S02	1.59 X10 ⁸	1.54 X10 ⁴	3.1	1.9
S03	9.29 X10 ⁷	1.40 X10 ⁴	4.2	2.5

Yuma Magnetic Susceptibility Measurements (1040Hz)

Sample	As Received		Oven Dried	
	10 ⁻⁶ cgs	n	10 ⁻⁶ cgs	n
S01	13.4	7	14.7	5
S02	13.7	6	14.4	4
S03	15.5	5	13.4	4
Average	14.1	18	13.9	13
Pebbles	13.1	3		

n= number of measurements

Table 2.1. This table summarizes measurements of electrical and magnetic properties of three soil samples collected near the Calibration Area at YPG. The electrical resistivity (reciprocal of conductivity) at 100 Hz is reduced by almost six orders of magnitude by the addition of 5.5% weight percent water. (Measurements by Robert J. Horton, USGS).

Some of the 1993 samples from the undisclosed YPG location were reported to have high magnetic permeability and consequent high losses for ground penetrating radar. However, the samples we obtained and measured at the Calibration Area showed little magnetic susceptibility.

The magnetic field over the site was measured by the Army with a Geometrics-858 magnetometer and showed background variations of 20 to 30 nT for the most part except for a few anomalies that had amplitudes of almost 600 nT. Except for buried objects the soil magnetic susceptibility would control the spatial variations in the measured magnetic field. The values of soil magnetic susceptibility we measured in the laboratory are all close together and low.

2.2 Reconfigured Calibration Lanes

Because of the natural magnetic anomaly seen in Figure 2.3, targets were removed from that area and placed on the west side of the Calibration Grid

Figures 2.4 and 2.5 show the reconfigured Calibration Lanes. Data courtesy U.S. Army.

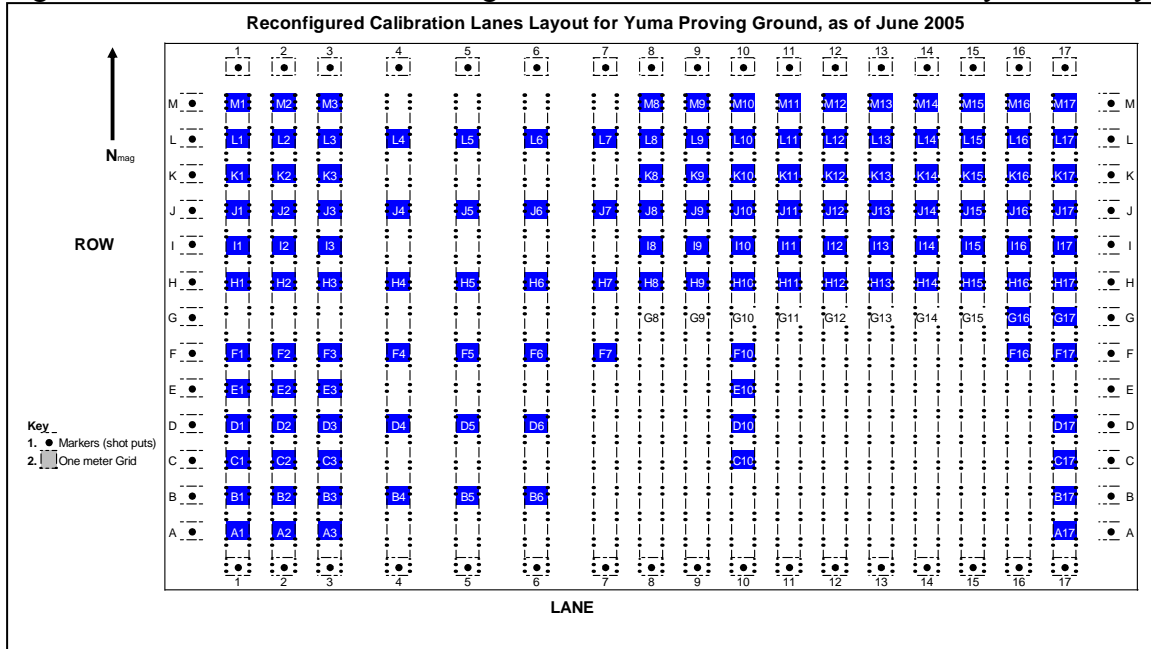


Figure 2.4. Reconfigured Calibration Lanes.

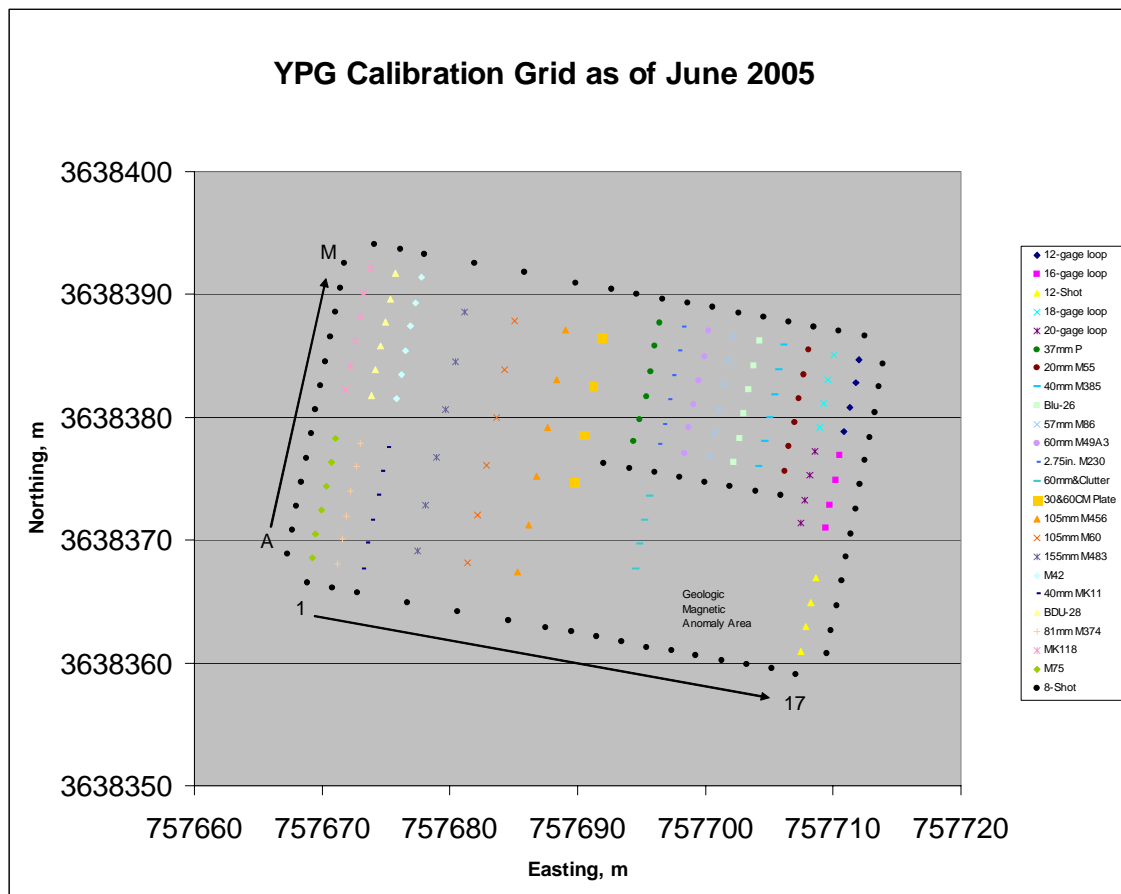


Figure 2.5 Target identities in the reconfigured Calibration Grid.

3.0 ALLTEM DATA AND ANALYSIS

The daily log of activities for ALLTEM is included in Table 1.1 above. The main divisions of our work with ALLTEM were (1) initial set-up and primary field nulling, (2) repetitive calibrations, (3) a survey over the entire Calibration Grid with H_z (vertical) magnetic field excitation, (4) a survey over the entire Calibration Grid with H_y (across-track) magnetic field excitation, (5) a survey over the entire Calibration Grid with H_x (along-track) magnetic field excitation, (6) high-density (tic tac toe) grids over a 60 mm target, and 81 mm target, and a 20 mm target, (7) a final run over the entire Calibration Grid while multiplexing through H_z , H_y and H_x excitation polarizations. We plan to do the Blind Test Grid using this multiplexing mode of operation during our next deployment.

3.1 Coil Primary Field Nulling

Because one of the transmitting coils (H_x , H_y , or H_z axis) is always on, except for brief switching intervals when multiplexing, we operate various combinations of receiving (Rx) coils as gradiometers to remove the primary field. Because this primary field is orders of magnitude larger than signals from the targets of interest, and because it is difficult to exactly cancel the primary field by mechanical position adjustments alone, we opted to electronically adjust the outputs of various coils in pairs so that the primary is cancelled as precisely as possible. Figure 3.1 shows how this was done as the first step in our ALLTEM YPG work. We elevated the cube in order to reduce any ground response, adjusted potentiometers for various coil pairs, and then left these settings the same for the duration of our testing, except for the last day's operation.



Figure 3.1. ALLTEM cube elevated for coil primary field nulling.

3.2 System Calibrations

In laboratory measurements of our system we identified electronic drifts from two sources, but these were largely stable within about 15 minutes. One additional source of drift is apparently expansion and contraction of the copper in the transmitter coil windings with temperature. We potted the windings to minimize movement, but cannot entirely eliminate thermal expansion. This drift is slower and may have a time constant of about 45 minutes to an hour. The coils may be heated from three sources: (1) electrical current driven through the windings, (2) ambient air temperature, (3) solar heating. It was our practice to turn the system on and let it run for at least 15 minutes before taking data except calibration files. At least at the beginning and end of each day's data collection we reoccupied a given location and ran the system in three ways: with no target, with a brass sphere, and with a steel sphere, each placed above the cube on a rigid plastic mount. This enables us to assess the drift of several channels at once. Figure 3.2 shows placement of one of the spheres for a calibration run.



Figure 3.2. Ted Asch placing a steel sphere on top of the ALLTEM cube for a static system calibration.

Standardization tests were conducted prior to all ALLTEM data collection events. An electromagnetically quiet test site was located on the pad just west of the YPG Calibration Grid. ALLTEM standardization testing included both static and dynamic testing. Static test data measurements were made in the morning and afternoon before and after each production survey. After the system was allowed to warm up for 15 to 30 minutes, approximately 100 static measurements over background geology were recorded. Examples of morning and afternoon static background standardization data are shown in Figure 3.3. These data, recorded on October 21, show a very large system shift. We may have had some electronic problems on that day, or the AM data may have been recorded before adequate system warm up was completed. High frequency coherent noise is also observed. This noise component disappears when the PMCal data and AMCal data are differenced.

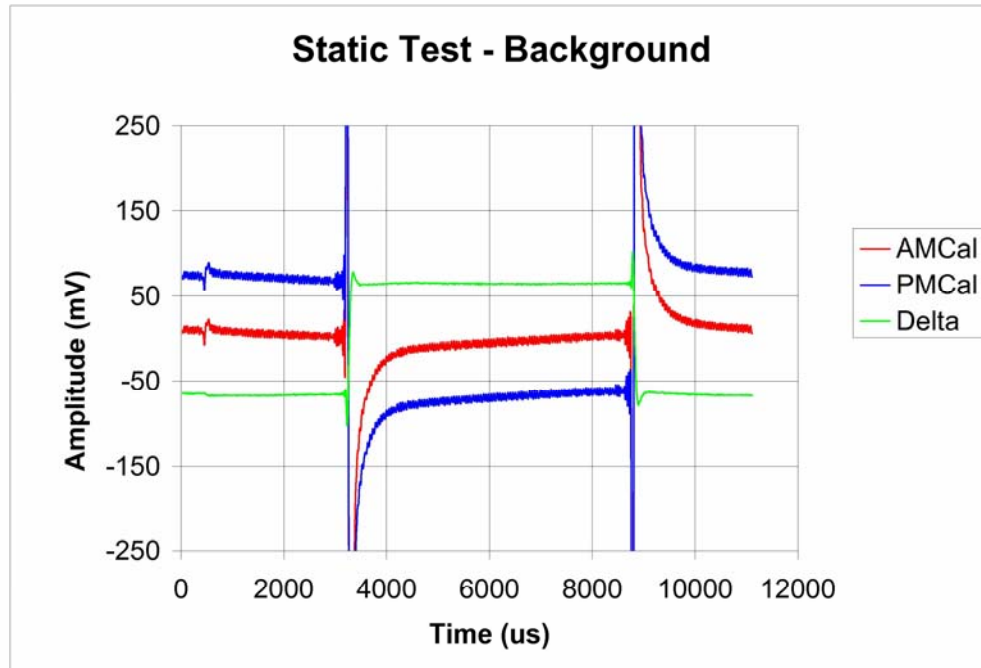


Figure 3.3 Background morning and afternoon static measurements and the difference (delta) between them on October 21, 2006. Large shifts (~ 60 mV) occurred that day.

After background measurements were completed, two more sets of 100 measurements were made with standardization targets. The ALLTEM standardization targets are 4-inch brass and steel spheres. Each sphere is placed on a PVC pipe 17-inches above the ALLTEM (Figure 3.4) and 100 measurements are recorded.

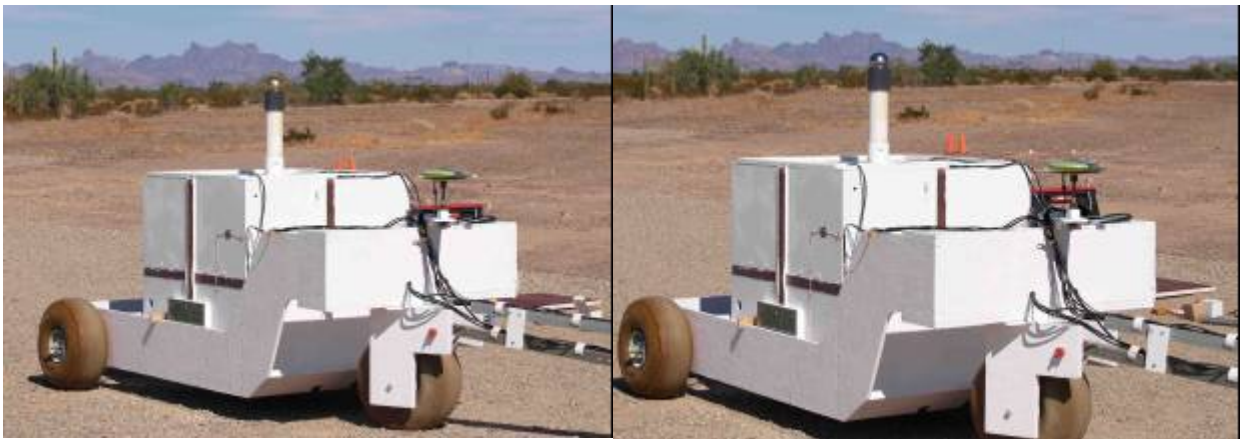


Figure 3.4 ALLTEM static standardization measurements for brass and steel spheres.

Examples of the metal sphere static measurements are presented in Figure 3.5. Note the differences in the decay slopes for the brass and steel compositions. The response for the steel sphere is decaying faster than for the sphere composed of brass.

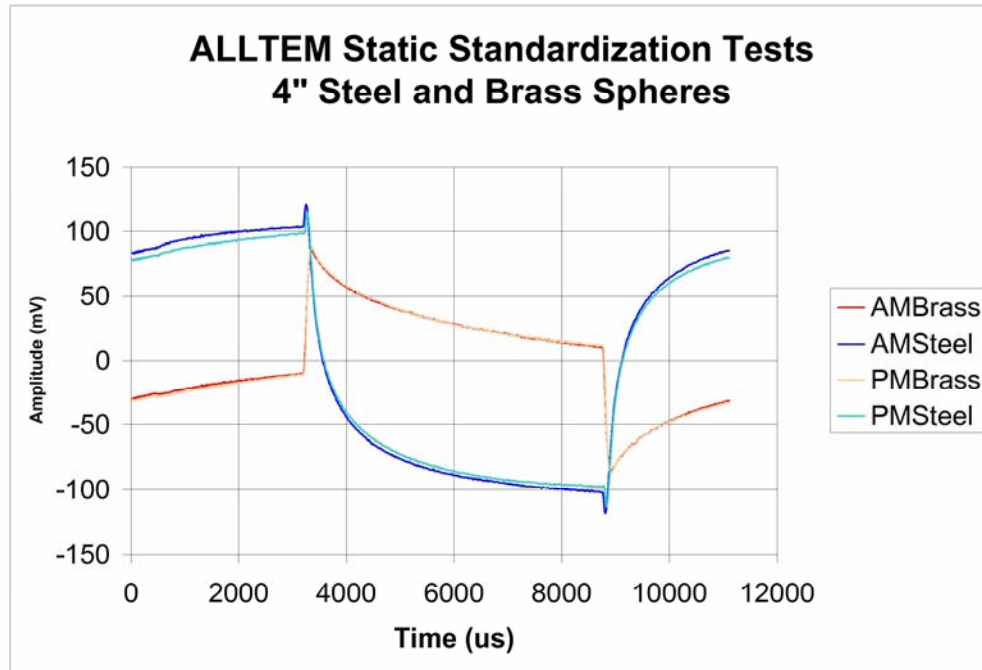


Figure 3.5 ALLTEM static standardization measurements for the brass and steel spheres. These measurements were made on Oct. 27 and show much reduced variation (~ 5 mV maximum) from those on Oct. 21.

Dynamic measurements to check GPS positioning were also conducted with the ALLTEM. This test consisted of burying an 8 lb. steel shot (the same as are in the Calibration Grid) just below the surface. The ALLTEM was then driven over the target at fast and slow speeds and then several runs were conducted with the ALLTEM approaching from different azimuths. A rope was laid out on the ground as a baseline azimuth (**Figure 3.6**). We do not show results from these tests in part because we had so many problems with the JAVAD GPS that we have decided to abandon use of that system in favor of the Leica 1200 GPS in the next deployment. We do not think this will solve all problems, but it should help. See our discussion in Sections 5.7 and 7.1.



Figure 3.6 ALLTEM Dynamic GPS standardization testing.

Navigation

Positioning and navigation for the ALLTEM utilized a JAVAD Legacy-E system. Data density along the traverses were nominally 20-25 cm which resulted in a location accuracy of approximately ± 25 cm. The TMGS utilized a LEICA 1200 Differential GPS system.

3.3 H_z Excitation Survey Results

The first runs over the Calibration Grid were done while driving the horizontal coil, producing a vertical (on axis) magnetic field. While driving this coil there were five simultaneous channels recorded, all vertical gradients. One was from a 1 m vertical gradient coil pair and the other four from four 34 cm vertical gradient coil pairs. As configured at YPG it was not possible to record horizontal gradients while the vertical field Tx coil was operating. We are currently modifying the system to permit this. An example of leveled amplitude data is shown in Figure 3.3.

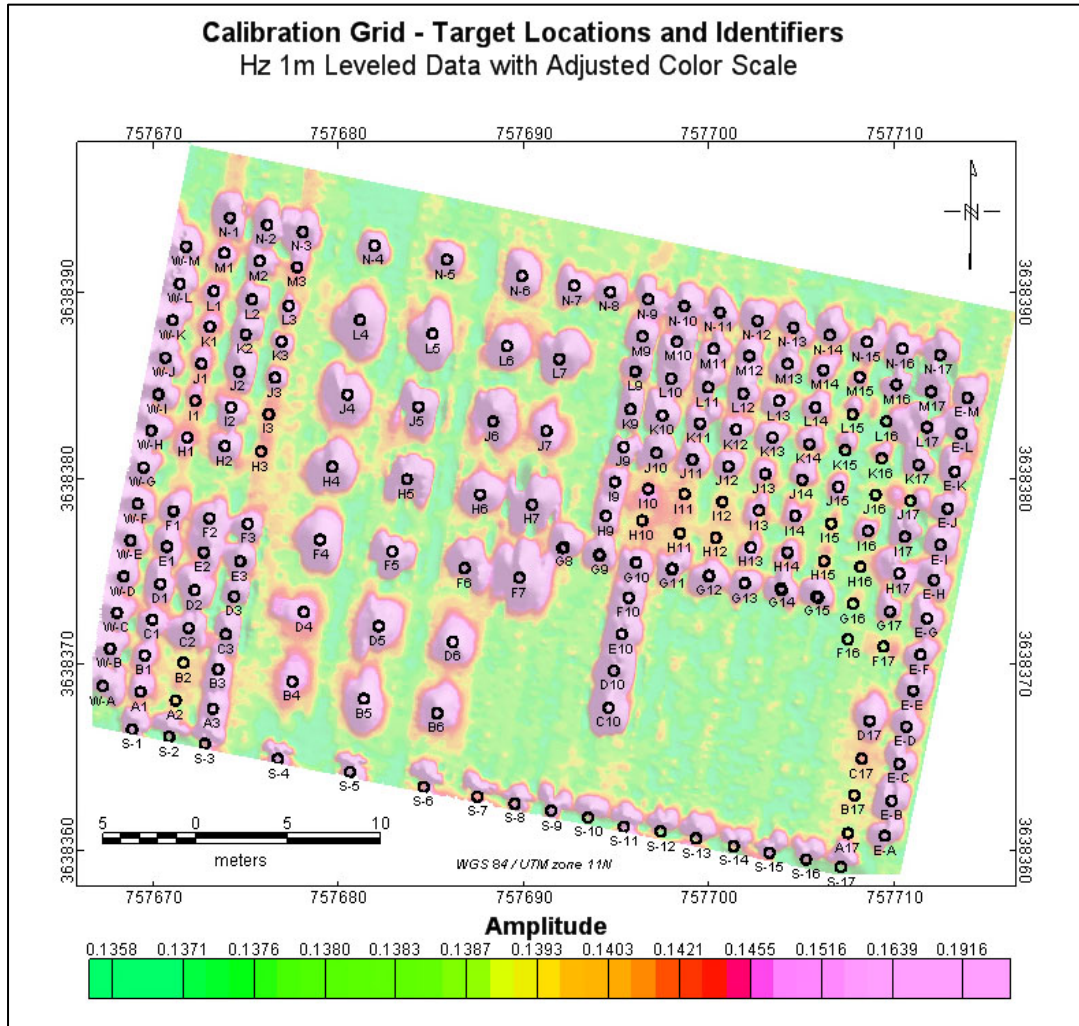


Figure 3.3. This amplitude difference map is produced from data recorded on the 1 m vertical gradient Rx coils when the vertical magnetic field Tx is driven. The data have been leveled and the color table adjusted to show the targets to good advantage. The target locations are shown by the open black circles and the target grid locations are indicated. It is clear that all but a few targets are detected.

A map of the raw data from which Figure 3 is derived is included in the draft paper in the appendix of this report.

3.4 H_y Excitation Survey Results

Our convention is that “y” is horizontal and perpendicular to the line direction. When the excitation is in either of the two horizontal directions we can record and examine both the corresponding horizontal spatial gradient and the vertical gradient. In Figure 3.4 we show an example map of the received vertical gradient when the H_y field is driven.

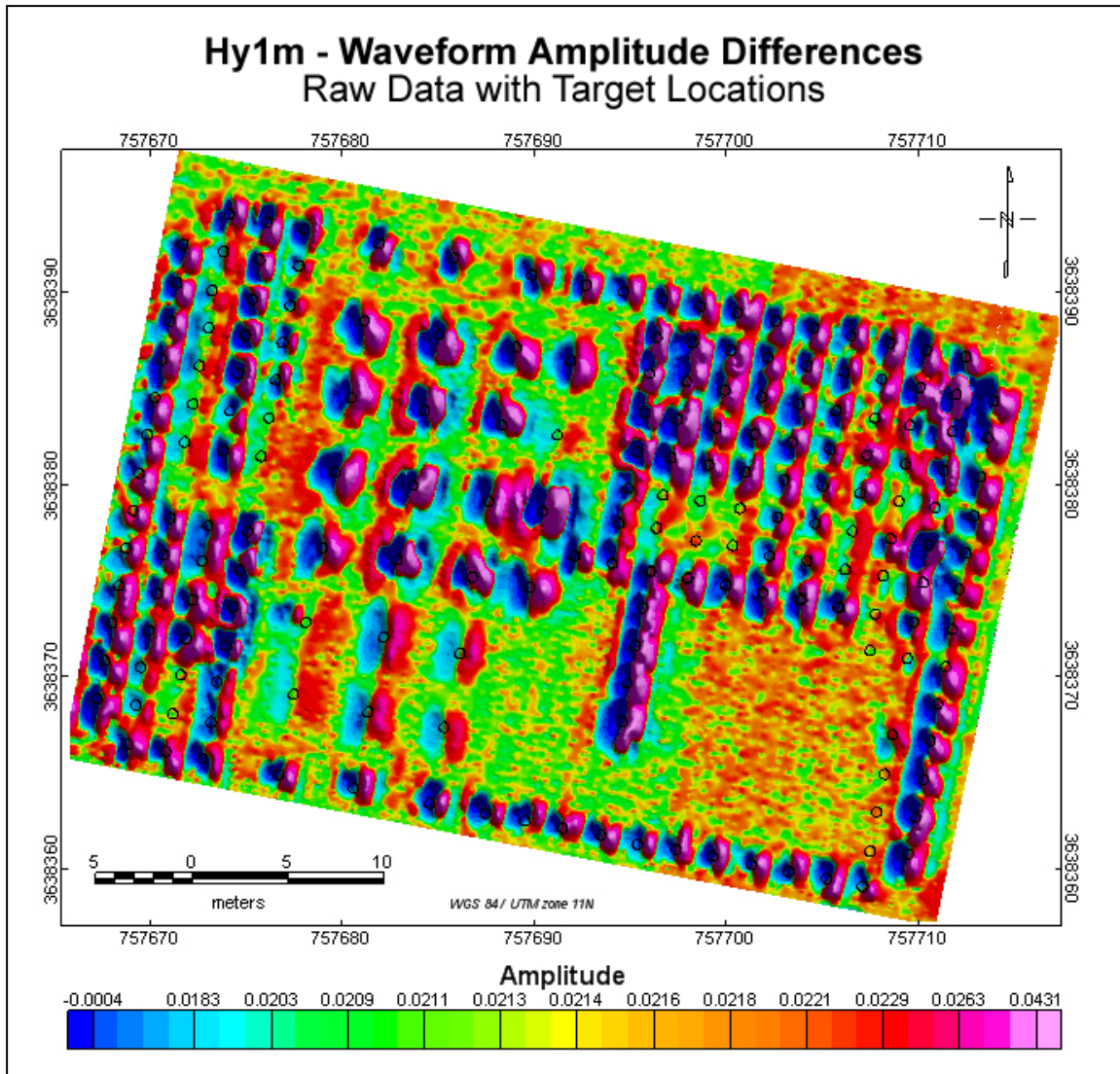


Figure 3.4. This is a raw data map when the Tx field is across track and the vertical gradient is recorded. For spherical and axially symmetric targets oriented vertically or along the traverse, the target location should be at a transition between positive and negative values. Note that the amplitude differencing we have done results in a DC shift that we have not removed, but the indicated target locations do generally fall on a color transition.

Combinations of data from different excitation polarizations and received gradient polarizations, in concert with time decay measurements, may assist in target identification and discrimination. Targets that are difficult to detect either because they are small or because they are deep may be observable only in some polarizations.

Figure 3.5 shows an example map when the excitation is in the cross-track direction and the horizontal derivative is being observed.

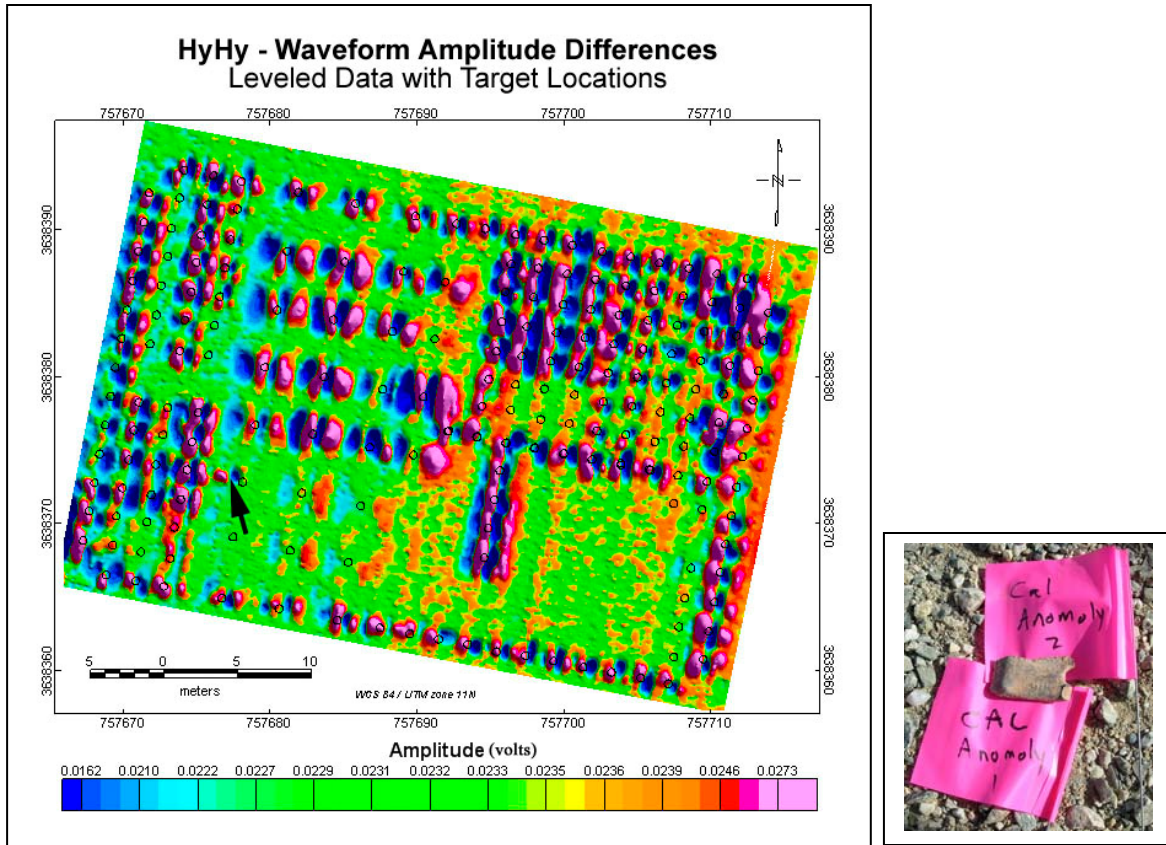


Figure 3.5. An example map when the driving field is in the y, across track, direction and the horizontal gradient in the y direction is being measured. We found evidence of an undocumented target on the Calibration Grid in this map (black arrow). This was confirmed by Rick Fling, Army Environmental Center. The undocumented target was found very close to the location positions we had supplied. The object was part of a broken backhoe bucket tooth shown at right.

3.5 H_x Excitation Survey Results

Figure 3.6 shows an example of raw data taken with the excitation in the along track, x, direction, and the x direction horizontal gradient is measured. Some of the deep 155 mm targets at locations B4 and D4, for example (see Figure 3.2), have higher amplitude when illuminated and observed in the x direction, rather than the y direction which is consistent with their orientation along the direction in which the lines were run, i.e. the “x” direction. The map of Figure 3.6 clearly has some position issues. This shows up in “splitting” of the target signatures and field patterns that are not perpendicular to the lines as they should be.

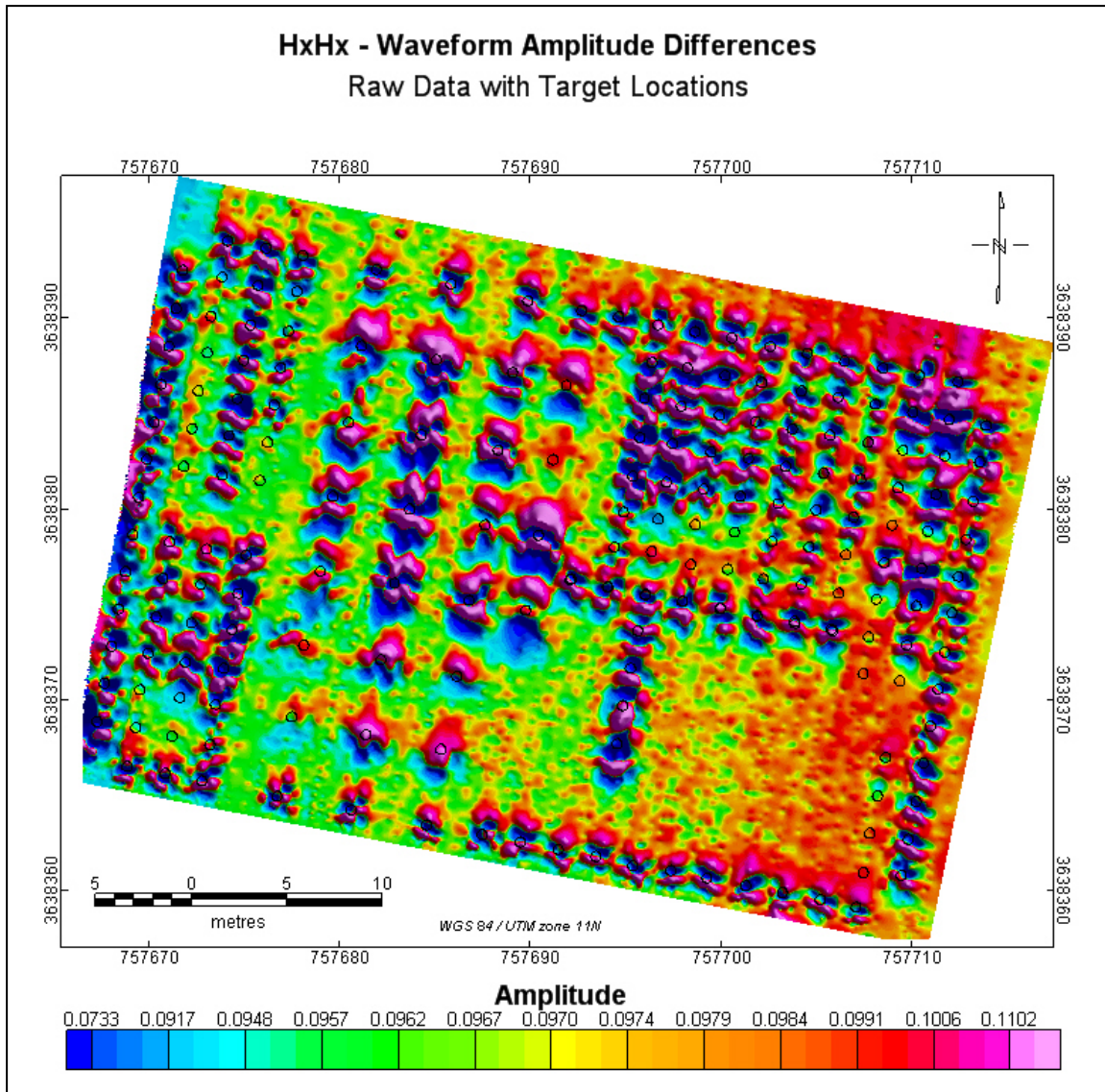


Figure 3.6. This map shows the results when both excitation and reception are in the along track, x, direction. This map shows adjacent line position alignment problems which are probably more obvious when using the along-track polarization. These data are raw. No adjacent line shifts nor leveling have been applied.

3.6 High Density Grid (Tic Tac Toe) Results

Three targets, an 81 mm, a 60 mm, and a 20 mm, were selected and a nominally 25 cm spacing 3 m x 3 m grid was run over each using each of the three excitation polarizations and corresponding receiving directions. The method we used for cart location was to lay out cords with painted marks on them. The cart was equipped with a vertical stick at the front and a pin flag in line with a vertical plane passing through the midline of the sensor cube (Figure 3.7). The stick and pin flag were used to position the cart. Over parts of some of the ground there was local topographic relief and the cart was significantly tilted (Figure 3.8). Thus, some of the indicated GPS locations are inaccurate.

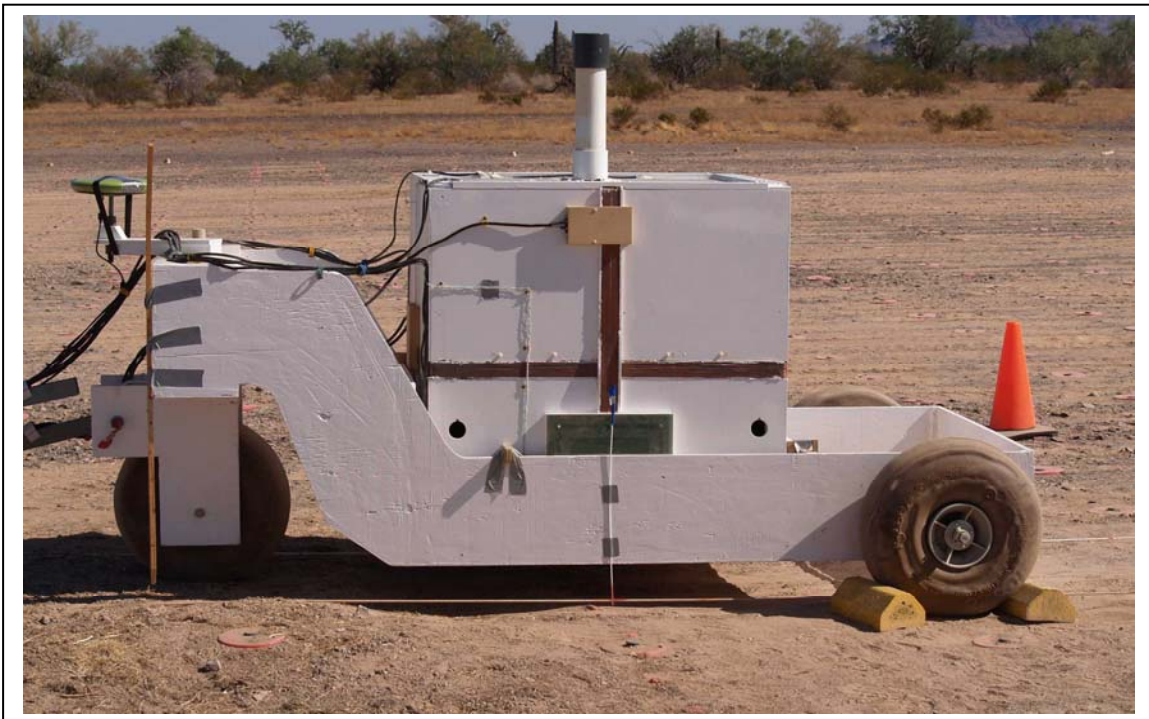


Figure 3.7. The cart was unhitched from the tractor and positioned by hand. The stick on the left front corner of the cart and the pin flag on the side were used to align the cart on a line defined by marked cord.

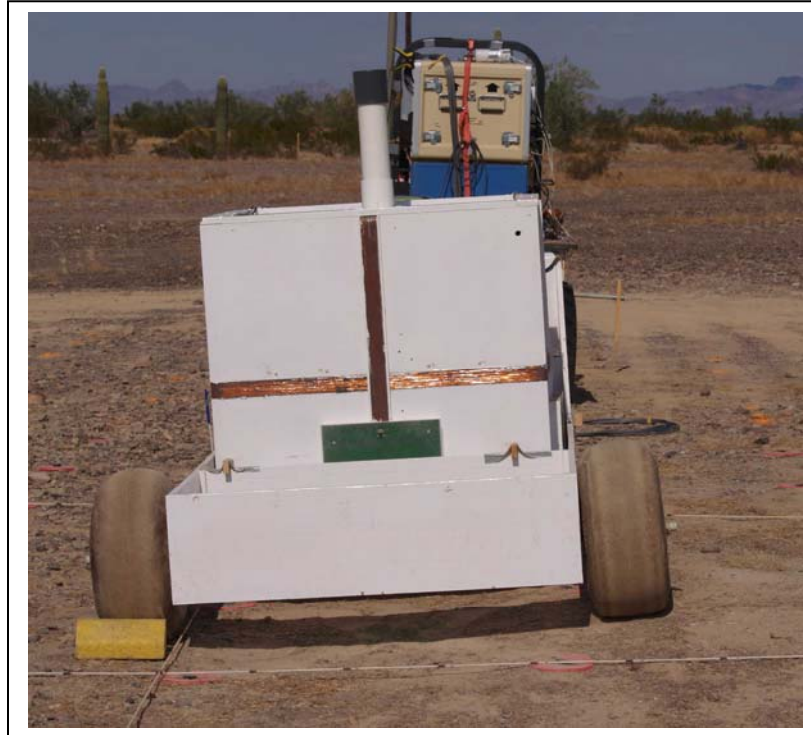


Figure 3.8 Although the ground surface over the Calibration Grid is mostly flat, there are local mounds sufficient in size so that the GPS recorded locations will be offset and the geometry of the coils relative to the target also varies over the grid.

The target of Figure 3.7 is an 81 mm M374 mortar round at grid location “E2.” The target spreadsheet furnished to us indicates that this target is buried 0.67 m deep, oriented with the nose grid (magnetic) north and dipping upward at 45 degrees. The target at F2 is identical except that it is buried with a downward dip of 45 degrees. In this case the two target signatures somewhat overlap as can be seen. The northward shift of the maximum amplitude is expected for two reasons. First, the target is not symmetric from front to back. Second, and more important, the target is dipping.

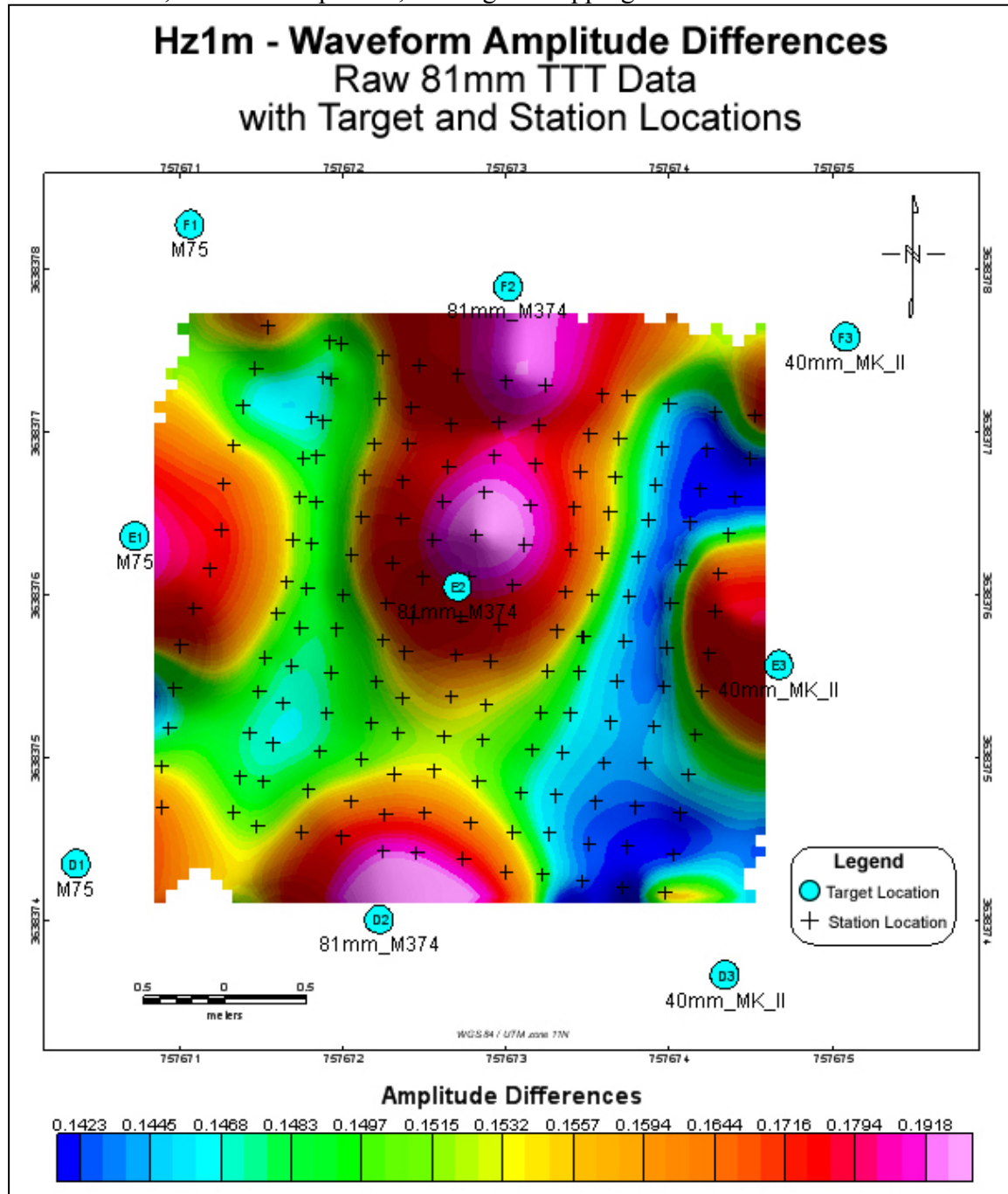


Figure 3.7. This amplitude map from vertical field data shows a maximum that is not directly over the center of the target, but shifted to the north.

Although the data do not extend far enough north to cover the target at F2, we would expect the maximum amplitude for this target to be shifted south.

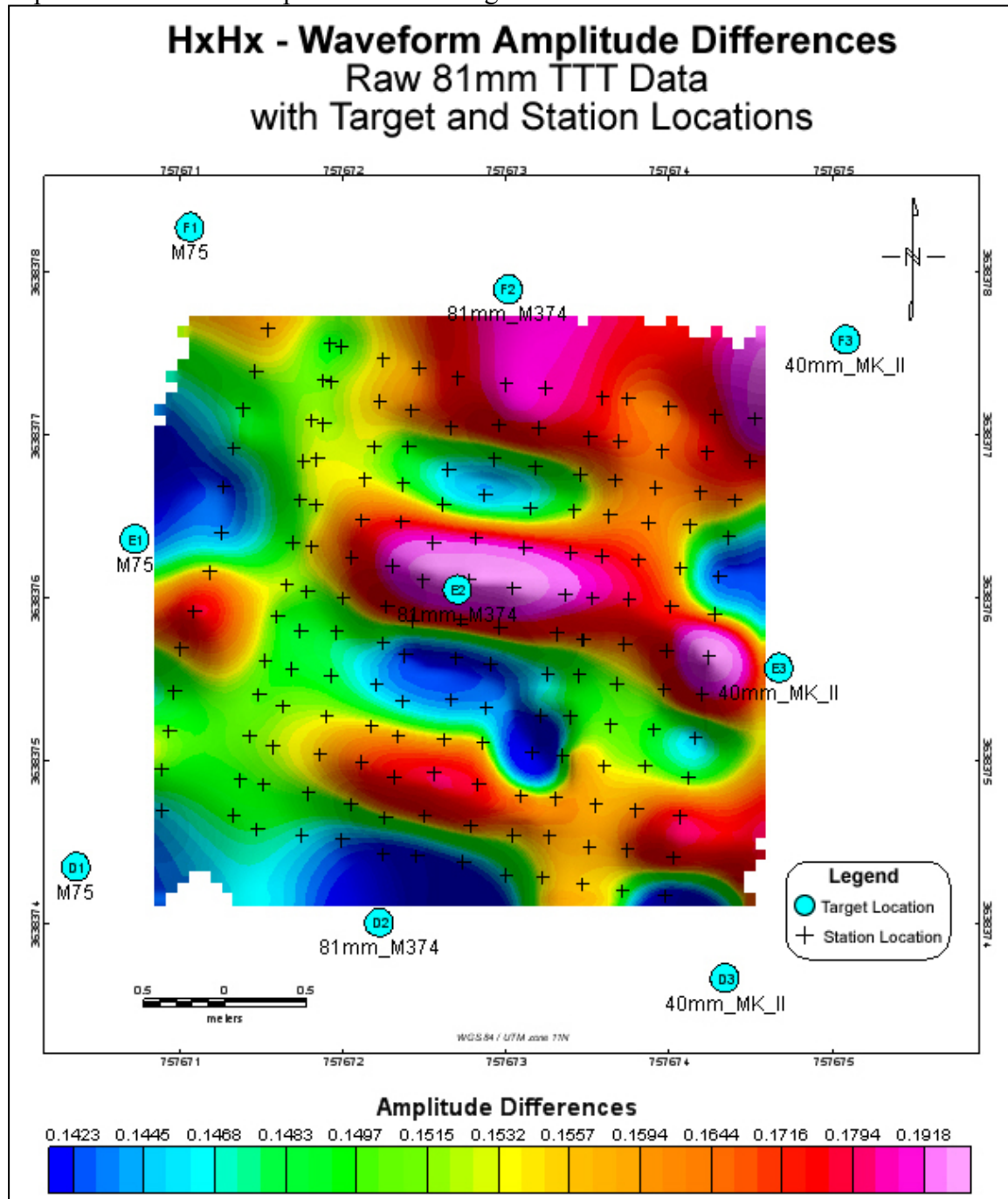


Figure 3.8. This figure shows the data over the 81 mm target when the excitation is in the X (grid north) direction. If the target at E2 was vertically oriented it would lie on a transition from positive to negative response. Note that there is a DC shift on the color bar that has not been removed.

Figure 3.9 is a map produced when the direction of excitation and observation is aligned with grid east-west and perpendicular to the long axis of the 80 mm target.

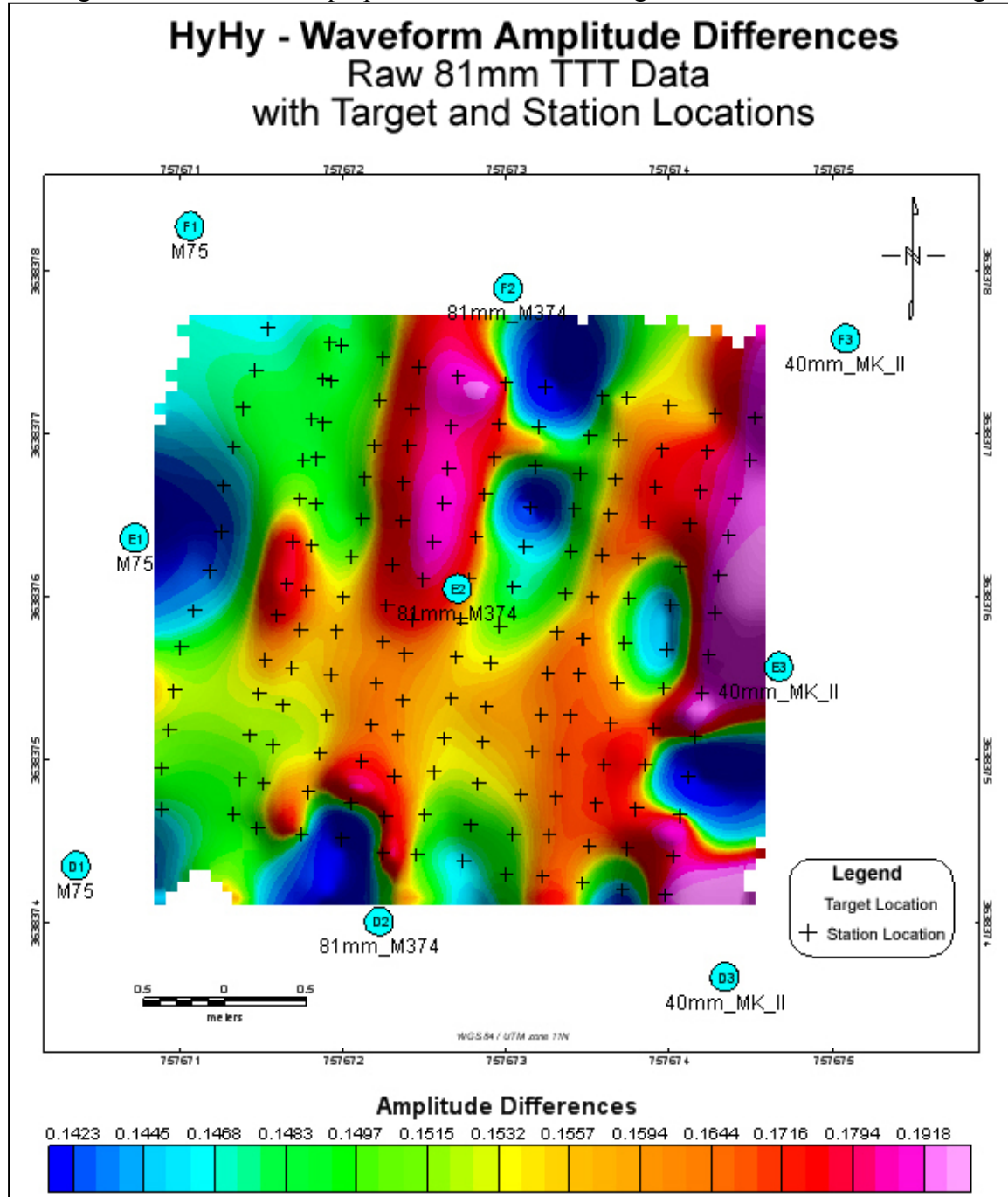


Figure 3.9. These data were recorded when the excitation and observation directions are both in the direction perpendicular to grid north and to the target long axis. The apparent shift to the north is attributed to the target nose-up north orientation. The amplitude pattern around the perimeter of the map is influenced by adjacent targets.

Figure 3.10 shows amplitude data over a 60 mm M49A3 mortar round that is buried 0.25 m deep, oriented along grid (magnetic) north and horizontal, i.e., not dipping.

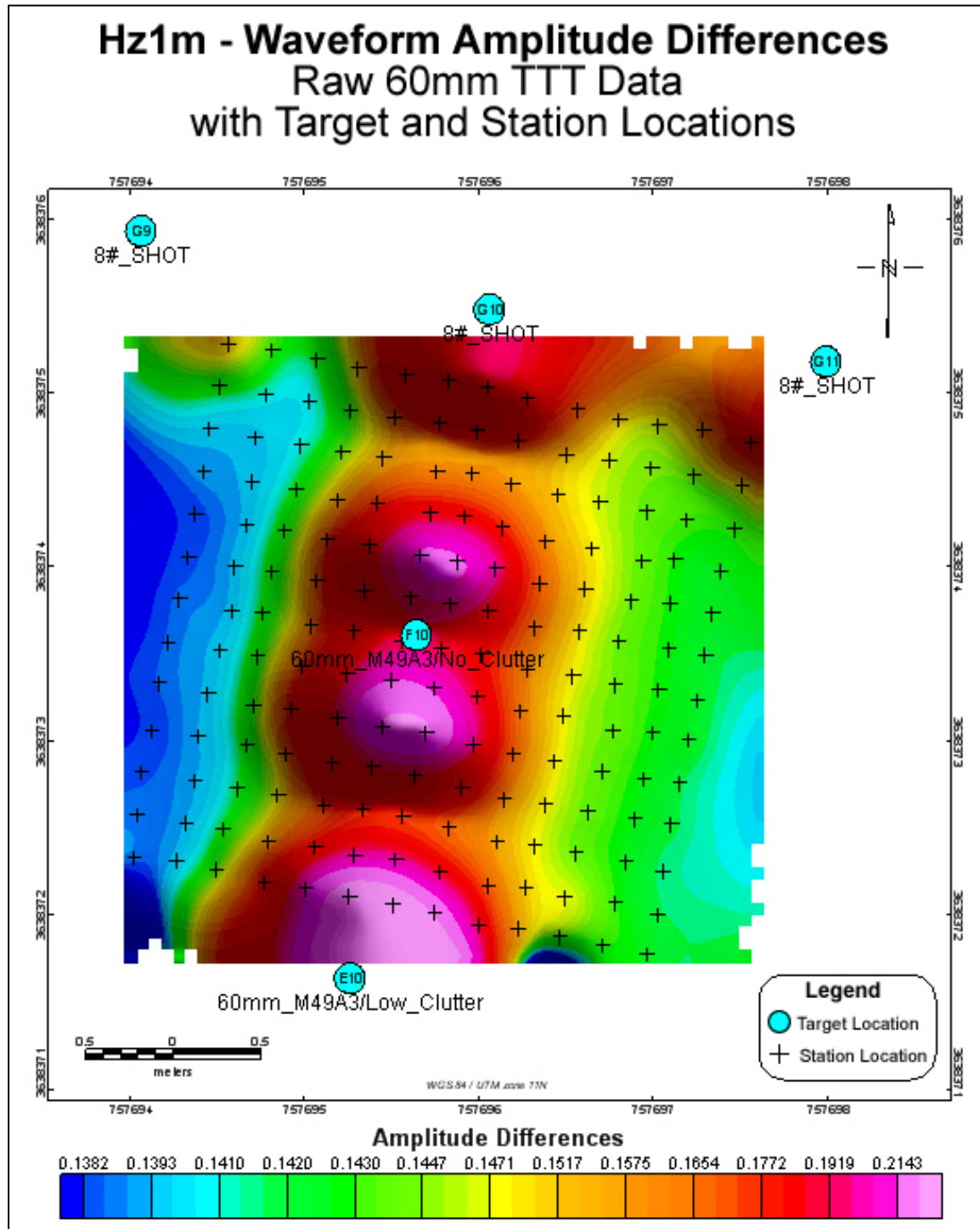


Figure 3.10. An amplitude map over a 60 mm M49A3 mortar round buried in a horizontal orientation, nose grid north, at 0.25 m deep.

The “double peak” signature is expected and is a consequence of a spatial convolution of the field patterns of the Tx and Rx coils and the target characteristics. Note that the southern peak has a higher amplitude than the northern peak. We think this is real and a consequence of the fact that the tail of an M49A3 is ferrous, but the nose has non-ferrous parts. We observed a similar pattern over this kind of target in the laboratory.

Figure 3.11 shows the spatial pattern for the 60 mm target when the polarization is grid north. Note that the location of the target is on a transition as expected by symmetry.

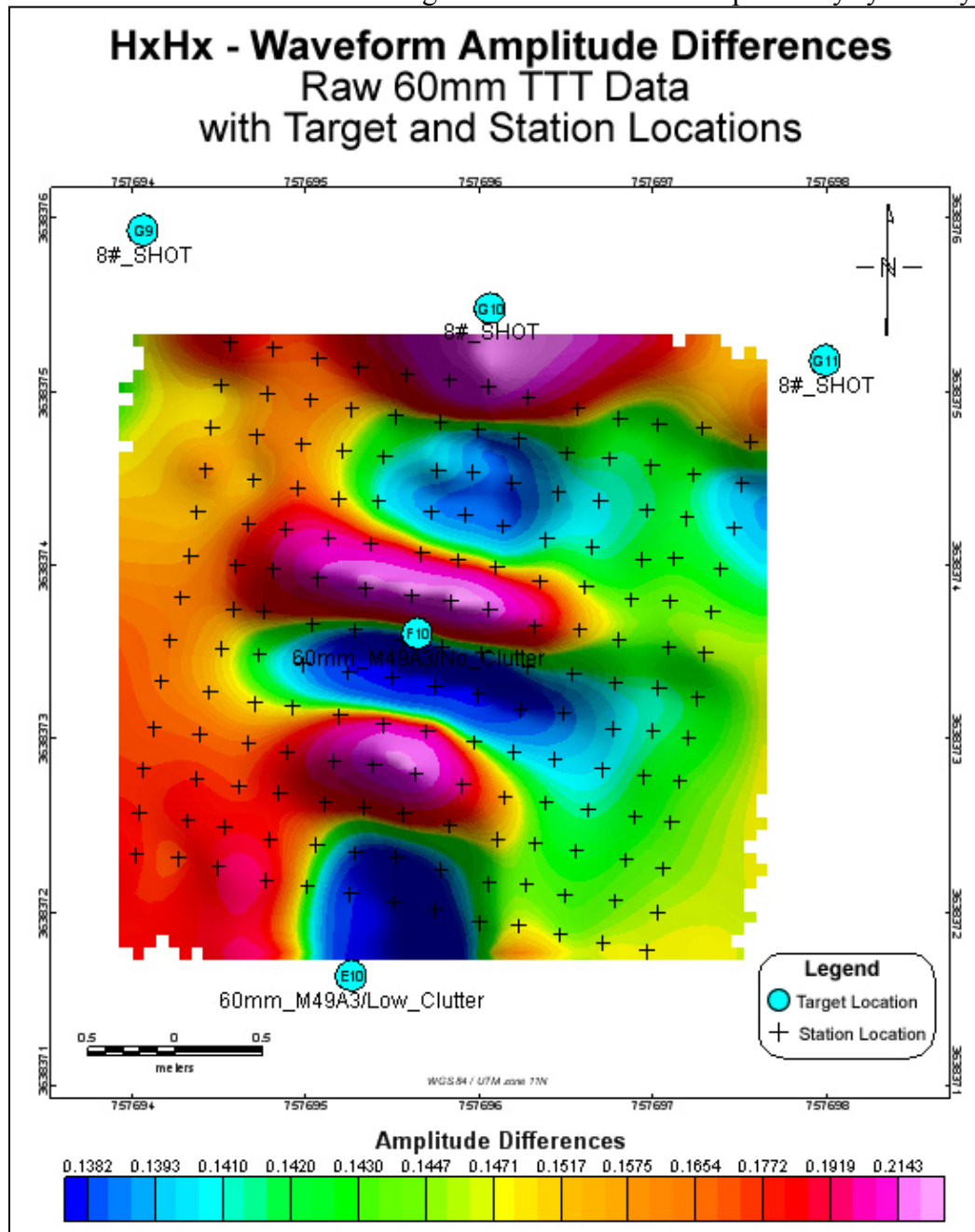


Figure 3.11. An amplitude map over a 60 mm mortar round oriented grid north when the excitation and observation directions are also along grid north.

Figure 3.12 shows the result for the same target when the excitation and observation directions are along grid east.

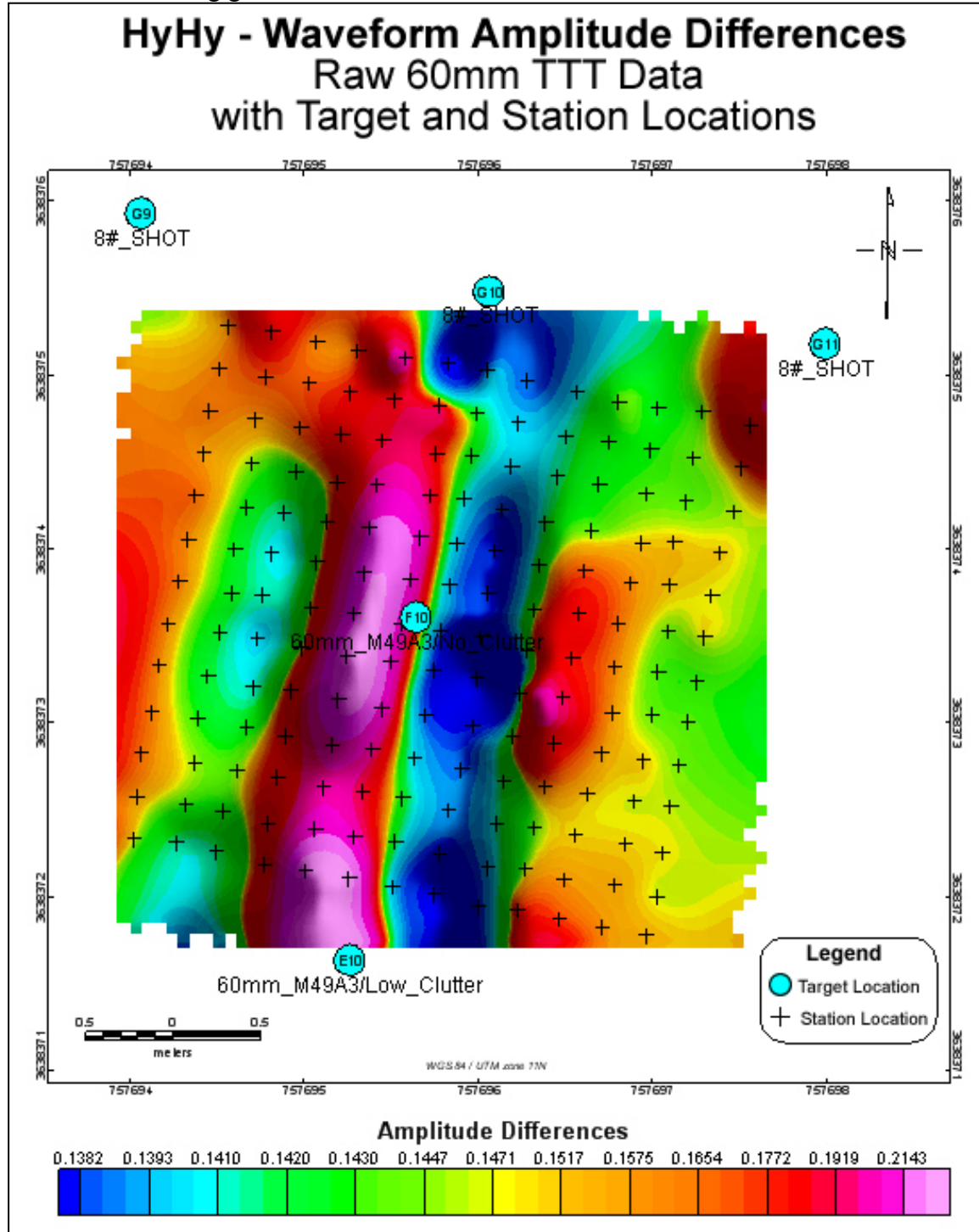


Figure 3.12. This is the amplitude map for the 60 mm mortar round when the polarization is along the east-west direction, perpendicular to the target long axis. We note that the target appears to be on a transition (east-west on grid) and that the tail to the south has slightly higher amplitude than the nose, consistent with our discussion of Figure 3.10.

Figure 3.13 shows a vertical polarization amplitude map over a 20 mm projectile at location L15. This projectile is buried 0.13 m deep oriented grid north nose up 45 degrees. Although this target would probably be detected, the location is off approximately 25 cm. This could be due to low SNR. For a target this small one would not expect that the dip could produce a significant apparent location offset. Since the data are taken while the cart is stationary there should not be significant GPS errors. Cart tilt could introduce a few centimeters of error.

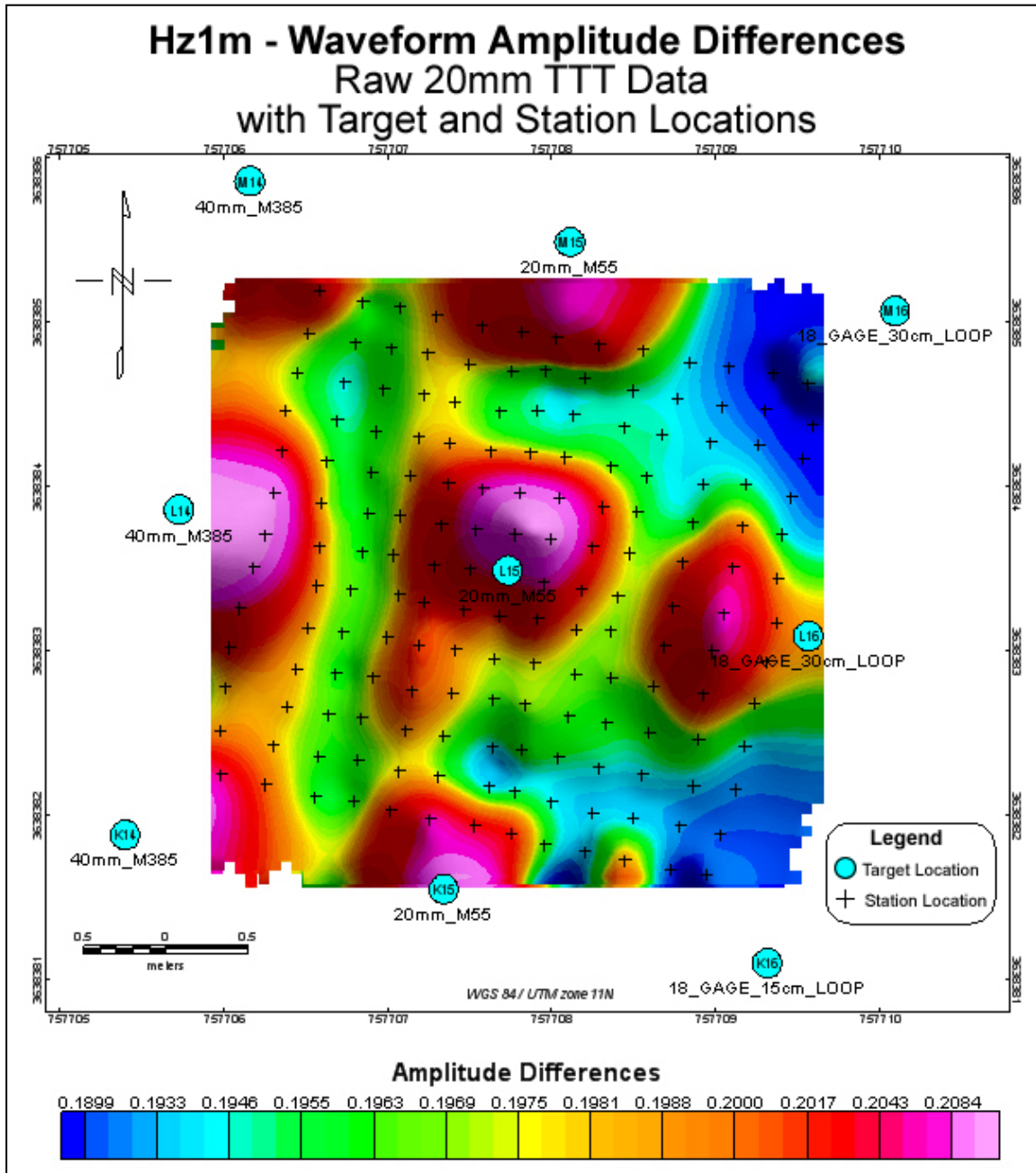


Figure 3.13. An amplitude map over a 20 mm target using vertical polarization.

Figure 3.14 shows the amplitude map over the 20 mm target with grid north-south polarization. The apparent location of the target is about 25 cm too far north, the same as in Figure 3.13. The fact that the two target locations are off by about the same amount and in the same direction suggests a systematic error and not simply poor SNR.

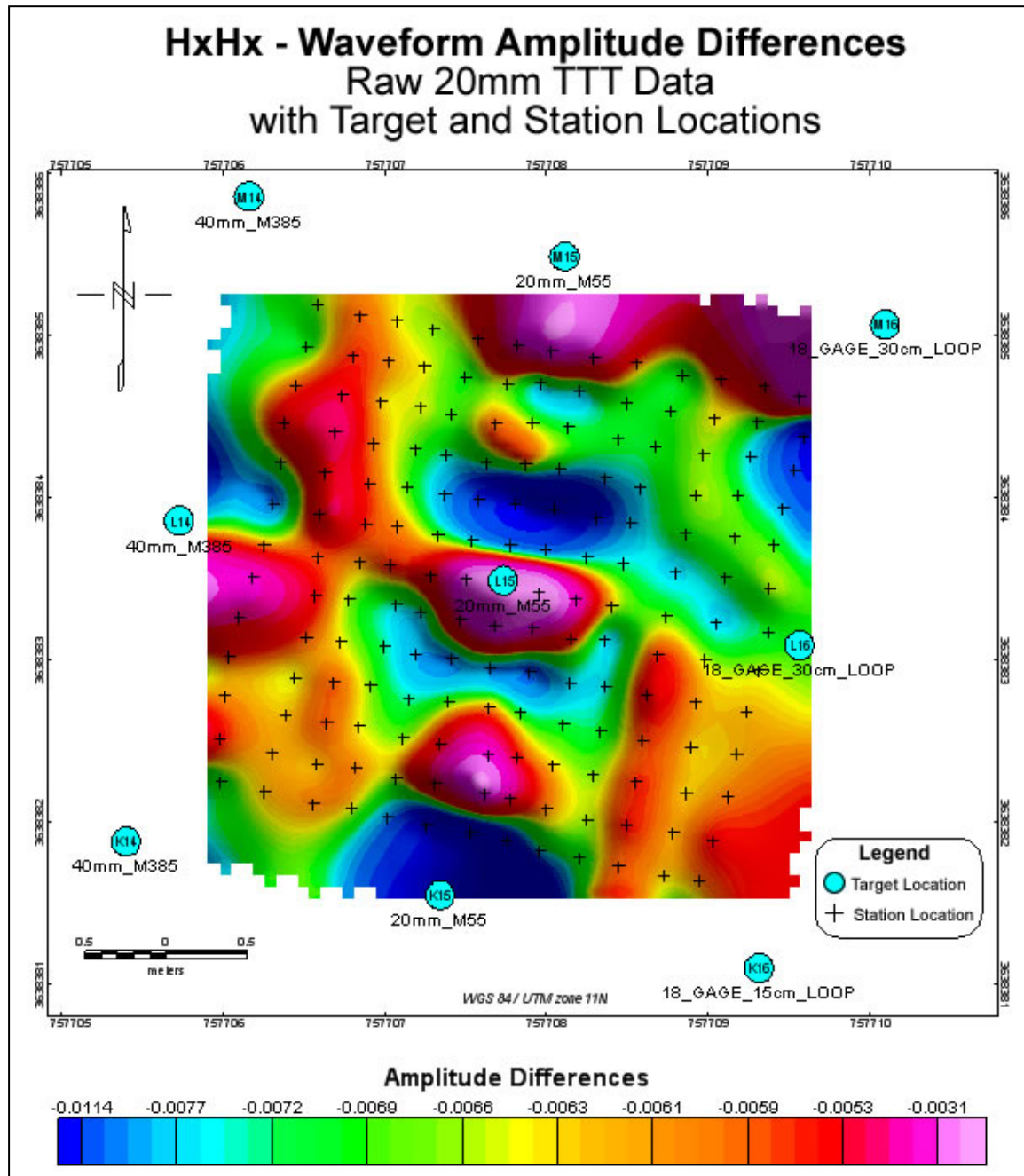


Figure 3.14. An amplitude map over a 20 mm target using grid north-south polarization.

Figure 3.15 shows an amplitude map over the 20 mm target using grid east-west polarization.

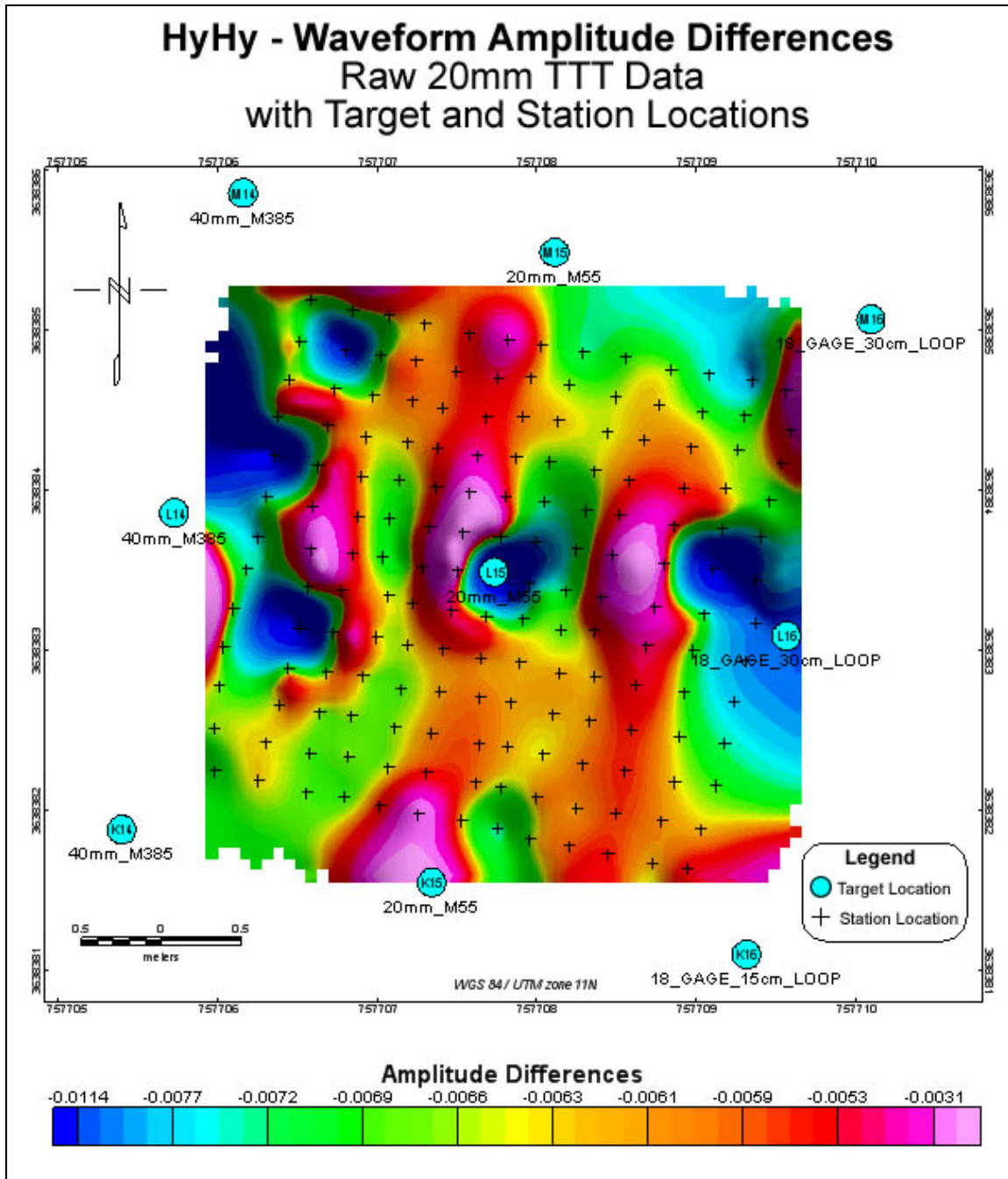


Figure 3.15. This figure shows an amplitude map over the 20 mm target using a grid east-west polarization. In this case there is a known bad waveform that distorts the image immediately in the vicinity of position L15. It was left in to see what impact it might have on the map. In this case it produced a roughly circular “pit” near the target.

Figure 3.16 shows an example of an amplitude plot using one of the smaller 34 cm loops over the 60 mm target. Since the loop is smaller, the spatial footprint of the Rx loop field pattern and the fields produced by the 60 mm target is more compact. This figure may be compared with Figure 3.10. In Figure 3.16 we note an apparent system drift from left to

right. This is more of a problem for the tic tac toe data than for data over the entire Grid because the beginning and ending of lines are often influenced by adjacent targets and thus leveling is more difficult.

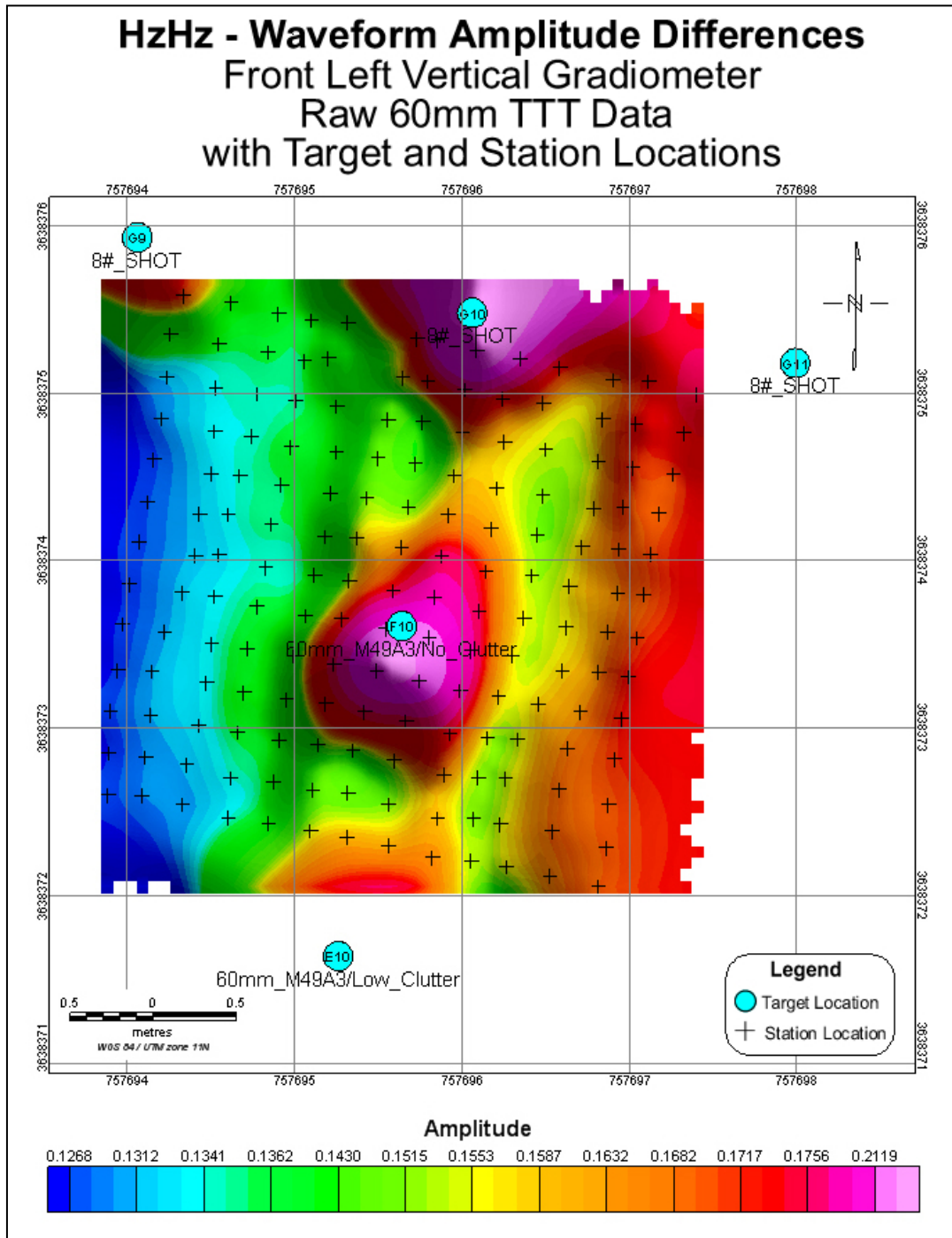


Figure 3.16. An amplitude map produced using vertical excitation polarization and vertical observation, but using one of the 34 cm loops instead of the 1 m receiving loop.

3.7 “Racetrack” H_z Data and Time Picks

On the last day the Calibration Grid was run again. An example is shown in Figure 3.17.

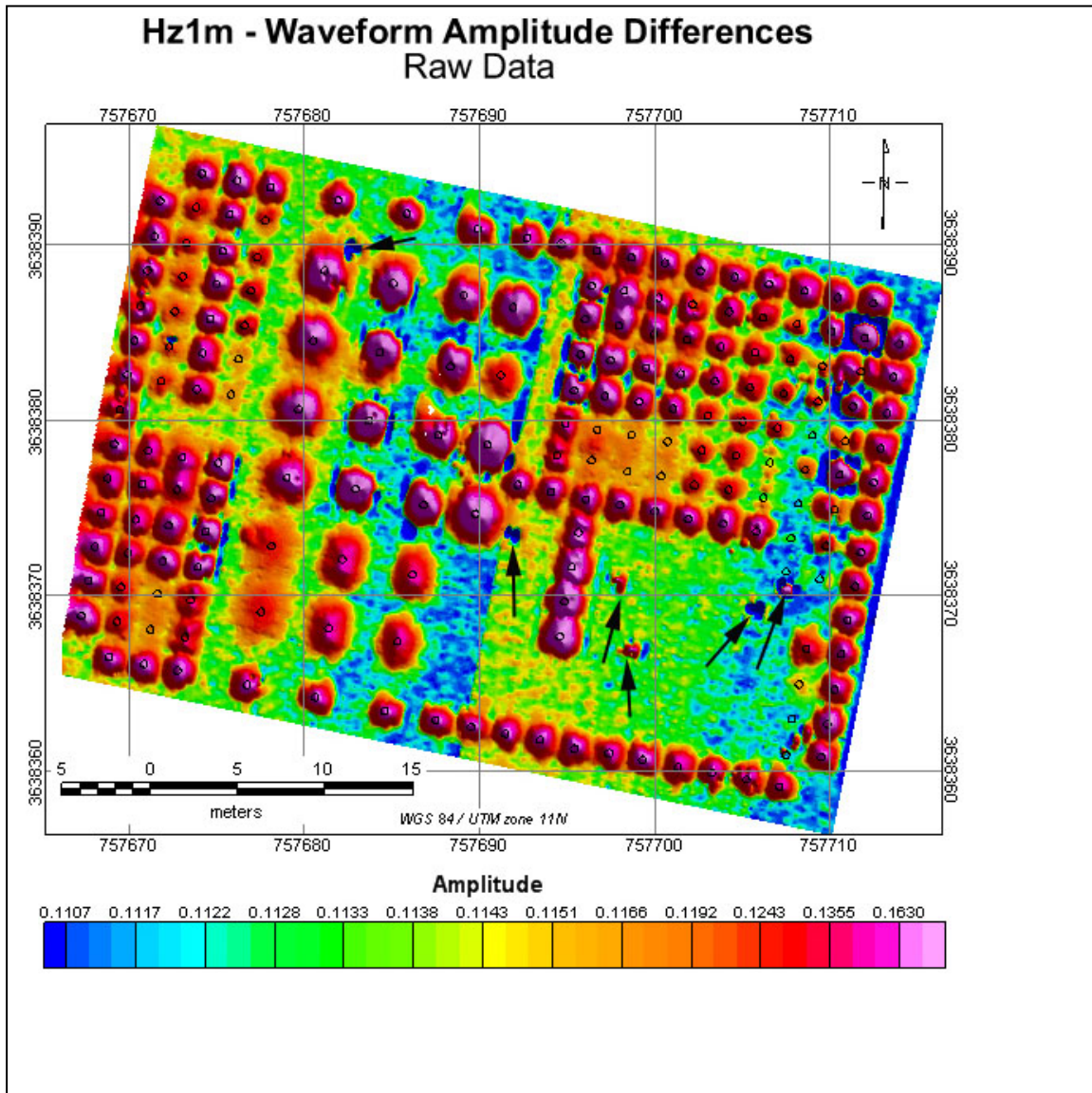


Figure 3.17. This is a vertical field amplitude map taken while the system was sequencing through all three polarizations. The slow instrument drift is evident on each half of the grid as discussed in the text. The data are generally of very high quality although a few bad waveforms that were not removed in the batch processing, produce a few “pits” and “peaks” where there are no targets (see arrows). The earlier time pick was set at 50 μ s and differenced against the end of the waveform at about 5.5 ms in these data.

This time, the speed was reduced to about 40 cm/s and all three Tx polarizations were cycled while the cart was moving. In previous maps, all lines were run from south to north. In these data the western half of the Calibration Grid was run with lines going from south to north, but the cart was then pulled around and lines run north to south down

the eastern half of the grid with lines progressing sequentially toward the east. A slow instrument drift from west to east is evident on the two halves of the grid as seen in Figure 3.17. Figure 3.18 is like Figure 3.17 except that the earlier time was set at 420 μ s after a slope transition in the Tx current.

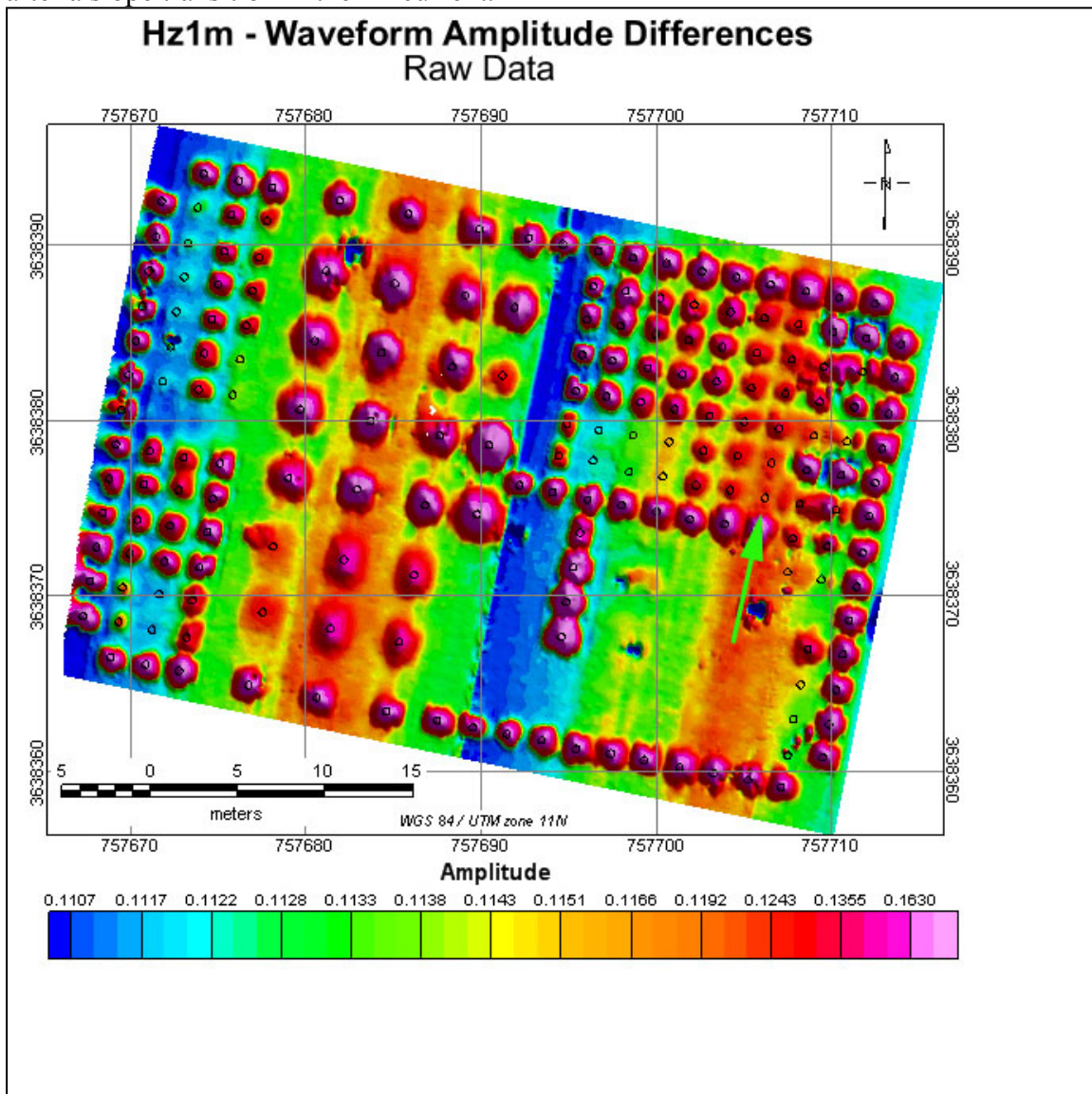


Figure 3.18. This amplitude map is produced from the same data as Figure 3.17, but in this case the early time pick is at 420 μ s instead of 50 μ s. Some of the 20 mm targets in Lane 15 (green arrow) may show better here, but other targets, for example some in Lanes 1, 2, and 3 are clearly better in Figure 3.9. Effects of instrument drift appear more pronounced in this later time pick. Some of the targets that have faded are non-ferrous.

These data are rich with information and it will take some time and effort to learn to optimally extract the available information from them. Efforts in that direction are discussed in Section 4.

3.8 “Racetrack” H_z Data with 34 cm Loop

Figure 3.19 is like Figure 3.17 except that one of the 34 cm loop pairs is the receiver.

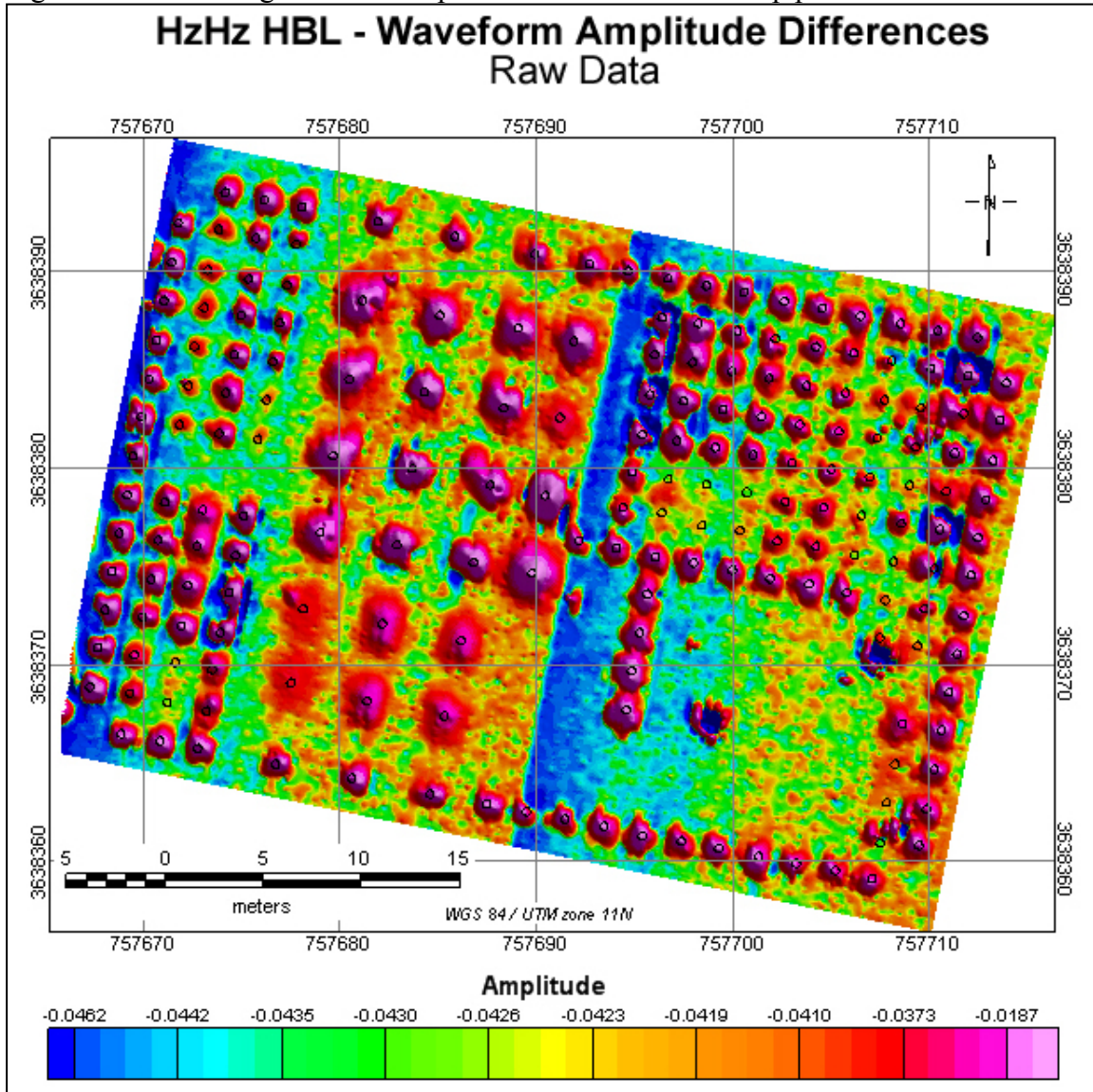


Figure 3.19. This map is similar to Figure 3.17 except that one of the 34 cm loop pairs is the receiver. For some of the shallower targets, for example in Lanes 1, 2, and 3, the smaller loop provides a slightly more focused target response, but for deeper targets there is no spatial advantage to the smaller loop size.

3.9 “Racetrack” H_y Data

Figure 3.20 is an amplitude map of data when the excitation is in the “y” (cross-track) direction and the observing direction is in the same direction.

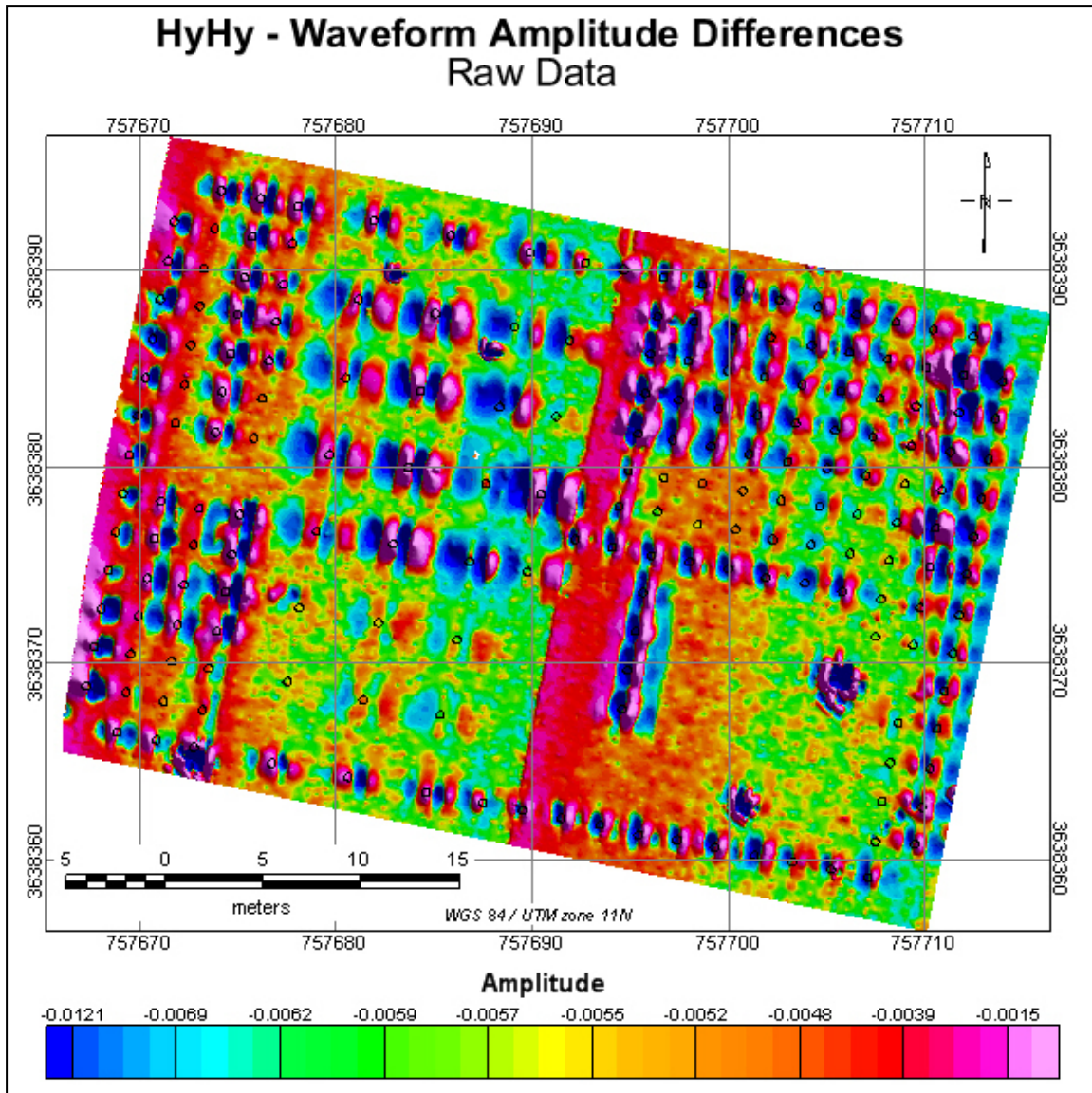


Figure 3.20. This figure shows data when the excitation and observation directions are both horizontal and perpendicular to the direction of travel. This figure may be compared to Figure 3.5.

Apart from some occasional noise anomalies of unknown origin, highlighted in Figure 3.17, the data recorded while multiplexing is quite close to the same quality obtained when the system is running with only one polarization active. The main penalty for such recording is speed. The “racetrack” data, taken while the system was multiplexing through all polarizations, were recorded while the cart was moving at a speed of about 0.4 m/s as opposed to 1 m/s or faster for the single excitation polarization data.

3.10 “Racetrack” H_x Data

Figure 3.21 shows data recorded while the excitation and observation polarizations are horizontal and parallel to the direction of travel. This may be compared to Figure 3.6.

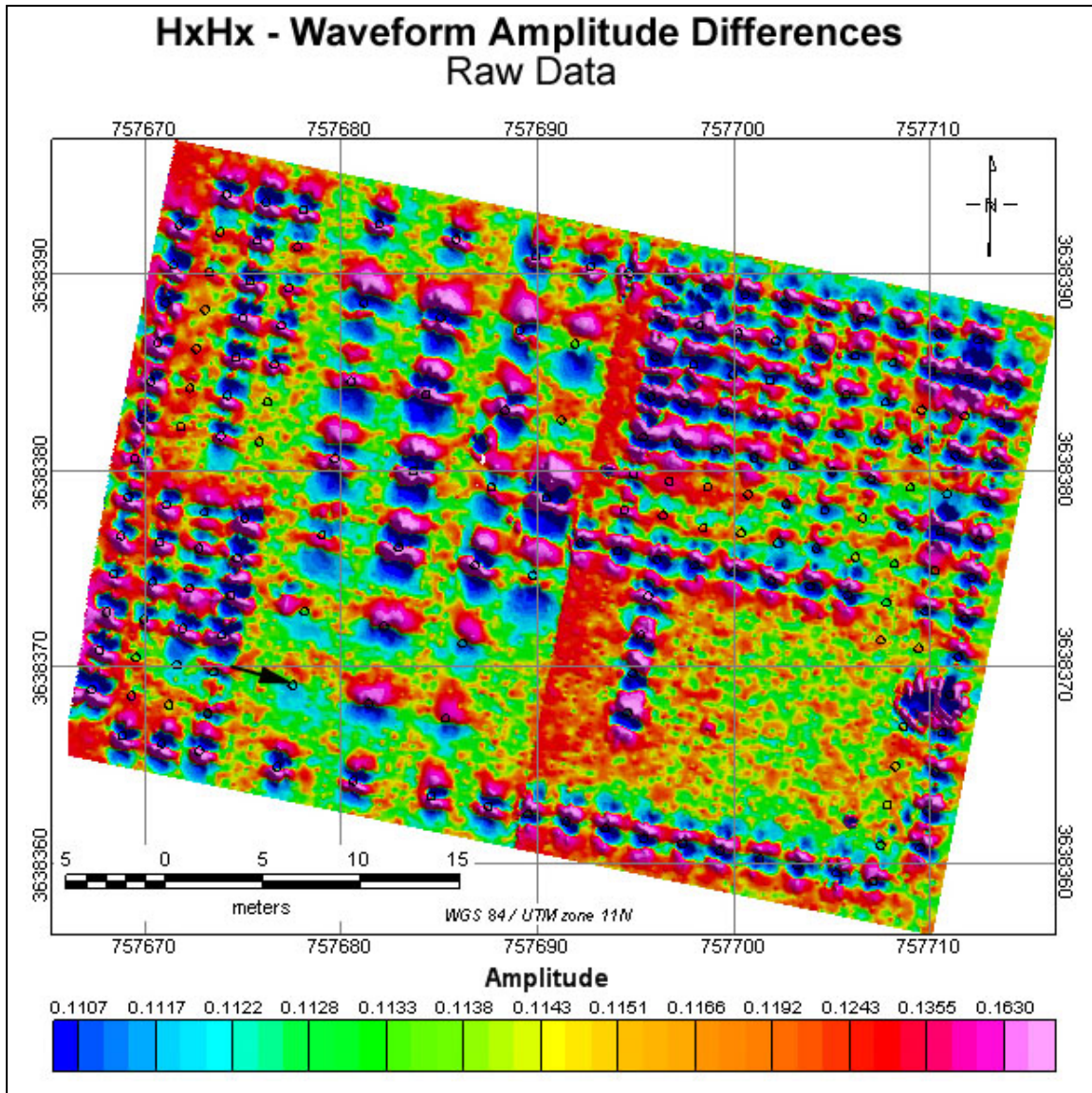


Figure 3.21. This figure shows data when the excitation and observation polarizations are both along the direction of travel. Compared to Figure 3.6 our line-to-line positions are better, hence individual targets are not so “split.” The black arrow in the lower left indicates a 155 mm target buried 1.5 m deep and oriented along the direction of travel.

In Figure 3.21 a 155 mm target, indicated by the black arrow, can be seen whereas in Figure 3.20, with the horizontal polarization perpendicular to the long axis of the 155 mm target, the target cannot be discerned. This difference is expected, because for a ferrous axisymmetric target whose long axis is significantly longer than the diameter, the stronger late-time response will be obtained when the target is excited and observed by magnetic fields oriented parallel to the long axis of the target.

3.11 Cursor-Based Target Composition Classification

In this section we discuss a simple, quick approach to target separation into classes of ferrous targets versus non-ferrous and mixed targets having both ferrous and non-ferrous parts. This approach relies on the fact that ferrous and non-ferrous targets that have typical UXO shapes generally display distinctly different responses as we have noted in several previous reports and papers. There appears to be a shape factor exception to this scheme; namely, thin plates that are illuminated along their thin dimension may appear to be non-ferrous even if they are ferrous. The reason for this is that the separation of ferrous from non-ferrous is based on the fact that the ferrous targets are being magnetized at late times by ALLTEM. If the target dimension along the direction of the inducing field is very small, there will be little magnetostatic dipole moment induced in the target. To illustrate the approach on real data from the Calibration Lanes, we begin by showing raw waveforms from Lane 2 that contains marker shots, 81 mm M374's and BDU-28's (Figure 3.22). The BDU-28's have a large non-ferrous metal portion in their construction, as well as some ferrous parts, so they are a good example of a mixed-composition target. The shots are pure ferrous and the 81 mm M374's have some non-ferrous metal parts, but are dominantly ferrous. Figure 3.23 shows a “background” waveform. This is from the first few waveforms recorded on this line, before the sensors moved over the lane boundary markers. Figure 3.24 shows the “residual” waveforms along this line after subtraction of the background waveform.

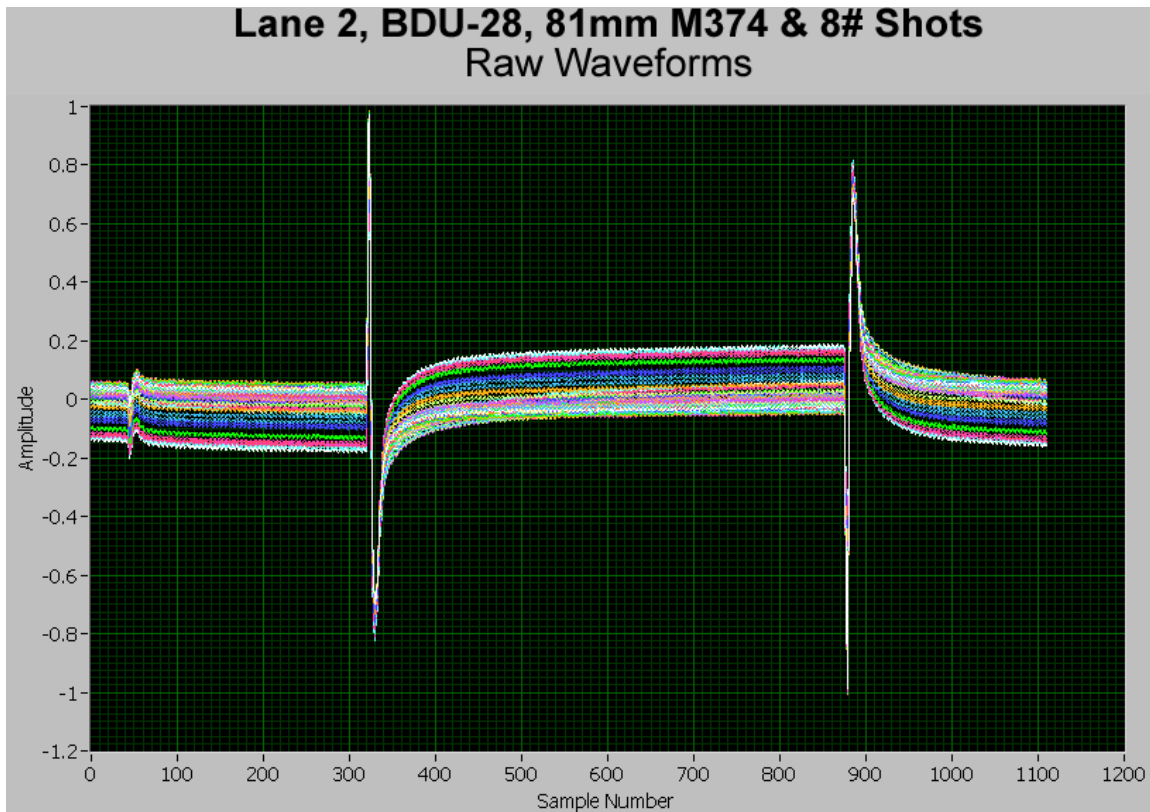


Figure 3.22. ALLTEM raw waveforms for Lane 2 containing two 8-lb shots, six 81-mm M374's and six BDU-28's

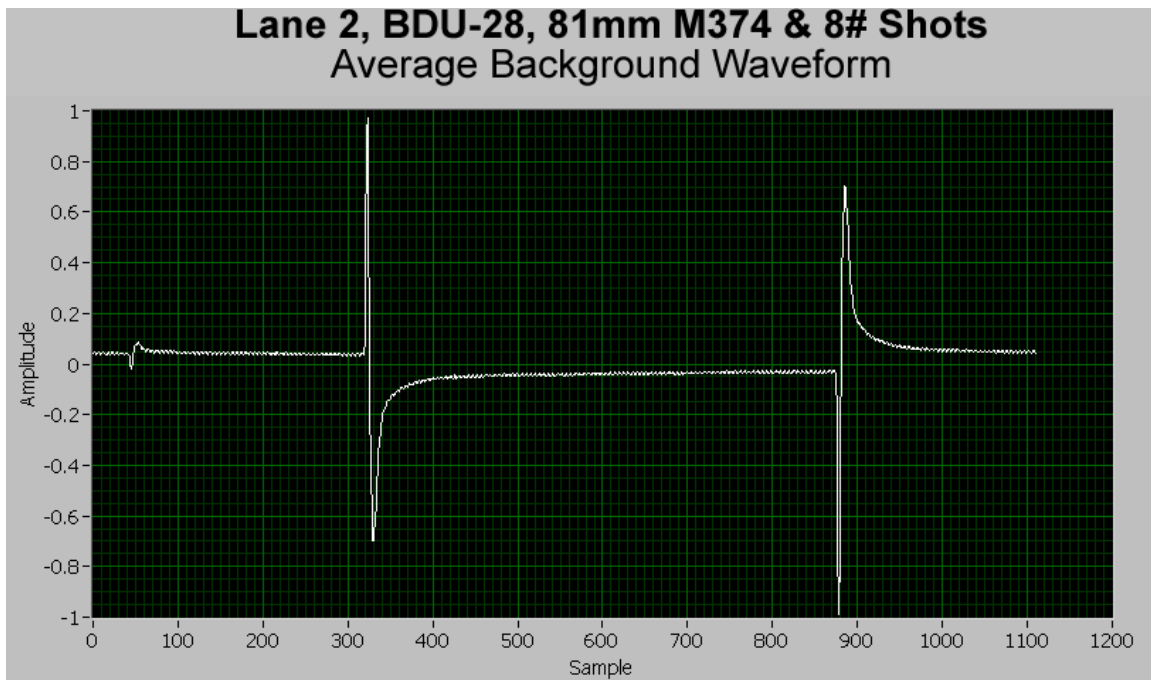


Figure 3.23. An ALLTEM “background” waveform for Lane 2. This waveform is an average of the first 20 waveforms before the sensors encountered any targets.

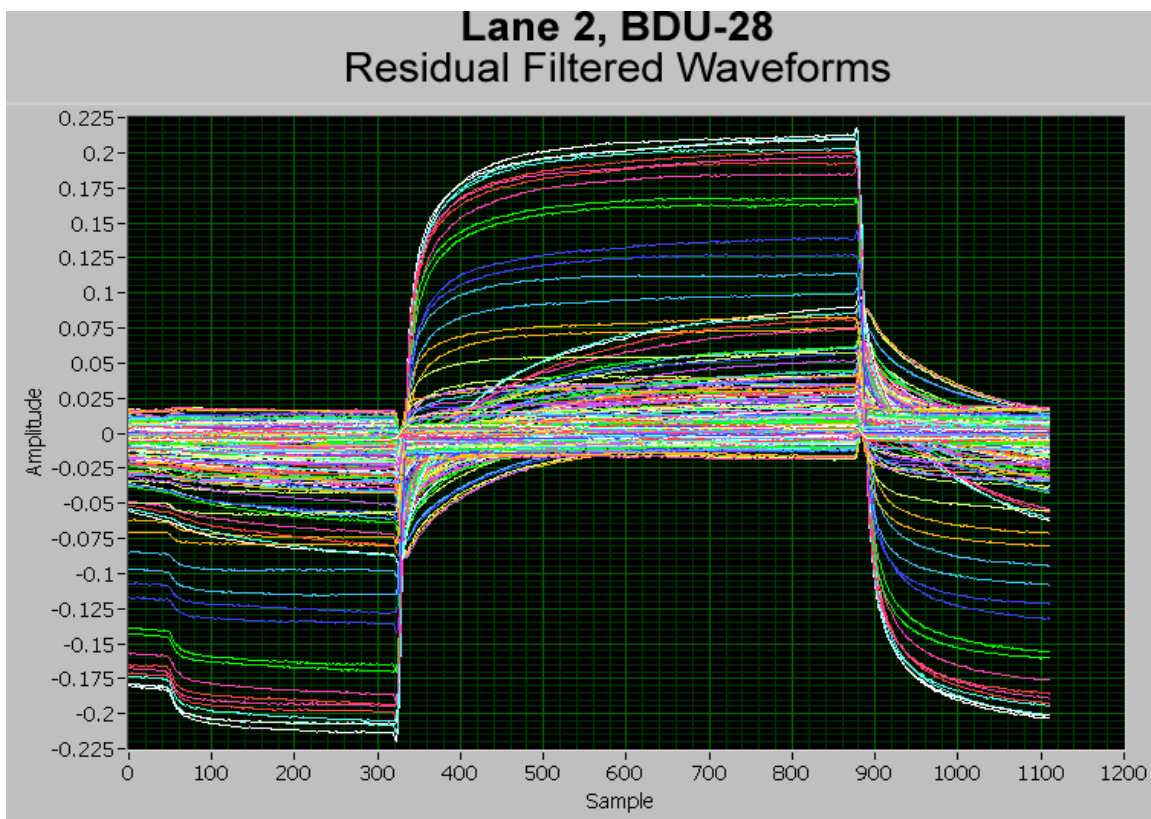


Figure 3.24. ALLTEM residual waveforms for Lane 2 containing two 8-lb shots, six 81-mm M374’s and six BDU-28’s. Waveforms are filtered with a low-pass zero-phase-shift filter to remove high frequency noise in the raw waveforms.

The residual waveforms from the three types of targets in Lane 2 are distinctly different. As an experiment to see whether an automatic or semi-automatic sorter could be devised, we wrote a program in LabVIEW (Wright and others, 2006) that allows the user to set cursors at any desired location, then run through the data and calculate amplitude differences and a late time amplitude from three selected cursor locations. Figure 3.25 shows an example. One cursor has been set on a received waveform just before a slope transition (where the transmitter triangle wave has changed slope). A second is set just after the transition, and a third is set just before the following transition. Waveforms for the background, a marker shot (green) an 81 mm M374 (blue) and a BDU-28 (pink) are shown. The 8 lb. marker shot is spherical and ferrous. The large amplitude for the boundary marker shot is due to the shallow burial depth. The 81 mm behaves similarly, but at lower amplitude and longer time constant. The BDU-28 breaks after the first cursor in the opposite direction from the other two targets – an indication of a dominantly non-ferrous target.

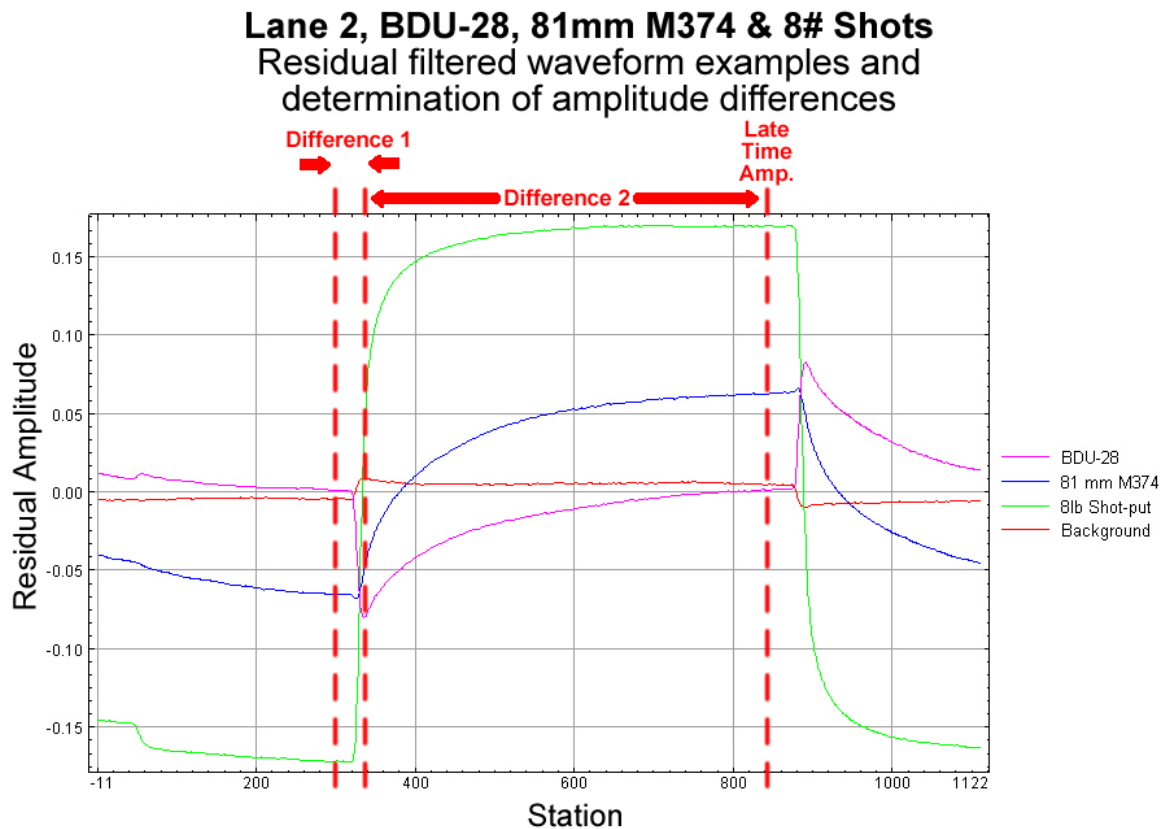


Figure 3.25. Residual filtered waveform and cursor example for Lane 2. Target location plots are made using the amplitude of the “Difference 2” values. Ferrous versus non-ferrous target classifications use the amplitude of both the “Difference 1”, “Difference 2” and “Late Time Amplitude” values.

Figure 3.26 shows an example of target location picks from the amplitude difference at the times annotated as “Difference 2” in Figure 3.25. Figure 3.27 shows an example target sorting along Lane 2. The line plotted in black is the amplitude difference between

Lane 2, BDU-28, 81mm M374 & 8# Shots
Difference 2 amplitude and target picks

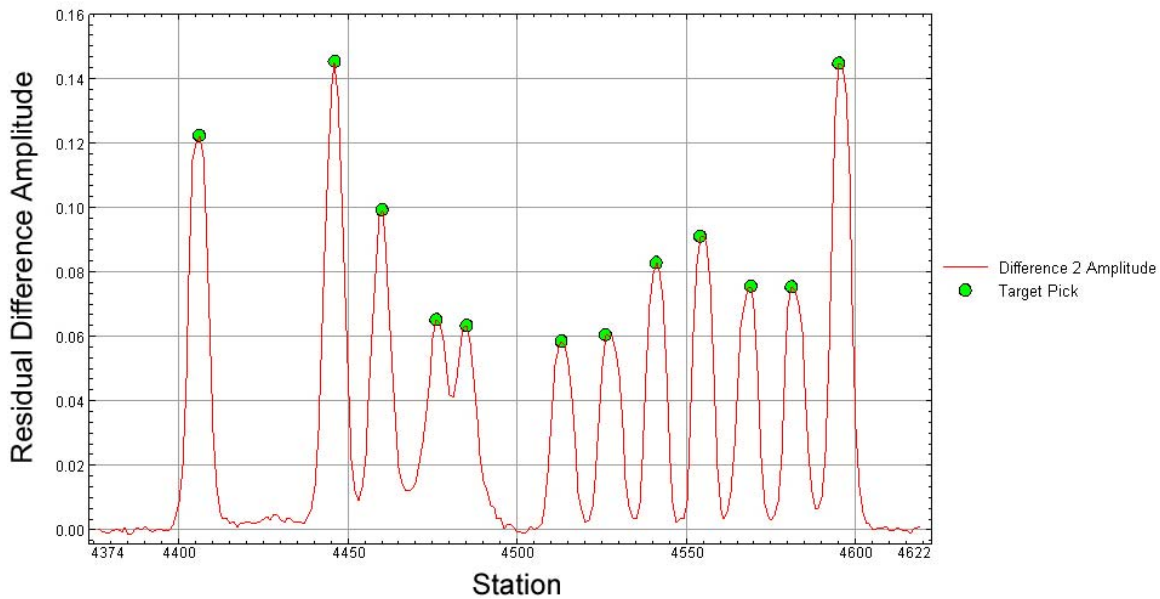


Figure 3.26. Lane 2 “Difference 2” amplitudes and target picks. Target locations are determined by using a threshold algorithm that picks the peaks along line profiles of the “Difference 2” amplitudes.

Lane 2, BDU-28, 81mm M374 & 8# Shots
Difference 1 and 2 amplitudes
and non-ferrous target picks

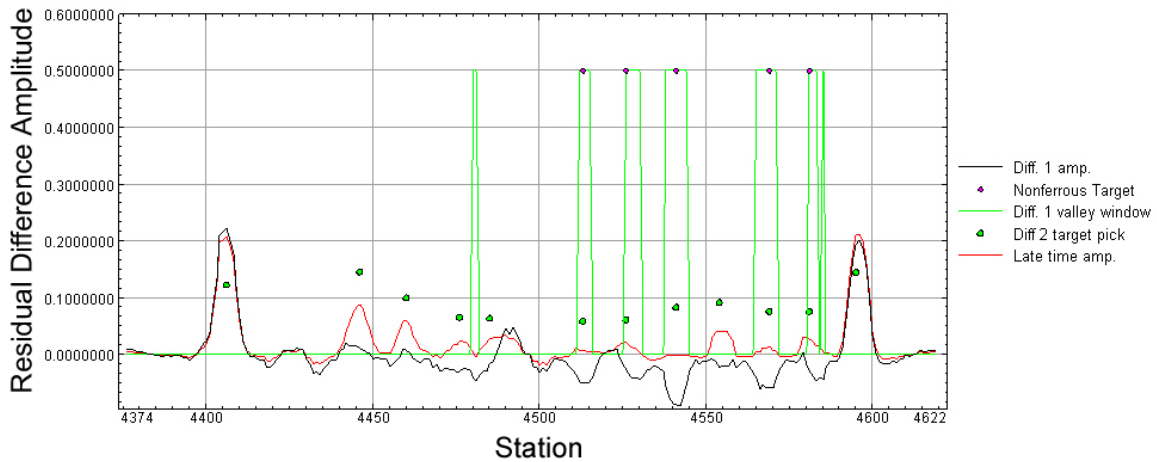


Figure 3.27. An example of target composition sorting along Lane 2. At the location of a purely ferrous target we expect the red and black lines to both be positive. For non-ferrous and mixed targets we expect the black line to be negative and the red line to be negative or zero for purely non-ferrous targets and positive for targets containing ferrous parts.

the cursor locations labeled “Difference 1” in Figure 3.25 and the red line is the “Late Time Amplitude. If this sorter worked perfectly, purely ferrous targets would all have a late time amplitude above the background and a beginning slope that is positive. All purely non-ferrous targets would have a negative beginning slope and a late time value at or below the background level. Mixed targets would have a negative beginning slope and a late time value above the background level. Potentially non-ferrous targets are determined by using a threshold algorithm that picks the valleys along line profiles of the “Difference 1” (black line) amplitudes. The valleys picked are windowed (green line) and if a known target is located within this window and “Late Time Amplitude” (red line) is below a threshold value it is classified as non-ferrous. Of the six BDU-28’s, five were sorted as “non-ferrous or composite” while one was classified as “ferrous.” Figure 3.28 shows the result when this sorter was run over the entire Calibration Grid. The majority of the targets are classified as ferrous, as indeed, most of them are. Three targets in Lane 1 are classified as non-ferrous or composite. Those targets are MK118’s and are mostly non-ferrous. Three of them (half) were classified as ferrous. Lane 7 has two 30 cm

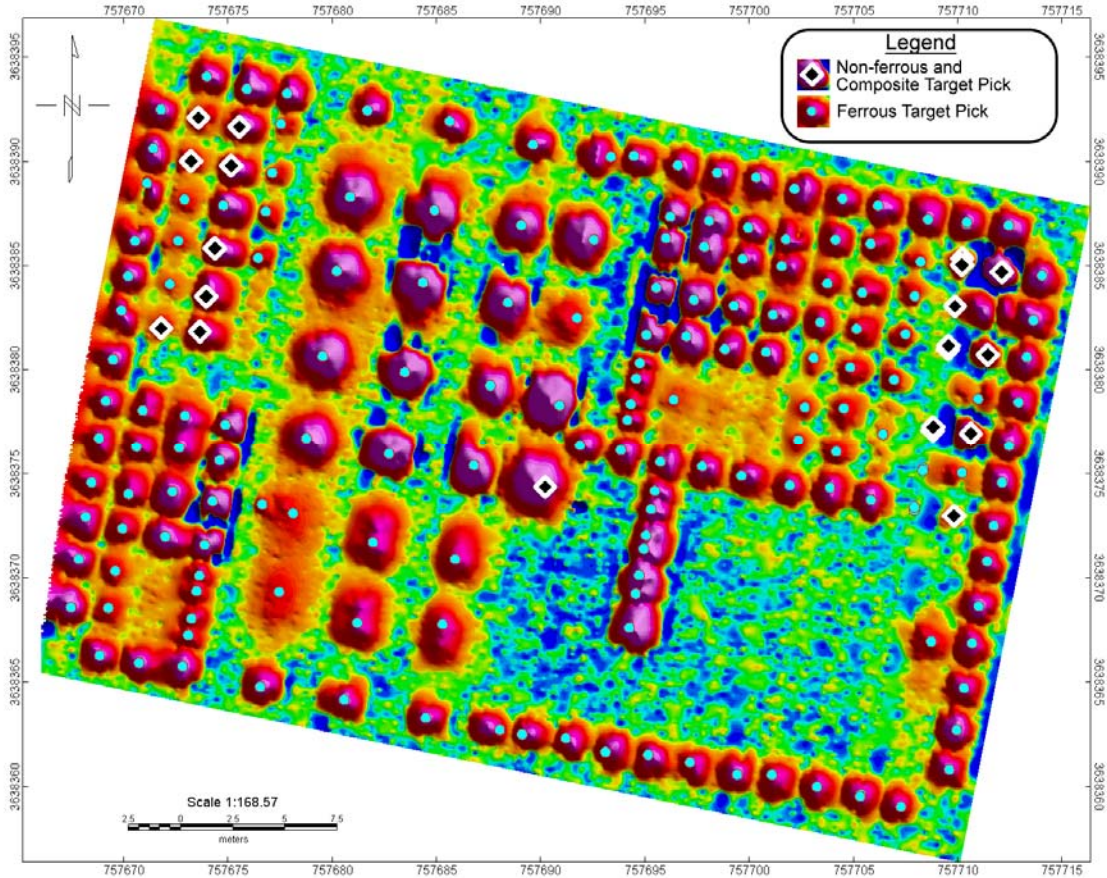


Figure 3.28. Image created from “Difference 2” amplitudes collected using the 1m Hz Hz transmitter and receiver coils. The blue circles show the ferrous target picks determined by thresholding the “Difference 2” amplitudes. The black diamonds represent non-ferrous picks determined from criteria based upon the “Difference 1”, “Difference 2” and “Late Time” amplitudes.

plates and two 60 cm steel plates buried horizontally at 0.5 and 1.0 m depth. One of these was classified as non-ferrous. Lanes 16 and 17 contain eight each 15 cm and 30 cm wire loops at several depths and buried alternately horizontally and vertically, at 0 degree azimuth with respect to magnetic (grid) north. Since the map of Figure 3.20 is made from vertically polarized data, there should be zero response directly over the vertically buried loops and maximum response over the horizontally buried loops. The sorter found half of the loops to be non-ferrous. This simple method can flag certain targets as mostly non-ferrous. We may retain this method as a supplement, or it may be supplanted by the processing and inversion software that we describe in following sections.

3.12 Processing Software

A processing software package is currently under development for processing ALLTEM data sets. This software package, called *GP Workbench*, provides utilities for pre-processing of raw data, calculation of calibration parameters, forward modeling of UXO targets, inversion for UXO properties, graphical user interaction, and generation of publication quality images. *GP Workbench* operates as a stand-alone processing platform, and future development will allow the program to interface with *OASIS Montaj* (Geosoft) in a seamless manner. *GP Workbench* can also process data from other geophysical instruments such as GPR. It is written in Microsoft Visual C++ 6.0. Figure 3.29 illustrates a *GP Workbench* screen of ALLTEM data in section view.

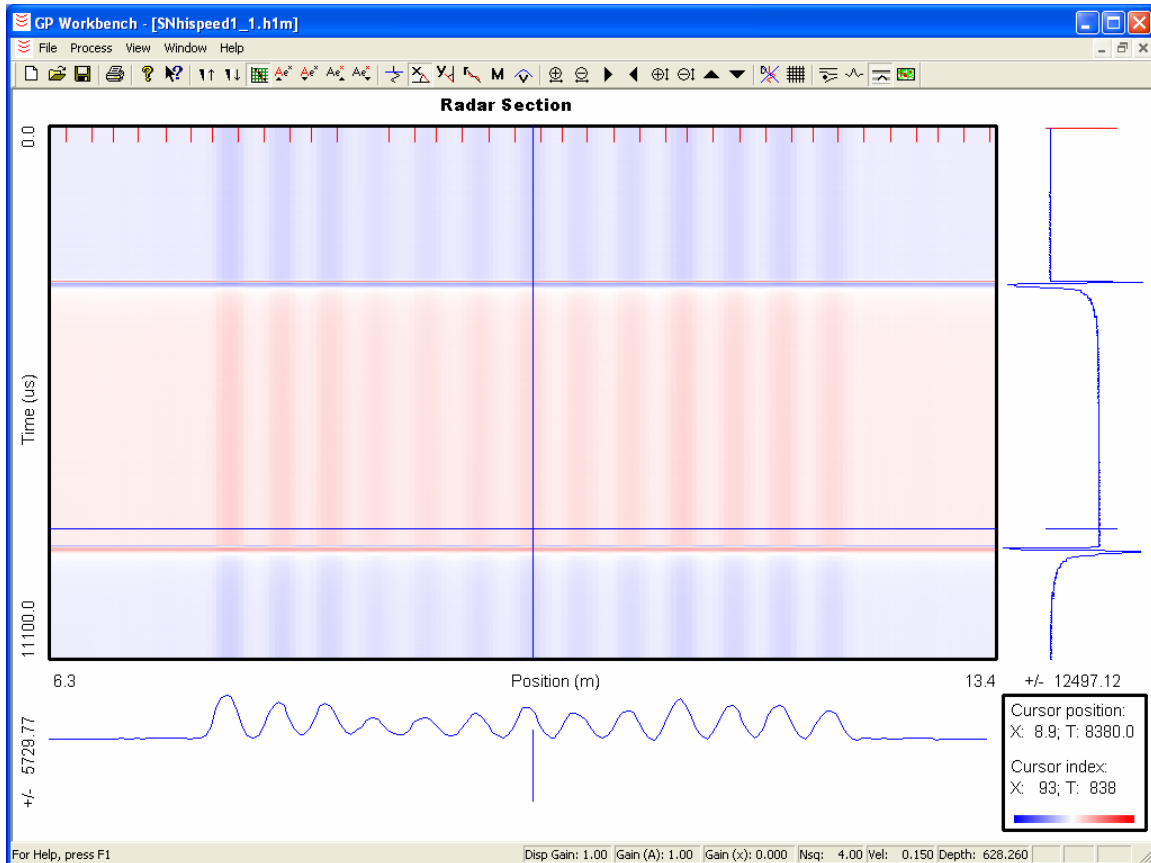


Figure 3.29. A screen shot of the *GP Workbench* processing package. ALLTEM data are shown in section view.

At the time of this report, the pre-processing and inversion are not complete. Our goal is to finish the program in time for processing ALLTEM data from our planned May, 2006 deployment to YPG.

The following steps outline the GP Workbench pre-processing steps required for raw ALLTEM data. The data from each ALLTEM survey line are recorded in multiple files – one file for each transmitting – receiving coil polarization.

Most of the utilities in GP Workbench process all of these files (or polarizations) in tandem. This significantly increases productivity. It may be necessary, depending on the survey method employed, to concatenate some data files before processing.

Current processing steps under development in GP Workbench:

1. Process calibration data to determine the calibration matrix \vec{k} (see Forward Model section in Section 4). A steel shot will be used as the calibration standard. The inverted UXO parameters such as dipole strength and aspect ratio will be with respect to the calibration standard. Calibration data should be recorded at the beginning and end of each survey.
2. Import data in section view and delete noisy records. Noisy records are usually the result of electromagnetic interference.
3. Convert from latitude and longitude to northing and easting using local UTM coordinates and then import data in plan view. Delete records with erroneous GPS positions. These erroneous positions can result from interference on the radio link between GPS components, and/or obstruction of GPS satellite signals due to buildings, hills, trees, etc. Alternatively, records with erroneous GPS positions can be relocated by interpolating between records with known good positions.
4. The ALLTEM system records waveform records more quickly than the JAVAD GPS system provided position updates. Therefore, records that are recorded between GPS position updates must have their positions calculated by interpolation. Each line in the survey data may require further positional adjustments depending on the direction of travel, and the location of the GPS antennas.
5. Remove the background response of the system electronics and the response from the soil. Each survey line should contain data recorded at the beginning and the end of the line where no targets exist. An interpolated waveform is calculated from the waveforms at the beginning and end of the line based on the distance between the beginning and end of the line. This interpolated waveform is subtracted from the data along the line as a function of position. It is assumed that the variation of soil properties is minimal over the length of the line, and that any change (drift) in the system response is linear over the length of the line. We have verified that the system drift over a few minutes is essentially linear after the system has been powered up for 15 minutes or more. After background subtraction, the remaining response is approximately that of the UXO target in a non-conducting-non-magnetic whole space.

6. Pick geophysical signal anomalies interactively or automatically. Extract data from the pre-processed waveforms for the inversion algorithm.

3.13 Ground Response

One of the difficulties with the VETEM system that we deployed to YPG in 2003 was that it was quite sensitive to the ground. We expected that ALLTEM would be entirely insensitive to the ground. At YPG ALLTEM was indeed much less sensitive to the ground than was VETEM, but the ground response is not zero. At the Denver Federal Center the measured ground response was, in fact, quite large, with measured amplitudes that sometimes exceeded 200 mV. At YPG the measured ground response amplitudes are generally less than 15 mV (see Figures 2, 4, 14, 15 in the paper “ALLTEM for UXO Applications – First Field Tests” in the appendix.) The lower ground response amplitudes at YPG pose little difficulty for shallow and large targets, but could set a lower limit on our ability to detect small and deep targets and will have some impact on our ability to derive accurate target parameters from our data for low amplitude targets. We previously attributed the earth response to electrical conductivity, but now think that ALLTEM is responding to magnetic susceptibility in the soil and rocks. If so, it is functioning as an active magnetometer. Preliminary modeling suggests that this is possible. More accurate modeling should settle the question. Whatever the mechanism, the earth response should ultimately be accounted for in inversion or discrimination algorithms, although we begin by ignoring it.

Since the amplitude of the ground response is clearly a strong function of height above the ground, we are examining the possibility of adding an array of acoustic or laser sensors to the cart and adding the outputs from these sensors to the data stream with the intention of accounting for, if not removing, ground response.

4.0 ALLTEM MODELING AND INVERSION

This section describes the data forward modeling and inversion algorithms that are being developed for the ALLTEM to estimate UXO parameters such as depth, attitude, aspect ratio, and composition. The following sections discuss the forward model and inversion algorithms.

4.1 Forward Model

A forward operator has been developed to approximate the response of a subsurface UXO. This operator describes the induced magnetic fields in the UXO in terms of three orthogonal magnetic dipole moments. A set of dipole moments is used to describe the induced magneto-static response, and another set is used to describe the induced electro-dynamic response. The forward operator A used in the inversion has the form

$$A([\mathbf{r}_{cart}, \mathbf{r}_{tx}, \mathbf{r}_{rx1}, \mathbf{r}_{rx2}, \mathbf{P}_{tx}, \mathbf{P}_{rx}, t], [\mathbf{r}_{s,uxo}, \phi_s, \theta_s, m_{s,1}, m_{s,2}, m_{s,3}, \mathbf{r}_{t,uxo}, \phi_t, \theta_t, m_{t,1}, m_{t,2}, m_{t,3}, \tau_1, \tau_2, \tau_3]) \\ = y([\mathbf{r}_{cart}, \mathbf{r}_{tx}, \mathbf{r}_{rx1}, \mathbf{r}_{rx2}, \mathbf{P}_{tx}, \mathbf{P}_{rx}, t])$$

where \mathbf{r}_{cart} is the location of the center of the ALLTEM cart, \mathbf{r}_{tx} , \mathbf{r}_{rx1} , and \mathbf{r}_{rx2} are the locations of the transmitting and receiving loops, \mathbf{P}_{tx} and \mathbf{P}_{rx} are the polarizations of the transmitter and receiver coils, t is time, and y are the simulated data. The UXO parameter set is listed in the second set of square brackets in the argument list of the forward operator, where $\mathbf{r}_{s,uxo}$ is the location of the UXO, $m_{s,1}$ - $m_{s,3}$ are the magnitude of the three orthogonal induced magneto-static dipole moments, ϕ_s and θ_s are the azimuth and inclination of the m_1 component, $\mathbf{r}_{t,uxo}$, $m_{t,1}$ - $m_{t,3}$, ϕ_t and θ_t are the analogous parameters for the transient electro-dynamic response, and τ_1 - τ_3 are the late time decay constants for the transient dipole moments. Separate sets of UXO parameters are used for the static and transient response to provide more information to better facilitate discrimination. This parameter set will be estimated by the inverse algorithm discussed below.

The forward model includes both the induced magneto-static response, and the electro-dynamic response from induced transient eddy currents. The magneto-static UXO response is modeled as three orthogonal magnetic dipoles, and the electro-dynamic response is modeled as three orthogonal exponentially decaying magnetic dipoles. It is assumed that the target and the ALLTEM cart are in a non-magnetic, non-conducting whole space. The modeled magneto-static induction at a receiver coil $\mathbf{B}_s(\mathbf{r})$ is calculated using

$$\mathbf{B}_s(\mathbf{r}) = \tilde{\mathbf{k}} \cdot \left[\frac{3\hat{\mathbf{R}}(\mathbf{m}_s \cdot \hat{\mathbf{R}}) - \mathbf{m}_s}{R^3} \right] \quad (4.1)$$

where $\tilde{\mathbf{k}}$ is a calibration matrix, \mathbf{r} is the location of the receiver, \mathbf{r}' is the UXO location, $\mathbf{R} = \mathbf{r} - \mathbf{r}'$, $R = |\mathbf{R}|$, $\hat{\mathbf{R}} = \mathbf{R} / R$, and \mathbf{m}_s is the static induced dipole moment. The static induced dipole moment is given by

$$\mathbf{m}_s = \begin{bmatrix} \mathbf{m}_{s,1} \hat{\mathbf{m}}_{s,1} & \mathbf{m}_{s,1} \hat{\mathbf{m}}_{s,2} & \mathbf{m}_{s,1} \hat{\mathbf{m}}_{s,3} \\ \mathbf{m}_{s,2} \hat{\mathbf{m}}_{s,1} & \mathbf{m}_{s,2} \hat{\mathbf{m}}_{s,2} & \mathbf{m}_{s,2} \hat{\mathbf{m}}_{s,3} \\ \mathbf{m}_{s,3} \hat{\mathbf{m}}_{s,1} & \mathbf{m}_{s,3} \hat{\mathbf{m}}_{s,2} & \mathbf{m}_{s,3} \hat{\mathbf{m}}_{s,3} \end{bmatrix} \cdot \mathbf{H}_p(\mathbf{r}') \quad (4.2)$$

where $\mathbf{H}_p(\mathbf{r}')$ is the primary magnetic field, and the three induced magnetic moments are related by

$$\hat{\mathbf{m}}_2 = \hat{\mathbf{m}}_1 \times \hat{\mathbf{z}} \text{ and } \hat{\mathbf{m}}_3 = \hat{\mathbf{m}}_1 \times \hat{\mathbf{m}}_2 \quad (4.3)$$

The primary field $\mathbf{H}_p(\mathbf{r}')$ at the UXO location is calculated using the Biot-Savart Law (Jackson, 1999) for the 1-meter square loop transmitting coils. Similar relationships are used to model the electro-dynamic induction at a receiver coil,

$$\mathbf{B}_t(\mathbf{r}) = \tilde{\mathbf{k}} \cdot \left[\frac{3\hat{\mathbf{R}}(\mathbf{m}_t(t) \cdot \hat{\mathbf{R}}) - \mathbf{m}_t(t)}{R^3} \right] \quad (4.4)$$

$$\mathbf{m}_t(t) = \begin{bmatrix} \mathbf{m}_{t,1}\hat{\mathbf{m}}_{t,1}e^{-t/\tau_1} & \mathbf{m}_{t,1}\hat{\mathbf{m}}_{t,2}e^{-t/\tau_1} & \mathbf{m}_{t,1}\hat{\mathbf{m}}_{t,3}e^{-t/\tau_1} \\ \mathbf{m}_{t,2}\hat{\mathbf{m}}_{t,1}e^{-t/\tau_2} & \mathbf{m}_{t,2}\hat{\mathbf{m}}_{t,2}e^{-t/\tau_2} & \mathbf{m}_{t,2}\hat{\mathbf{m}}_{t,3}e^{-t/\tau_2} \\ \mathbf{m}_{t,3}\hat{\mathbf{m}}_{t,1}e^{-t/\tau_3} & \mathbf{m}_{t,3}\hat{\mathbf{m}}_{t,2}e^{-t/\tau_3} & \mathbf{m}_{t,3}\hat{\mathbf{m}}_{t,3}e^{-t/\tau_3} \end{bmatrix} \cdot \mathbf{H}_p(\mathbf{r}') \quad (4.5)$$

where τ_1 - τ_3 are the late time decay constants. To calculate the ALLTEM response to a UXO target using a given loop polarization, the primary field $\mathbf{H}_p(\mathbf{r}')$ is calculated at the UXO location for the relevant transmitting loop and the B fields at the relevant receiver loop locations are calculated. Each transmitter coil is modeled as a 1-meter square loop. For a given measurement, the ALLTEM uses two receiver coils to make a differential measurement. The B fields at each coil location are subtracted to model the differential measurement. Each receiver coil is approximated as an ideal small dipole located at the center of the actual coil. The error introduced by this approximation increases as the distance between a receiver coil and the UXO decreases, and as the area of the receiver coil increases.

Using this forward operator, the simulated fields for various UXO targets can be simulated. For example, Figures 4.1 - 4.6 show the magneto-static fields simulated for targets listed in Table 4.1. To generate these figures, data were calculated for cart positions located on a grid two meters on each side and a simulated UXO target located beneath the center of the grid. The aspect ratios listed in Table 4.1 compare the length of the target to its width. Note that the synthetic data shown in these plots have a zero noise level.

Table 4.1. List of UXO attributes used to generate synthetic data shown in Figures 4.3-4.8. Azimuth and inclination are in degrees, and depth is in cm.

Description	Aspect ratio	Azimuth	Inclination	Depth	Figure
Vertical rod	5:1	0	90	25	4.1
Horizontal rod	5:1	45	0	25	4.2
Oblique rod	5:1	10	10	25	4.3
Oblique rod	5:1	45	45	25	4.4
Ball	1:1	0	0	25	4.5
Horizontal disk	1:5	45	0	25	4.6

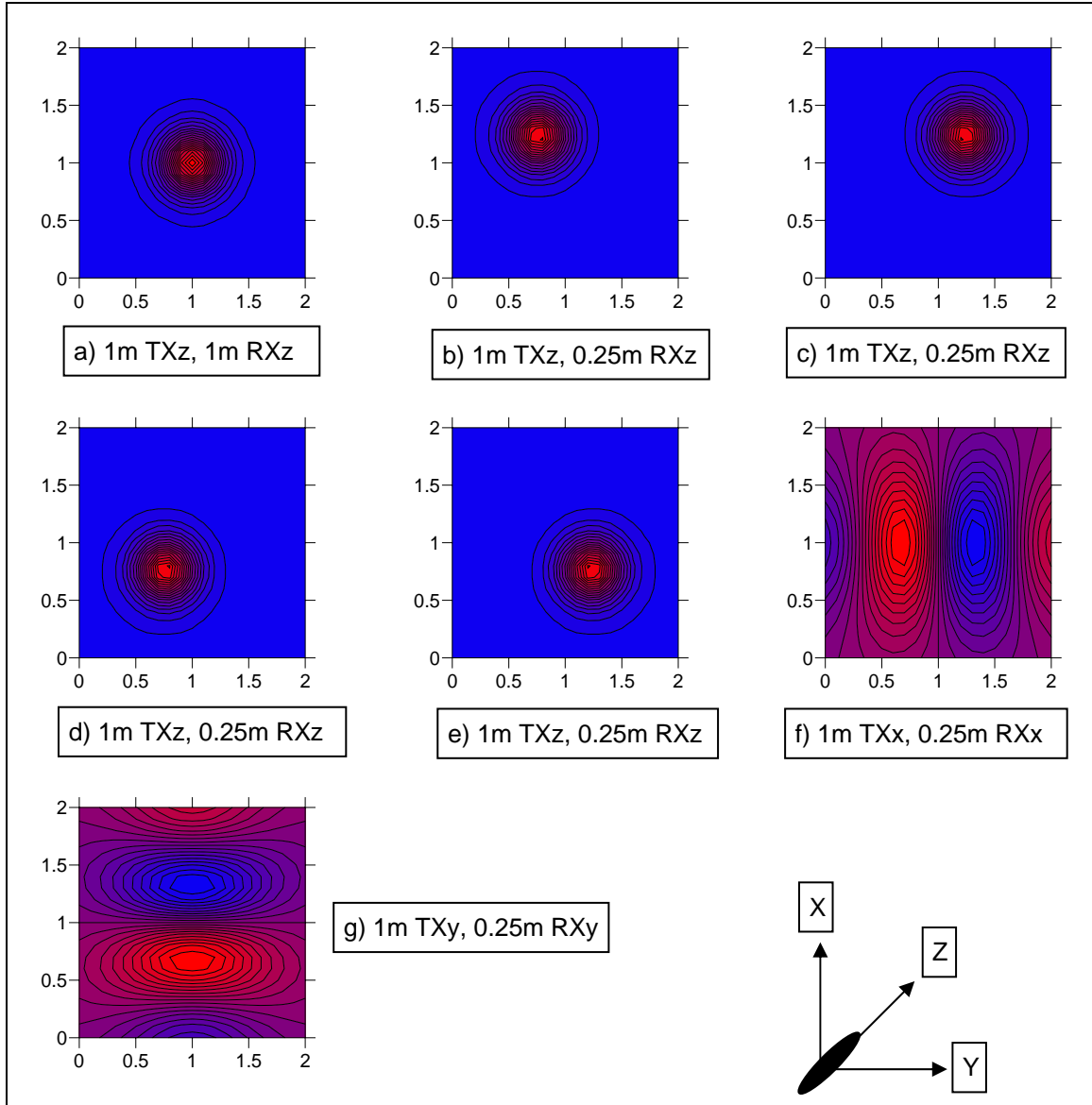


Figure 4.1. Simulated ALLTEM magneto-static response for a vertical rod-like structure. The length of the rod is five times its width. The response is shown for five different vertically polarized coil sets, and two different horizontal sets. Note the symmetric response by the different components. The response of the 1-m vertical gradient receiver is truly symmetric to the system whereas the 0.25-m vertical gradients are slightly offset according to their respective locations.

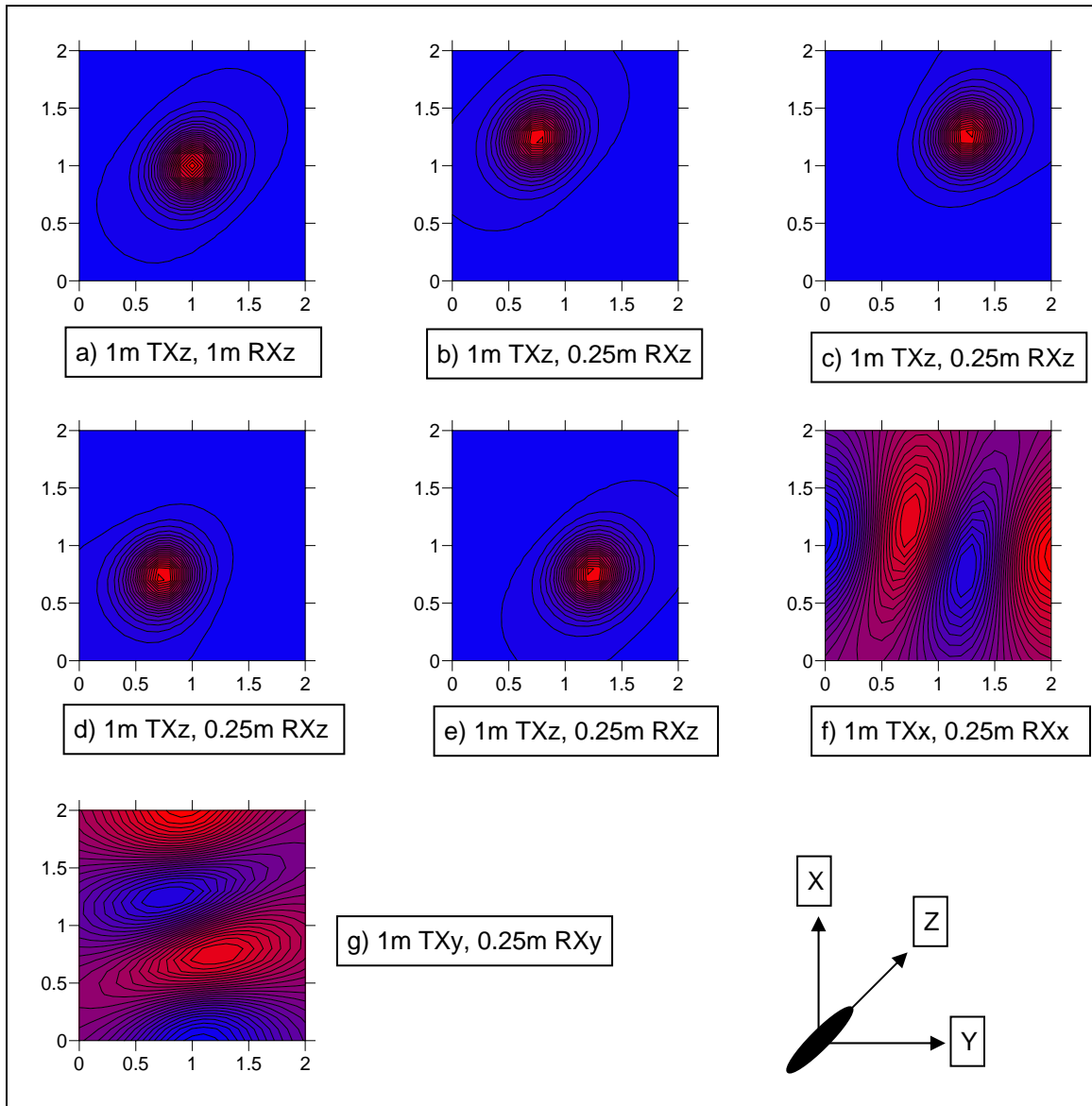


Figure 4.2. Simulated ALLTEM magneto-static response for a horizontal rod-like structure at an azimuth of 45 degrees. The length of the rod is five times its width. The response is shown for five different vertically polarized coil sets, and two different horizontal sets. Note the oriented response in both the vertical and horizontal components.

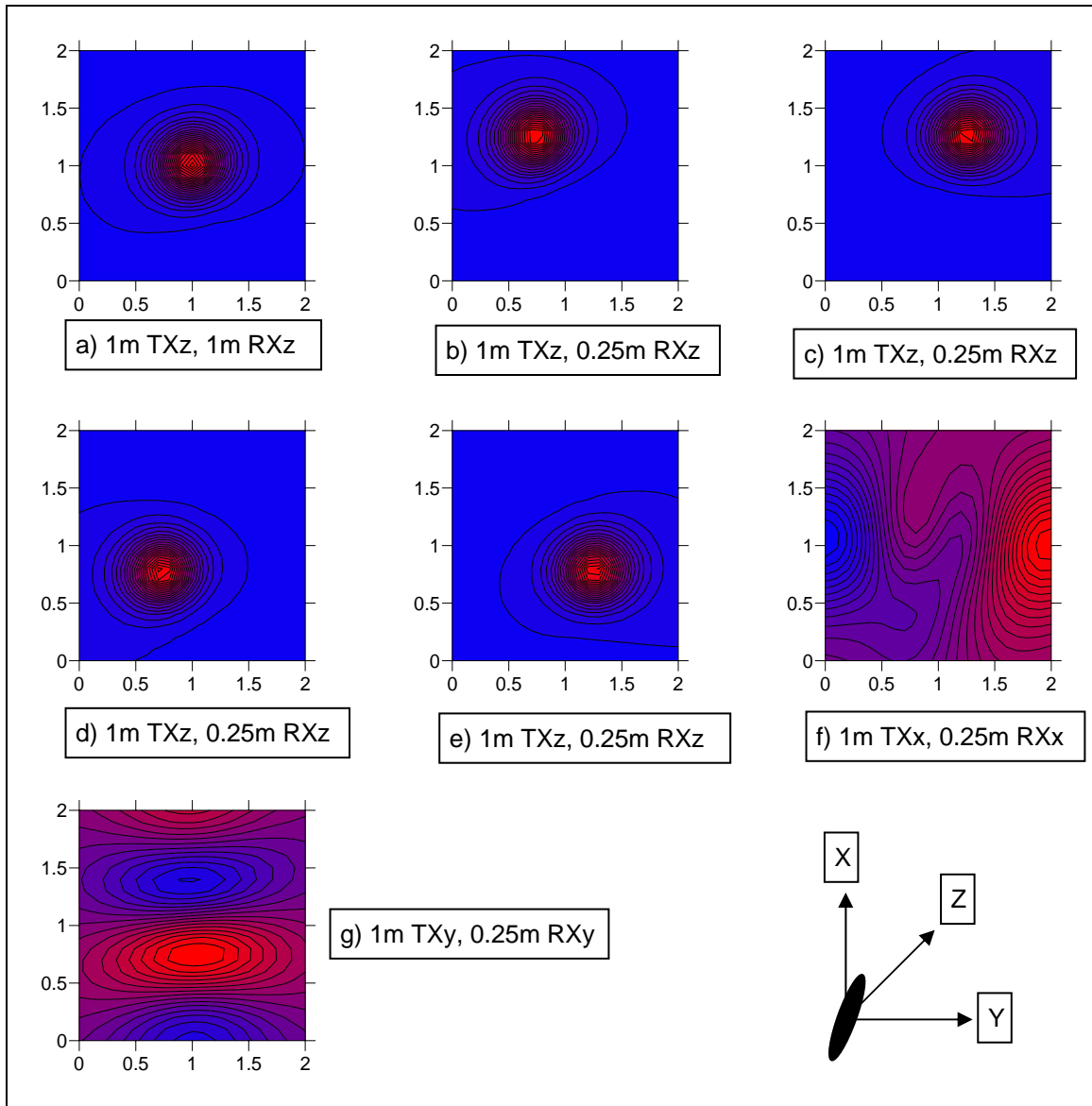


Figure 4.3. Simulated ALLTEM magneto-static response for a rod-like structure at an inclination of 10 degrees and at an azimuth of 10. The length of the rod is five times its width. The response is shown for five different vertically polarized coil sets, and two different horizontal sets. Note the oriented response in both the vertical and horizontal components.

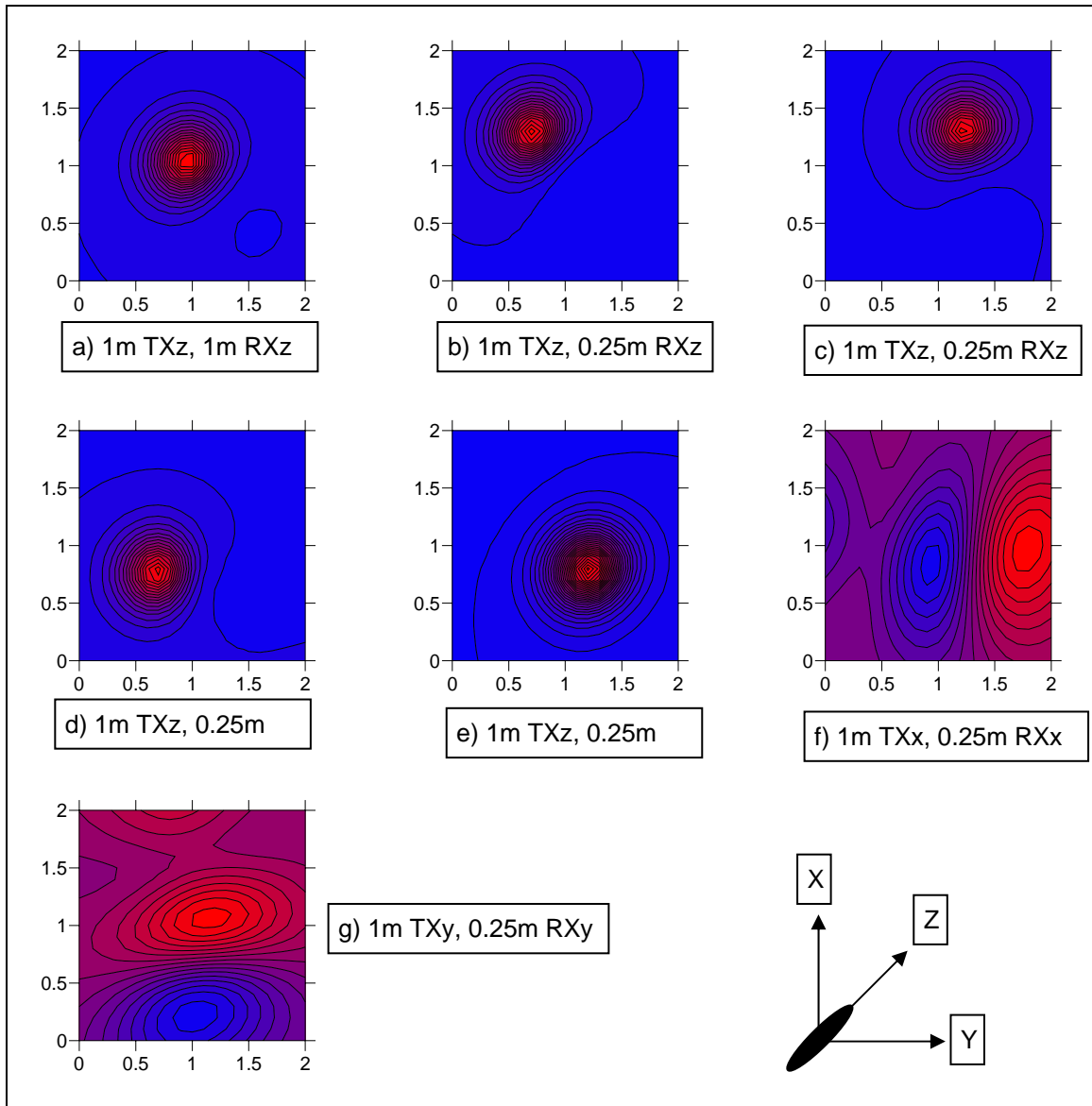


Figure 4.4. Simulated ALLTEM magneto-static response for a rod-like structure at an inclination of 45 degrees and at an azimuth of 45. The length of the rod is five times its width. The response is shown for five different vertically polarized coil sets, and two different horizontal sets. Note the oriented response in both the vertical and horizontal components.

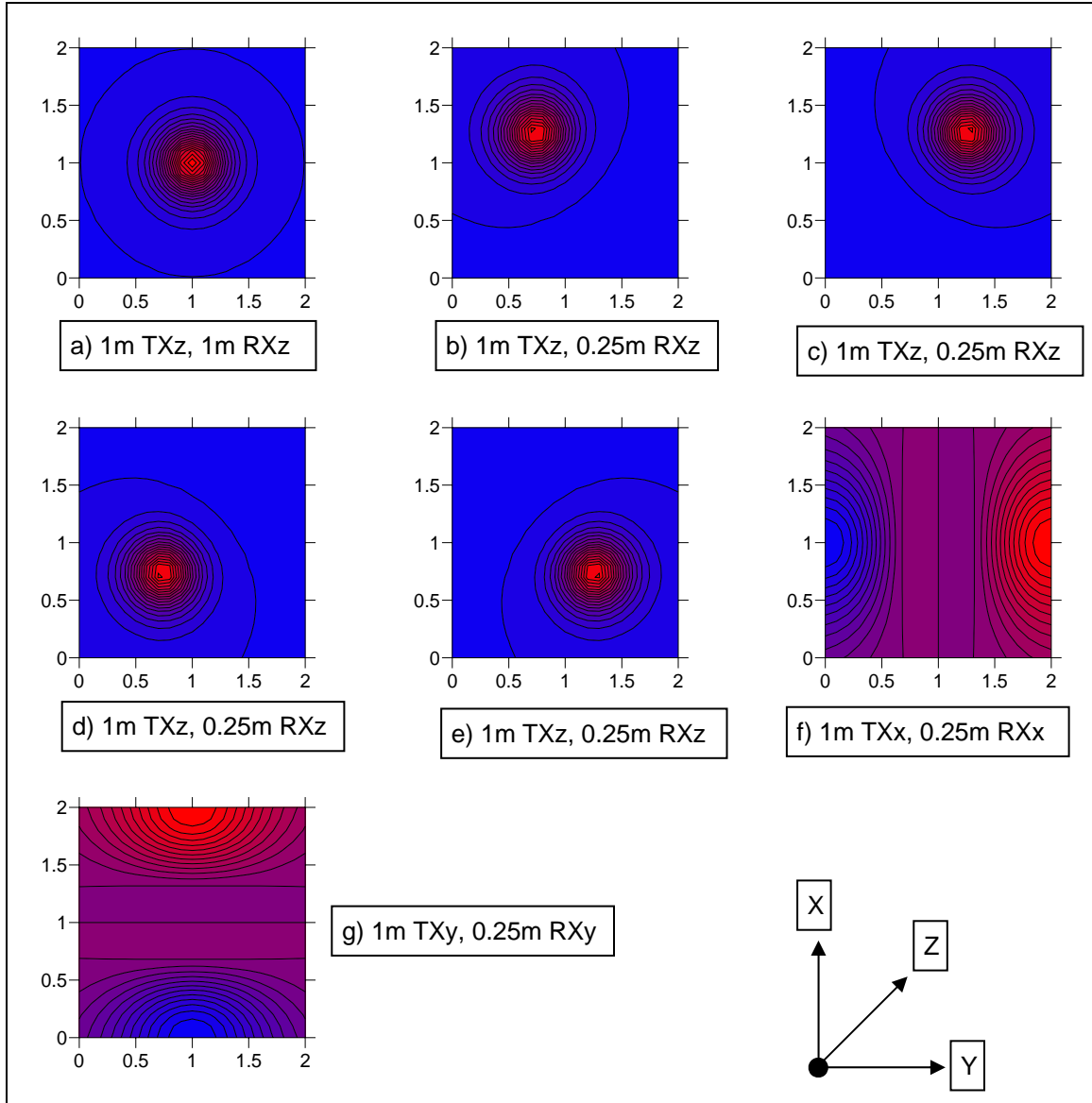


Figure 4.5. Simulated ALLTEM magneto-static response for a ball-like structure. The response is shown for five different vertically polarized coil sets, and two different horizontal sets. Note the symmetric responses for the horizontal components and the vertical 1-m loop receiver and the slightly offset responses for the small vertical loop receivers.

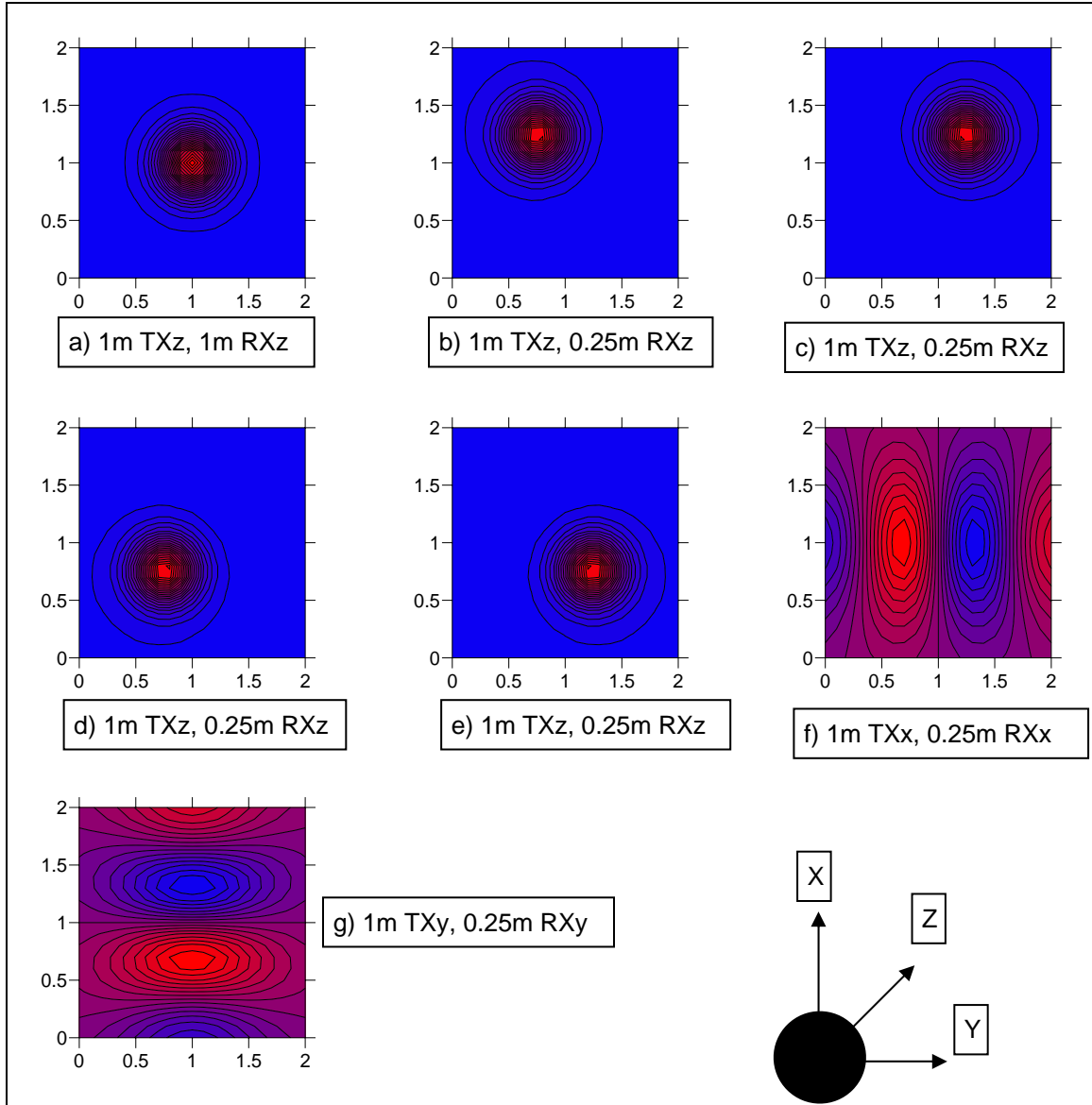


Figure 4.6. Simulated ALLTEM magneto-static response for a horizontal disk-like structure. The width of the disk is five times its height. The response is shown for five different vertically polarized coil sets, and two different horizontal sets. Note the difference between the 1-m vertical gradient response in Figure 4.5a and 4.6a above.

4.2 Inversion Algorithm

The forward operator generates a data set that can be compared with survey data to invert for UXO parameter estimates. For a given UXO target, a small data set is extracted from the field data set for use in the inversion. During a survey, the ALLTEM system records the response of various transmitting and receiving loop combinations, at successive positions along a survey line. A survey generally consists of a collection of survey lines. A small data set for an individual target is made by extracting received waveforms with locations inside a window over the target as shown in Figure 4.7. For

each waveform, three data points are extracted. One point is extracted for the static response, and two points are extracted for the transient response (see Figure 4.8). The transient points are taken at 10% and 25% of the peak value so that late time decays are measured. The resulting data set for a given target is made up of the three waveform points extracted from waveforms recorded at various ALLTEM cart locations using various coil polarizations. For a standard survey, using 50 cm line spacing, 20 cm between each record along each line, and seven different polarization combinations of the transmitting and receiving loops, there will be about 350 waveforms and 1050 data points that can be used to estimate 19 parameters.

During the early-time transient response, the induced dipole moments are oriented parallel to the primary magnetic field. The induced eddy currents will attenuate quickly if the cross sectional area of the currents in the target is small. Conversely, the induced currents will decay slowly if the cross sectional area containing the currents is large. Therefore, the late-time transient data contains information about the orientation of the large area conductive planes in the target, and the targets aspect ratio (length to width ratio). For these reasons, late-time data are used in the forward model and inversion, and early-time data are not processed.

The inverse algorithm uses the Gauss-Newton (Gill et al., 1996; Zhdanov, 2002) method to reduce the RMS difference between the predicted data and the measured data. This RMS difference is referred to as the objective function. The predicted data are calculated using the forward operator with an initial set of UXO parameters, and the value of the objective function is calculated. The inversion algorithm then chooses a new set of UXO parameters by moving in the down gradient direction of the objective function. The value of the objective function using the new parameter set will (usually) be less than the value using the initial parameter set. This process is repeated until the objective function is minimized. An acceptable solution (i.e. UXO parameter set) to the inverse problem is reached when the RMS difference between the predicted data and the actual data is less than the RMS noise level in the data. Since this is a non-linear problem, it is possible that the UXO parameter set determined by the inversion algorithm is located at a local minimum of the objective function rather than a global minimum. The parameter set at a local minimum may not be an acceptable solution to the inverse problem, and may have markedly different values than the parameter set at the global minimum. To solve this problem, the inversion is performed with many initial parameter sets starting at different locations in parameter space. An attempt is made with each initial model to obtain an acceptable solution to the inverse problem. In general, an acceptable solution cannot always be found for each initial model. Given a suitable number of initial models, and a noise level that is above some portions of the objective function topography, some acceptable solutions will be found.

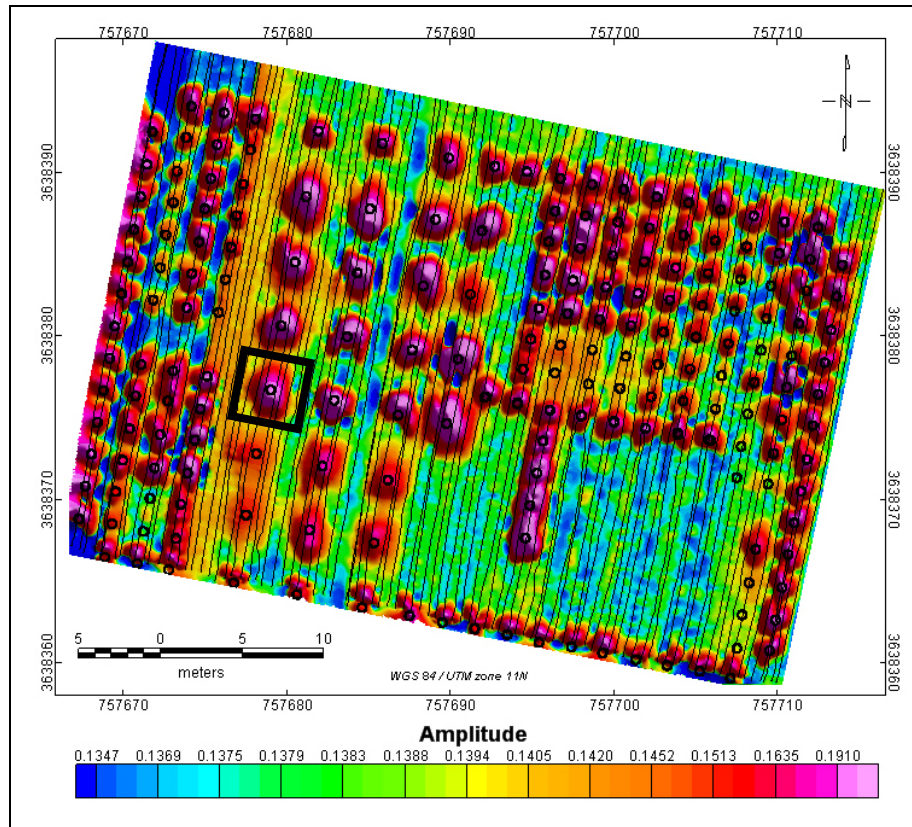


Figure 4.7. ALLTEM data from the YPG UXO Calibration Grid. Data are for 1-meter square vertically polarized transmitter and receiver coils. A data set for an individual target is made by extracting received waveforms with locations inside a window over the target as shown.

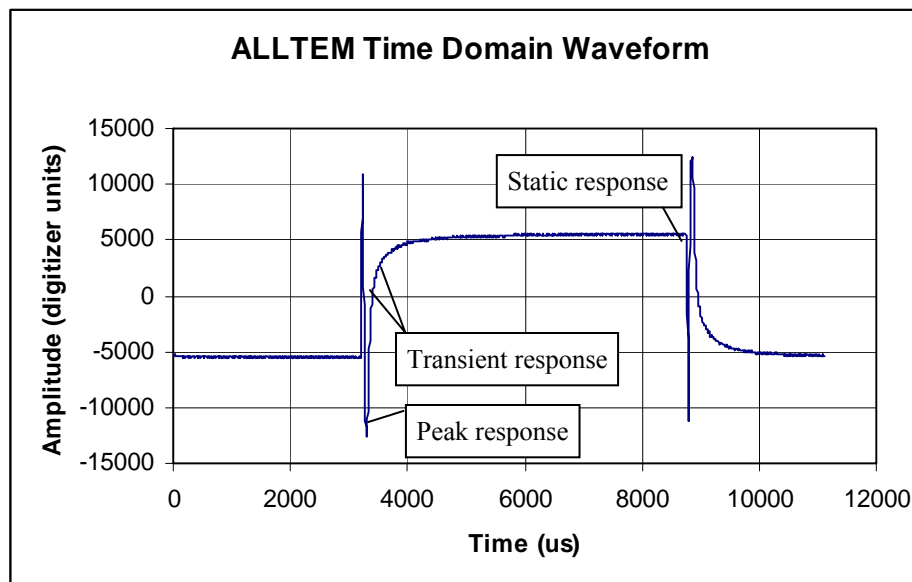


Figure 4.8. ALLTEM time domain waveform. One data point is extracted for the static response, and two data points are extracted for the transient response.

The final solution is calculated by averaging the results from the set of acceptable solutions. This inversion scheme has been used successfully for other non-linear problems (Oden, 2006; Oden et al. 2006). Currently, the inversion algorithm has not been completely implemented, but our goal is to have it operational for the next planned survey at the YPG in May, 2006.

The RMS noise in the data has several components. They are system noise from the electronics and sensors, electromagnetic interference, the response from varying electromagnetic properties of the soil, the response to topography, and the response due to changing attitude of the cart. Before inverting the extracted target data set, data points are removed from the set if their amplitude is less than the noise level. This makes the inversion less susceptible to noisy data. We chose not to weight data according to their signal to noise ratio, because this would possibly de-weight some data points that contain valuable information about the targets.

It should be noted that the inversion algorithm provides estimates of the UXO parameter set described in the discussion above on the forward model. The inversion algorithm does not attempt to identify specific targets. A library should be compiled that maps specific UXO types to the UXO parameter set estimated by the inversion. The aspect ratio of the targets is determined from the three components of the induced magnetic moment. If one component is significantly larger than the others, then the target is rod-like. If one component is significantly smaller than the others, then the target is disk-like. If all components have similar magnitudes, then the target is ball-like. A separate location and attitude of the induced dipole moments are determined for the magneto-static response and for the electro-dynamic response. Therefore, it may be possible to compare these locations and attitudes to better discriminate and identify targets when *a priori* information about the targets is known.

4.2.1 Sensitivity Analysis

A preliminary sensitivity analysis has been made to estimate the performance of the inversion algorithm for the magneto-static response. Synthetic data generated by forward modeling were used to estimate the sensitivity of various model parameters to noise and measurement uncertainties. Data were generated for a 2-meter square grid using a 20 cm interval in the x direction (along survey lines), and a 50 cm interval in the y direction. The location of the survey positions is shown in Figure 4.9 for a typical target. Tables 4.2 and 4.3 list locations in UXO parameters space where the sensitivities were determined. The simulated data with a 1:1 aspect ratio are representative of a steel shot with a diameter of 8.9 cm such as those buried at the YPG. The data with an aspect ratio of 5:1 are representative of an 81 mm M374 ordinance.

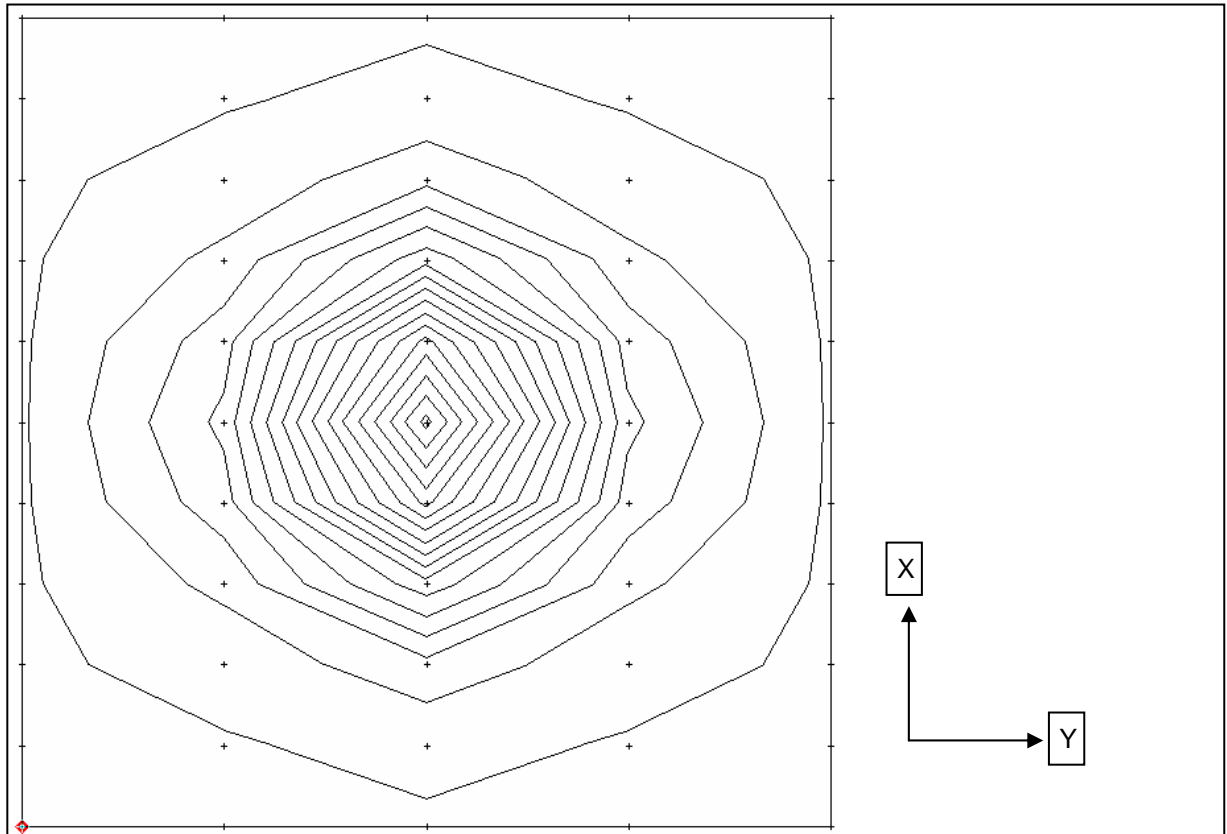


Figure 4.9. Cart locations used to generate synthetic data. Contours show a typical response to a vertical target under the center of the survey grid measured by the 1-m vertical gradient receiver. These simulated locations represent five survey lines along the x direction.

Table 4.2. Parameter sensitivities using only the vertical polarizations. Depth is in cm, and azimuth and inclination are in degrees.

Target Parameters				Parameter Uncertainty (+/-)			
Depth	Aspect ratio	Az./Inc.	Comment	Depth	Aspect ratio	Az./Inc.	Num. data
10	5:1	0/90	vert. rod	0.06	?	10.6/23.0	166
10	5:1	45/0	hor. rod	0.02	0.07	7.4/8.7	251
10	5:1	10/10	oblique rod	0.21	0.08	5.8/11.9	248
10	5:1	45/45	oblique rod	0.88	0.21	13.7/7.9	161
10	1:1	0/0	ball	0.09	0.08	?/14.6	107
10	1:5	45/0	hor. disk	0.18	0.07	?/8.8	257
25	5:1	0/90	vert. rod	1.3	?	60.3/79.2	113
25	5:1	45/0	hor. rod	5.6	0.42	24.4/34.0	201
25	5:1	10/10	oblique rod	5.5	0.48	26.3/28.5	199
25	5:1	45/45	oblique rod	30.1	1.1	78.7/12.5	120
25	1:1	0/0	ball	16.4	0.23	?/?	81
25	1:5	45/0	hor. disk	0.18	0.51	?/39.4	237
50	5:1	0/90	vert. rod	5.0	?	?/35.6	47
50	5:1	45/0	hor. rod	18.7	2.0	27.7/38.2	141
50	5:1	10/10	oblique rod	85.4	3.4	32.7/34.0	140
50	5:1	45/45	oblique rod	145	6.3	?/24.7	131
50	1:1	0/0	ball	70.0	?	?/?	99
50	1:5	45/0	hor. disk	6.7	1.4	?/41.4	129

Table 4.3. Parameter sensitivities using both vertical and horizontal polarizations.

Target Parameters				Parameter Uncertainty (+/-)			
Depth	Aspect ratio	Az./Inc.	Comment	Depth	Aspect ratio	Az./Inc.	Num. data
10	5:1	0/90	vert. rod	0.31	?	9.0/19.5	261
10	5:1	45/0	hor. rod	0.07	0.06	6.2/7.4	359
10	5:1	10/10	oblique rod	0.19	0.07	4.9/10.1	358
10	5:1	45/45	oblique rod	0.77	0.18	11.6/6.7	270
10	1:1	0/0	ball	0.32	0.07	?/12.3	197
10	1:5	45/0	hor. disk	0.16	0.06	?/7.4	351
25	5:1	0/90	vert. rod	1.4	?	50.9/67.0	210
25	5:1	45/0	hor. rod	4.7	0.35	20.6/28.7	309
25	5:1	10/10	oblique rod	4.7	0.41	22.3/24.1	308
25	5:1	45/45	oblique rod	25.4	0.91	66.5/10.6	229
25	1:1	0/0	ball	13.9	0.16	?/?	167
25	1:5	45/0	hor. disk	0.33	0.43	?/33.3	331
50	5:1	0/90	vert. rod	5.3	?	?/31.1	134
50	5:1	45/0	hor. rod	15.9	1.7	23.5/32.3	249
50	5:1	10/10	oblique rod	72.2	2.9	27.7/28.7	249
50	5:1	45/45	oblique rod	123	5.3	?/21.0	236
50	1:1	0/0	ball	59.2	3.1	?/?	179
50	1:5	45/0	hor. disk	5.7	1.1	?/35.0	223

The resolution of the inversion algorithm is estimated as follows. For a given datum y_i , the sensitivity to the UXO parameters x at a specified location in UXO parameter space is given by

$$\Delta y_i = \sum_j J_{i,j} \Delta x_j \quad (4.6)$$

where $J_{i,j} = \partial y_i / \partial x_j$ is the Jacobian. Similarly, the sensitivity of each UXO parameter to the data is

$$\Delta x_j = \sum_i S_{j,i} \Delta y_i. \quad (4.7)$$

where $S_{j,i} = \partial x_j / \partial y_i$ (to first order). An estimate of the UXO parameter resolution is given by

$$\sigma_{x,j}^2 = \frac{1}{N_i} \sum_i (S_{j,i} \sigma_{y,i})^2, \quad (4.8)$$

where $\sigma_{y,i}$ is the RMS noise of the i th datum y_i , and $\sigma_{x,j}$ is the RMS uncertainty in the j th UXO parameter estimate x_j . The Jacobian $J_{i,j}$ and sensitivity $S_{j,i}$ parameters are calculated numerically from the forward model. This simple formulation assumes that the noise in the data is uncorrelated, which is almost certainly not the case for some noise components such as topography.

To estimate the RMS noise level in a typical data set, the YPG data collected in October, 2005 were examined. ALLTEM measurements of buried steel shots were made near lane one of the YPG Calibration grid. These shots were buried at a depth of 20 cm and have a radius of 8.9 cm. The noise level due to electronic noise, electromagnetic interference, topography, and the changing electromagnetic properties of the soil was estimated to be two percent of the peak signal level measured above the steel shots. An RMS noise level for synthetic data was estimated as two percent of the peak signal level of the simulated data for a spherical target (i.e. an aspect ratio of 1:1) at a depth of 20 cm. When calculating the uncertainty values listed in Tables 2 and 3, any synthetic data values with a magnitude less than the synthetic RMS noise level were removed before applying Equation 4.8.

4.3 Discussion

Some generalizations can be made based on the results shown in Tables 4.2 and 4.3, from the forward operator relationships, and from the mechanisms used in the inverse algorithm.

1. Deeper targets produce fewer data points above the noise level. The RMS uncertainties for the UXO parameter estimates are larger for deeper targets. The UXO parameters for targets on the order of 9 by 40 cm that are deeper than 50 cm are not resolvable at the noise levels observed in the data examined for this analysis. Deeper targets can be located, but the data quality is insufficient to facilitate inversion for parameter estimates.
2. Under the assumption that all sensitivity $S_{j,i}$ parameters have similar values, the RMS uncertainty in the UXO parameter estimates will decrease as $1/\sqrt{N_i}$ where N_i is the number of data points collected. The number of data points can be increased by using a more dense survey grid, and/or collecting data using more polarization combinations from the ALLTEM coils. Collecting more data on a more dense survey grid increases survey time. In practice, the $S_{j,i}$ parameters do

not all have similar values, but the inverse square root relationship does provide useful insight.

3. Reducing the RMS noise level and increasing the signal level can increase the depth to which useful UXO parameter estimates can be obtained. The signal level could be increased with more primary field energy, but significant increases in driving current would be difficult to achieve from an engineering standpoint. A somewhat larger vertical axis transmitting coil might be worthwhile and possible. Non-coherent system noise and electromagnetic interference can be reduced by increasing the number of stacks used when acquiring data, but this slows data acquisition and additional stacking is thus practical only in cued mode. It is likely that the response due to changes in topography, cart attitude, and variations in the electromagnetic properties of the soil can be reduced by adding additional sensors to the cart to record topography and cart attitude. The signal-to-noise ratio (SNR) could also be increased by placing the cart closer to the ground, but we are already near a practical minimum on all but the smoothest ground. For some of our data digital filtering to remove some high frequency coherent system noise and external VLF radio station noise considerably improves the SNR.
4. Figures 4.1-4.6 indicate that the horizontal components contain valuable information regarding target attitude. Unfortunately, the signals from horizontal component coils at depth are weaker than the vertical components, and have a smaller signal to noise ratio, however see our discussion in Section 7.4 below. Tables 4.2 and 4.3 show that adding these components reduces uncertainty in the UXO parameter estimates, but not markedly. It is anticipated that adding more measurements using different coil polarizations will incrementally reduce the uncertainty.
5. Target azimuth can not be estimated when the target has radial symmetry such as a vertical rod-like structure or a horizontal disk-like structure. It is only possible to determine a target's azimuth over a range of 0-180 degrees, and inclination over 0-90 degrees. It is not possible, for instance, to determine whether the tail of a target is pointing up or down. By estimating a separate parameter set for the magneto-static and for the electro-dynamic UXO parameters, and having some prior knowledge about the targets, it may be possible to better estimate the attitude of some targets.
6. The uncertainty in the estimated aspect ratios increases when the induced dipole moments are aligned with the polarizations of the ALLTEM coils.
7. Since the amplitude of the electro-dynamic response is similar to the magneto-static response, similar resolution of electro-dynamic parameters is expected from the inversion algorithm.
8. The uncertainties listed in Tables 4.2 and 4.3 assume a locally linear forward operator. The actual forward operator is non-linear, which may pose difficulty in

finding a solution(s). The character of the objective function (RMS difference between the predicted data and the actual data) has not been studied. The objective function may have several or many local minima. The nature of the objective function will determine how difficult it is and how much searching in UXO parameter space is needed to find an acceptable solution set. It is possible that a solution set may extend across multiple basins of attraction, leading to a less-unique solution.

9. To date, the effects of positional errors of the ALLTEM cart have not been studied. Positional errors will detract from the accuracy and increase uncertainty associated with the inverse solution.

4.4 Further Steps

Remaining tasks in the development of the inversion algorithm and the *GP Workbench* package include:

1. Finish the data preprocessor. Allow for importing, opening, saving of all polarizations of an ALLTEM data set in tandem. The tandem processing will allow for deleting traces, interpolating and adjusting GPS positions, and applying filters to all polarizations. This step is nearing completion.
2. Write a forward modeler for late time electro-dynamic (transient) response. Since the electro-dynamic forward operator is very similar to the magneto-static operator, implementation should be straightforward.
3. Finish the inversion algorithm. The inversion algorithm for the magneto-static response is nearing completion. Adding the inversion for the electro-dynamic response will be straightforward. The ALLTEM inversion algorithm is being adapted from existing routines that have been proven to work with non-linear inverse problems (Oden, 2006; Oden et al., 2006). Much of the existing code will be re-used.
4. There are many possible coil polarization combinations that can be used when making an ALLTEM survey. However, only a limited number (seven receiver coil combinations per transmitter coil) of coil combinations can be recorded. A sensitivity analysis will be performed to determine the optimal coil polarizations to use when collecting data. *GP Workbench* currently handles seven polarization combinations. Additional combinations will need to be implemented in pre-processing, calibration, forward modeling, and inversion.
5. Add a processing history window and associated text file with each data set. The results from pre-processing, filtering, and the inversion algorithm will be written to this file.

6. Integrate *GP Workbench* with *OASIS Montaj*. Code exists for reading/writing *OASIS Montaj* data files.

4.5 Conclusions

A user-friendly data processing and inversion and software package is being developed for the ALLTEM system. This package includes utilities for pre-processing raw data, system calibrations, forward modeling of UXO targets, inversion for UXO properties, graphical user interaction, and production of publication quality images. The inversion algorithm will aid in the discrimination of possible UXO targets. The inversion algorithm is based on a simple dipole model for the UXO target. The data processing and inversion algorithms are not yet complete, but we plan to have these modules operational for our YPG surveys scheduled for May, 2006.

Preliminary results indicate that useful parameter estimates can be made for shallow targets. The practical depth limit will be target dependent and will not be fully known until the processing and inversion package has been completed and applied to our 2005 and upcoming 2006 field data. In order to obtain useful parameter estimates for deeper targets, the SNR of the measurements must be increased. Future goals include increasing the SNR by decreasing noise due to topography, system-generated noise, and variations in soil properties and by adding more simultaneously recorded polarization channels.

5.0 TMGS DATA AND ANALYSIS

5.1 Overview

A series of field experiments with the TMGS were conducted at YPG from Oct. 28 through Nov. 15, 2006. The experimental regimen included:

1. Spin calibrations,
2. Lag and heading error calibrations,
3. Towed surveys over the Calibration Grid,
4. Cued, high-density surveys over 60 mm and 81 mm targets, and
5. Towed, high-density survey over 20 mm target.

The two main objectives were met: to obtain high-quality data from several complete spin calibration, and to completely survey the Calibration Grid with the towed array. In addition, other significant experiments were completed. This report discusses the experimental field procedures and the current status of data reduction and processing.

5.2 System Description

The TMGS hardware and software, described in detail in past reports, will be briefly summarized here. The system block diagram in Figure 5.1 depicts five major system components:

1. The towed platform, consisting of the magnetometer array and mechanical mounts (Figure 5.2), temperature sensors, inclinometer, accelerometers, the GPS receiver antenna, and the nonmagnetic, three-wheeled cart;
2. The legacy magnetometer interface electronics, housed in a temperature regulated case (Figure 5.3);
3. The PC-based National Instruments (NI) data acquisition system, and the power system, all mounted on the prime mover (Figure 5.3);
4. The GPS base station, made up of a tripod mounted GPS receiver, a radio telemetry unit, and a battery power source (Figure 5.4); and
5. The computer workstation, which is a desktop computer having software for data conversion and post-processing TMGS data, and with Oasis montaj for displaying GPS coverage and magnetic maps. The workstation was maintained off-site at the motel.

All together, the complete system is illustrated in Figure 5.5 as it surveyed the Calibration Grid.

Not shown in the block diagram is the magnetic reference base station, which typically consists of a G-858 magnetometer, two sensor heads mounted on a vertical pole, and an external battery. These data are logged internally for later download to a portable computer. While a magnetic reference station is not strictly required for full TMGS operation, it is employed as an experimental control during this research and development.

5.3 Spin Calibrations

For the array of four 3-axis fluxgate magnetometers to perform as a magnetic gradient tensor device, it is essential to remove inherent misalignments and to obtain accurate transfer functions for the conversion of raw data in volts to magnetic field measurements in nanoteslas.

5.3.1. *Field Procedures and Data Acquisition*

First, a reconnaissance survey was completed over possible magnetically clean and quiet areas of the STS. An operator packing the Leica GPS system walked the areas with the G-858 cesium magnetometer in gradiometer mode. These data were downloaded and processed in the command trailer. Three locations were identified on the resulting maps which displayed very small horizontal and vertical magnetic gradients. These locations were re-surveyed with the G-858 on a high-resolution grid. A prime location for the spin calibration experiments was found approximately 100 m south of the Blind Test Grid. This location was also suitable for the magnetic reference base station.

The spin calibration apparatus consists of four main components:

1. A motor drive assembly, in which a small, high-torque, gear head dc-motor transmits power through a 50:1 gear box to a V-belt pulley;
2. An intermediate stage of ganged V-belt pulleys which reduces the rotation by a factor of 6;
3. A pulley-driven turntable mounted on a sturdy base that has 3-point leveling; and
4. A lectern on which the magnetometer array is mounted.

The entire apparatus is shown in Figure 5.6 as it was set up for a calibration run. Except for the dc motor and gear box on the stand farthest away from the array, all materials are nonmagnetic. Magnetic signature tests with a G-858 magnetometer verified that at the separation distance (greater than 3 m), no magnetic noise was detectable at the array location. A close-up photograph of the lectern is shown in Figure 5.7. The data acquisition system was stationed about 10 m away (Figure 5.8), where the operator directed operations and continuously monitored in-coming data. Besides the NI data acquisition system, the legacy laptop (Rocky) also recorded data during these experiments.

A variety of experiments were conducted: normal (array facing up on lectern), inverted (array facing down on lectern), heads removed in sequence, heads remounted in sequence, array vertical (on edge), and array horizontal (facing up). The normal spin rate was one revolution in 13 minutes. Some experiments were repeated at a slower spin rate (one revolution in 26 minutes) to accommodate the Rocky laptop's lower data rate (5 samples per second). Final spin calibration on Nov. 5 had the array on the lectern in normal and inverted aspects. These data are used for all subsequent data corrections because the heads remained fixed afterwards without further adjustments.

5.3.2 Data Reduction and Analysis

Our efforts have concentrated on deriving calibration coefficients from the spin calibration data which can achieve 1.0 nanotesla precision of the magnetic vector gradients G_{xx} , G_{xy} , G_{yx} , G_{yy} , G_{zx} , G_{zy} , and G_{zz} in a common frame of reference. These vector gradients are computed by differencing diametrically opposite vector components (e.g., head 1-Y minus head 3-Y) across the planar cross-array baseline (nominally 0.37 meter). To realize 1.0 nT precision it is necessary to accurately determine the following parameters:

1. Transfer function for each of the 12 axes (volts-to-nanotesla), to third order
The transfer functions have the form:

$$B = Av^3 + Bv^2 + Cv + D$$

where: B is magnetic field, v is voltage, and A-D are the coefficient parameters

2. Inorthogonalities between three axes of each head, to first order
The inorthogonalities have the form:

alpha, beta, gamma

where: The X-axis is fixed, alpha is angle between the X and Y axes, and gamma is the angle between the X and Z axes.

3. Alignment (Euler rotation) angles to rotate heads 2, 3, and 4 into the head 1 frame of reference, to first order.
The Euler angles have the form:

delta, epsilon, zeta

where: delta is the first rotation about the Z-axis, epsilon is the second rotation about the Y-axis, and zeta is the third rotation about the Z-axis.

Unlike the legacy system, which receives bin numbers in serial data from the MIU, the NI digitizes the bin volts directly. To convert bin volts to bin number, it was necessary to perform a linear regression of laptop bin numbers against NI voltages. This procedure was needed only once to establish an accurate transfer function relating volts to bins.

We are using a multiple nonlinear regression program (NLREG) to match the spin calibration data (over 12,000 quality-checked measurements) to the base station-corrected ambient magnetic field. The regression dataset included measurements from both normal and inverted spins (Figure 5.9). The NLREG program for the planar array is modified from the one used for the tetrahedral array data obtained in 2003, with the main difference in the formulations for the inorthogonality and alignment angles. The best results to date are given in Table 5.1. It is then a straightforward procedure to apply the calibration coefficients to the raw field data and to derive the magnetic gradient tensor. As a test of the accuracy, the coefficients are applied to the spin calibration data. If the regression were exact, then no differences would be observed between the corresponding vector components (e.g., all the X-, Y-, and Z-components would be equal, respectively). As Figure 5.10 shows, the desired degree of accuracy has not yet been achieved. The bottom half of the figure shows the X-component of head 1, while the top half shows the

Gxx gradient, which is the difference between head 1 X-component and head 3 X-component. An angularly dependent residual of ± 1 nT remains in Gxx, when a sub-nanotesla residual was expected. A similar variation is observed for the other directional gradients. Several possible causes for this variation are posited:

1. Static magnetic field gradients in the volumetric space of the spin calibrations,
2. Geomagnetic field temporal variations of the Earth's total field,
3. Geomagnetic field temporal variations of the Earth's vector field components,
4. Thermally dependent variations, and
5. Small sensor interactions not yet understood.

Of these, the most serious (number 5) is considered least likely, because at the 2 nT/m level, these would have been detected in the sensor proximity/interaction experiments conducted in 2004 and 2005. The data from those experiments were the basis for the 0.367 m baseline separation of the sensors on the planar array. Thermal effects (number 4) are a possibility, and to investigate this the regression equations are being modified to use the temperature measurements. Fluctuations in the Earth's magnetic field components (inclination, declination) could introduce vector component variations as the array was rotated, but considering that the reference basestation recorded less than 1 nT of diurnal change during the average duration of a complete spin, this candidate (number 3) seems unlikely. If other means fail to account for the variation, however, this possibility will be reconsidered. Possibility number 2 has been discounted, because the results from assuming a constant ambient field compared with the results using a diurnally corrected magnetic field do not differ significantly. The last possibility (number 1) is considered the most likely. The low magnetic gradient location was identified through a high-resolution G-858 survey with the sensors in vertical gradient configuration. As this was the only G-858 available, there was no accompanying reference basestation data to correct for diurnal variations. Therefore, it's possible that these G-858 data are in error approximately on order of the observed residuals. To investigate this, the regression equations are being modified to incorporate a non-uniform ambient field in the spin volume. We suspect this will account for most, if not all, of the observed systematic error.

5.4 Calibration Grid Surveys

5.4.1 Field Procedures and Data Acquisition

The objective of the towed surveys over the Calibration Grid was to obtain baseline data to test target location and discrimination algorithms that are currently under development.

Two complete surveys were performed, one on Nov. 8 and the second on Nov. 15. Both were run in racetrack mode, in which the tractor was driven from south to north on the western half, and north to south on the eastern half, with turnarounds at the northern and southern boundaries. Survey on Nov. 8 covered the entire grid at 0.5 m line spacing. During this survey, the data acquisition system ran continuously. When the data files reached a certain size (about 100 MB), they were closed and new files were automatically created with incremental file names. The survey on Nov. 15 covered the entire grid at 1.0

m line spacing with the platform guided down the center of the lanes. Because of extraordinarily high winds, guiding the platform proved extremely difficult, as it tended to crab from side to side under the force of gusting winds (Figure 5.11).

5.4.2 Data Reduction and Analysis

Coverage maps for the Nov. 8 and Nov. 15 surveys are given in Figure 5.12 and Figure 5.13, respectively. High gusting winds on Nov. 15 caused highly irregular coverage, because the platform tended to move from side to side under the influence of wind drag. This occurred in spite of attempts by the operator to compensate by steering the tractor off line. Nevertheless, coverage was excellent in the Nov. 8 dataset and good in the Nov. 15 dataset.

As a first check on sensor array data quality, total magnetic intensity (TMI) equivalents were calculated from the vector components of each head using the latest, though rough, calibration coefficients. The TMI equivalent is simply the magnitude of the vector resultant of the three axial components. For these examples, the dataset of Nov. 8 is used. The TMI's for head 1, head 2, head 3, and head 4 are given in Figure 5.14, Figure 5.15, Figure 5.16, and Figure 5.17, respectively. Because the data are minimally processed, the images contain many artifacts that will be eliminated after more refined processing. The main point is to evaluate the images for signal consistency and overall coherence of detected anomalies.

Using current calibration coefficients, we can nevertheless generate Calibration Grid tensor invariant maps (invariants I1, I2, and tensor magnitude) to illustrate the functioning of the TMGS as a true tensor device. The array was towed over the grid at an average height of 0.3 m, so most of the measured magnetic gradients greatly exceed the current 2 nT/m limitation. The tensor invariant maps have been despiked and corrected for GPS lag, and system timing latency errors. The data are still minimally processed – no attempt has been made to compensate for the effects of roll, pitch, and temperature variations.

The first tensor invariant, I1, is defined as:

$$I1 = GXX*GYY + GYY*GZZ + GZZ*GXX - GXY*GXY - GZY*GZY - GZX*GZX.$$

The second tensor invariant, I2, is the determinant of the tensor matrix, defined as:

$$I2 = GXX*(GYY*GZZ-GZY*GZY) + GXY*(GZY*GZX-GXY*GZZ) + GZX*(GXY*GZY-GZX*GYY).$$

The third tensor representation, the tensor magnitude, is a variation of the I2 invariant and is defined as:

$$Tmag = \text{SQRT}(GXX*GXX + GYY*GYY + GZZ*GZZ).$$

Figure 5.18 shows the I1 map. The regular highs along the periphery are due to the steel balls used for lane markers. Clearly visible are numerous anomalies, ranging from large to small. The color gradation from left to right in both halves of the calibration grid is

probably due to thermal drift, which has not been removed. Small white circles mark the location of emplaced targets.

Figure 5.19 shows the I2 map. The determinant has a higher fall-off rate than the I1 invariant. This causes a sharpening of anomalies and suppression of long wavelength gradients. Small white circles mark the location of emplaced targets.

Figure 5.20 shows the tensor magnitude map. While anomalies are broadened in the direction perpendicular to travel, the image is clear of the along-line striations evident in the I2 map. Small white circles mark the location of emplaced targets.

Finally, some idea of the resolution of the tensor maps can be gained from inspection of the area of the calibration grid which contains many of the small, hard to detect targets. An enlargement of the northeast corner is shown in Figure 5.21. With these unrefined tensor maps it is possible to discern BLU-26 items (column 13, rows H-M). Tensor maps such as these were unobtainable with the original tetrahedral system on a towed platform.

5.5 Cued Surveys

5.5.1 Field Procedures and Data Acquisition

Grids measuring 3 m by 3 m were centered on selected 20 mm, 60 mm, and 81 mm targets. Using taut rope, measurement stations were established at 0.25 m intervals. With the platform unhitched from the tractor, the array was positioned manually over each station and data were recorded continuously for 30 seconds before repositioning the array over the next station. This resulted in over 3,000 magnetometer measurements and over 600 GPS positions at each station. Complete surveys were performed on the 81 mm target on Nov. 9 and on the 60 mm target on Nov. 14. The schedule called for the 20 mm target to be surveyed on Nov. 15, but poor site conditions forced us to abandon the cued survey in favor of a very high density towed survey, in which the tractor pulled the platform extremely slowly over the target on lines spaced 0.25 m apart. This experiment was not a success, however, as the data acquisition failed due to blowing dust and buildup of static electricity.

5.5.2 Data Reduction and Analysis

Coverage on both the 81 mm and 60 mm targets was excellent, as can be seen in Figure 5.22, and Figure 5.23. Data reduction and analysis of the magnetic gradient tensors for these experiments will be done after we have a final set of refined calibration coefficients.

5.6 Lag Line Surveys

The purpose of lag line surveys is to directly measure positioning errors caused by both the spatial offset of the GPS antenna to the center of the sensor array, and timing differences between the GPS updates and the data recording software. The first kind of error is independent of velocity, and should closely agree with measurements of the physical dimensions of the platform. The second kind of error is more subtle and

pernicious. It can be caused by buffering lags, system timing delays, and interruptions from operating system functions.

5.6.1 Field Procedures and Data Acquisition

A 30 m long calibration lane was established on the gravel road just to the west of the Calibration Grid. The lane was marked with a taut rope staked to the ground at each end with steel pegs. A steel sphere was placed in a shallow hole at the middle and covered with sand. This was later replaced by a strong bar magnet to increase the signal to noise of the data. Two experiments were performed over the steel sphere, and one over the permanent magnet. The paths over the target are shown in Figure 5.24, and Figure 5.25.

5.6.2 Data Reduction and Analysis

As the map in Figure 5.26 shown, a serious problem was revealed. Magnetic anomalies due to the magnet at the intersection of the lag lines do not coincide at the center, as expected. A lag of seven to eight seconds was evident. For the slow lines, the target registered about 7 seconds before the GPS position was over the target. For the fast lines, there was an 8 second discrepancy. Apparently, the time channel in the analog dataset was leading the time channel in the GPS dataset by a significant amount. As it happened, a flaw in the data acquisition software prevented the NI clock from being synchronized with the GPS clock as it was designed to do.

The GPS receiver and the NI system operate asynchronously. The GPS system relies on a satellite time-base, while the NI system derives its clock from a crystal controlled oscillator on the main board. If GPS time is taken as a standard reference, then the NI clock appears to drift over time. The NI specification is 50 microseconds per second, or 50 ppm. Over the short term, the effect will be unnoticeable, but over the course of several hours, the discrepancy can amount to several hundred milliseconds. In fact, at this rate positioning “slips” about every 20 minutes of data acquisition time. Synchronizing the two systems is nontrivial. The computer clock was set on the laptop-based legacy system by calling out the time indicated on an independent atomically-controlled watch. This method was adequate for the legacy system, because it acquired GPS positions every second and recorded sensor data every 0.2 second. The NI-based system, however, records GPS positions every 0.05 second and sensor data every 0.001 second. An engineering solution would be to incorporate an IRIG-B decoder into the NI chassis, but unfortunately NI does not yet have available a card that is compatible with the digitizer cards currently installed. Because the NI system remains on-site, there is no way to synchronize it to an atomic time server over the internet. The LabVIEW software was designed to set the NI system clock using the ZDA time string from the Leica GPS. Once this is done, the recorded PPS signals can be used to establish an accurate timing signal in the dataset. The software routine did not work, and the NI clock never got set. Consequently, rather than relying on the PPS channel for correlating times to GPS positions, lag corrections for the Nov. datasets have to be done manually in post-processing. This software flaw has been corrected and tested, and further shakedown tests will confirm the robustness of the fix.

5.7 Other Current Work

We will continue refining the spin calibration regression coefficients to the point where the field data can be reprocessed to a higher degree of accuracy. This step is necessary to process the cued high-density grid data over the 20 mm, 60 mm, and 81 mm targets, as well as to evaluate performance of the towed survey over the Calibration Grid, with particular attention to small targets, such as the 20 mm and 40 mm items. We received tensor gradient inversion software on March 21, 2006 from our collaborators at the Colorado School of Mines. We will test this software on field data at the earliest opportunity.

Experiments have been performed at the Denver Federal Center to evaluate the accuracy of the Leica GPS operating in differential RTK mode. A magnetic reed switch was placed on a benchmark in an open, paved area of a parking lot. The geodetic position is known to ± 2 mm. The GPS receiver antenna is mounted on a short mast that is attached to a low wagon. A permanent magnet is affixed to the bottom of the mast directly below the antenna. The mobile assembly is pictured in Figure 5.27. The reed switch is normally open, but when the magnet is 5 mm or less from the switch, it closes a simple resistor circuit. The signal from this circuit is digitized by the NI system at a rate of 100 KHz, along with the PPS pulse and ZDA serial data from the Leica. The map in Figure 5.28 shows the GPS positions (blue) along the lag lines. Positions where the reed switch was triggered are shown in red. An inset box shows the data at a 10 cm scale. The switch closures are indicated as red circles, and the precision benchmark is shown as a green cross. Note that most of the red positions are offset from the benchmark. The red positions appear in two separate clusters, one cluster containing EW-moving data and the other NS-moving data. Thus, there appears to be a systematic, directionally dependent shift in accuracy. These data were analyzed statistically (Figure 5.29). The error, as a function of radial distance away from the precision benchmark, appears normally distributed with a sigma of 0.04. In practice, then, we would expect a 4-cm uncertainty in GPS positions from a moving platform. More experiments are planned to further investigate this result.

Table 5.1: Head 1 regression coefficients

Param	H1X	H1Y	H1Z
A	-0.0409903529	0.0792098701	-0.010531755
B	0.00752839064	-0.0133833741	0.017100496
C	100.686659	101.527717	99.7345015
D	-0.191568112	-0.131091781	-0.209536344
alpha	90.0082988		
beta	90.8352916		
gamma	89.5133902		

Table 1B: Head 2 regression coefficients

Param	H2X	H2Y	H2Z
A	-0.0363224345	0.0387867193	-0.000171790317
B	0.00240221685	0.0000268946065	-0.0022677532
C	99.833256	101.439029	100.117349
D	-0.082684888	-0.00098596675	-0.0273581792
alpha	89.8407155		
beta	90.2404030		
gamma	89.7865905		
delta	-32.6120161		
epsilon	-0.511516137		
zeta	-58.0800960		

Table 1C: Head 3 regression coefficients

Param	H3X	H3Y	H3Z
A	-0.080776317	0.0825161945	-0.0141519253
B	0.00188970798	-0.00684747311	0.00594449427
C	100.086105	100.571804	100.196846
D	-0.0260332026	0.0194208643	-0.0239009621
alpha	89.7971474		
beta	91.3871882		
gamma	90.2605870		
delta	-288.3876270		
epsilon	-0.850204373		
zeta	108.5513520		

Table 1D: Head 4 regression coefficients

Param	H4X	H4Y	H4Z
A	0.0480909032	-0.0467378698	-0.0106305057
B	0.00291967932	0.0130304129	0.0102450299
C	100.281437	101.381862	99.8489213
D	0.0429226015	-0.00895568728	0.0398757028
alpha	90.1122809		
beta	89.4769338		
gamma	88.9605493		
delta	11.7578605		
epsilon	0.520310400		
zeta	77.9930662		

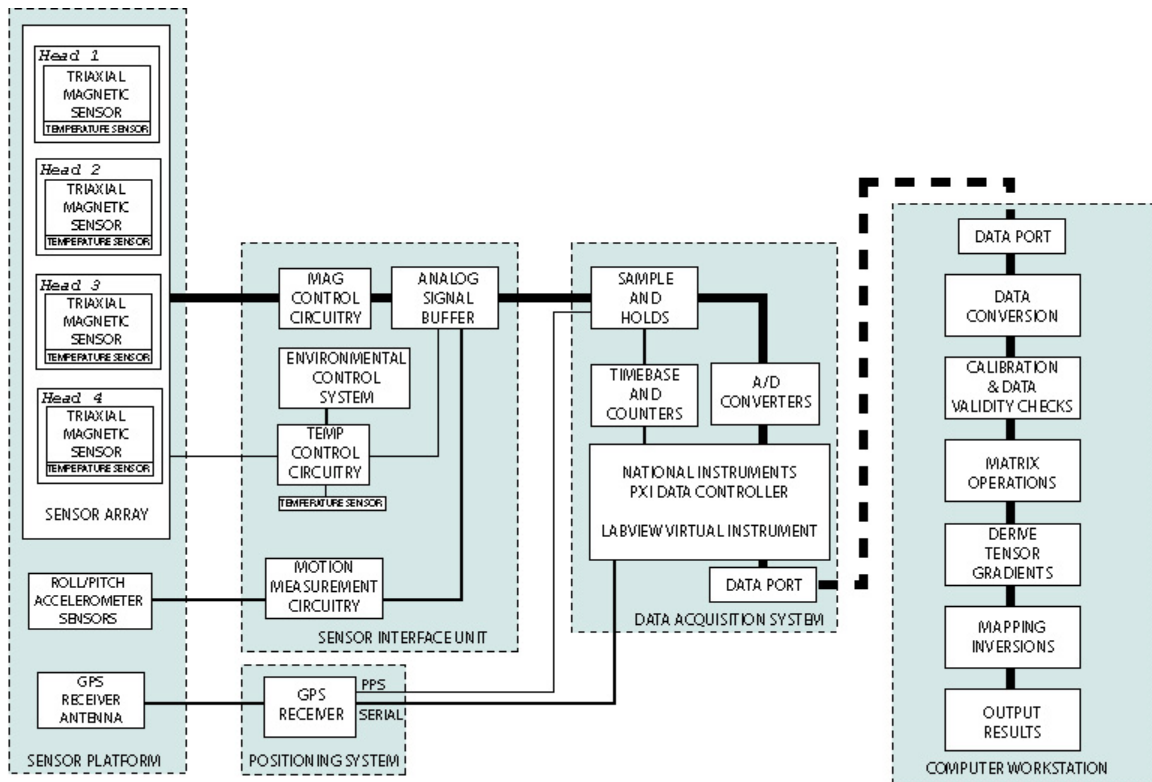


Figure 5.1. TMGS System Block Diagram showing the five major components (dashed, shaded boxes). Major and minor data paths are indicated by thick and thin lines, respectively. The computer workstation (on right) is independent of the other components, which operate together in real time. Data is transferred to the computer workstation using portable storage media, such as an external hard disk drive.

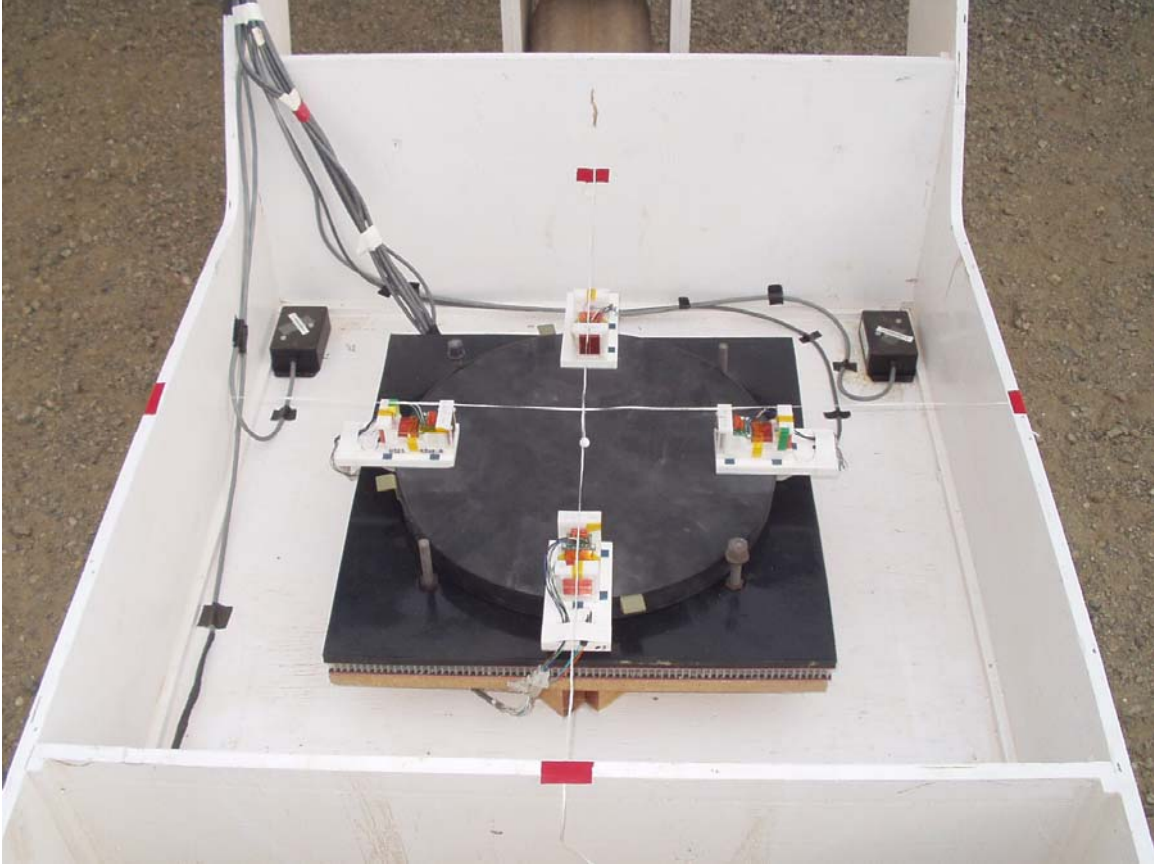


Figure 5.2. The magnetometer array mounted in the towed platform during alignment. The two accelerometers (black boxes) are mounted forward of the array. The inclinometer (not shown) is mounted in the right-rear corner. The GPS receiver antenna (not shown) is mounted above the front wheel pivot, approximately 2 m in front of the geometrical center of the array (indicated by white ball).

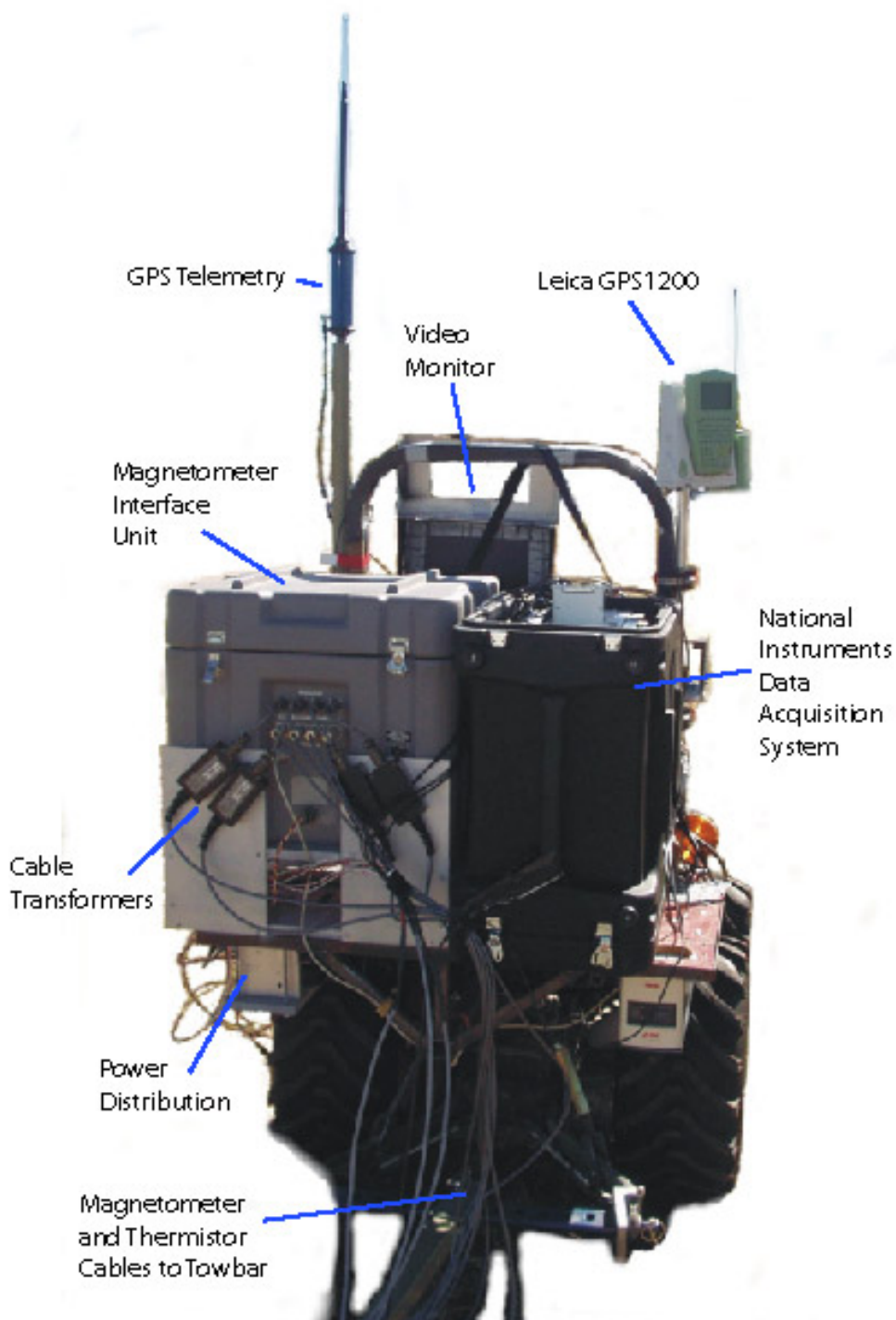


Figure 5.3. The TMGS electronics are shown mounted on the prime mover, a Kubota tractor. The Magnetometer Interface Unit (grey case on left) is the only original piece of equipment still being used. The computer controlled data acquisition system (black case on right) receives analog signals from the MIU and ancillary sensors, along with serial data from the GPS receiver mounted on a short mast. A keyboard, monitor, and mouse face the driver/operator. Not shown is a bank of four 12VDC lead acid batteries mounted on a shelf over the front bumper of the tractor.



Figure 5.4. The GPS base is erected over a pre-established geodetic marker.



Figure 5.5. The TMGS in operation over the Calibration Grid. The operator used a simple outrigger pointer to guide the tractor between large red disks that marked the corners of individual cells.



Figure 5.6. The spin calibration apparatus set up for a calibration run. The electric motor drive assembly (left) transmits power through a set of tandem pulleys (center) to the rotating platen on the turntable assembly (right). The magnetometer array is mounted on a lectern which rests on the platen. Here the array is seen shielded from direct sunlight in order to minimize large, rapid temperature variations.



Figure 5.7. The magnetometer array mounted on the lectern (brown material) at a 57 degree inclination. The clamping bar and stops around the perimeter of the array prevented it from shifting while the array was manipulated for various experiments.



Figure 5.8. The TMGS data acquisition system was stationed about 10 m away from the magnetometer array. The MIU (grey case on left) and the NI computer (black case) are flanked by lead acid batteries. The GPS receiver (top center, on the pole) supplied timing pulses.

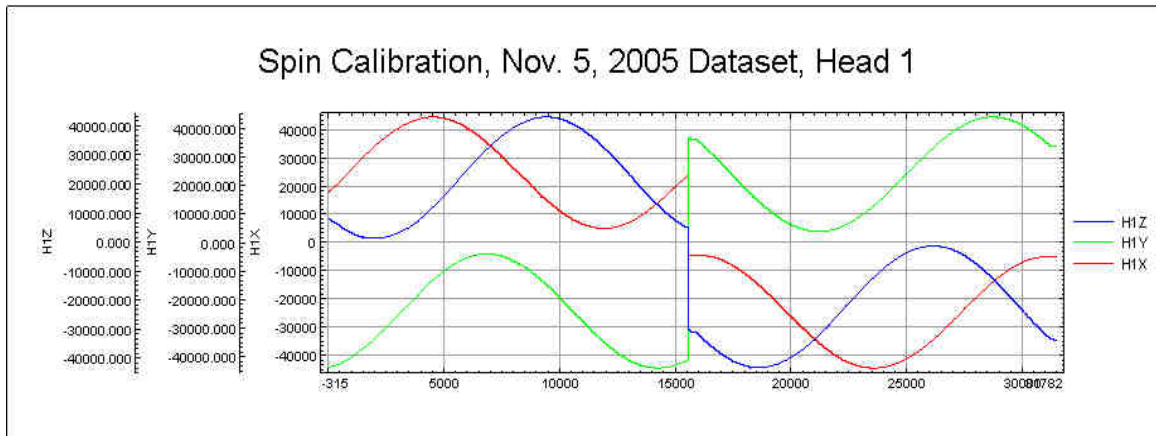


Figure 5.9. Example of raw spin calibration data from a single magnetometer head. Data in the left half of the plot (samples 0-16,000) come from a normally oriented array. Data in the right half of the plot (samples 16,000-33,000) come from an inverted array. Both types of data were used in order to characterize the magnetometer transfer functions across a broad range of positive and negative values.

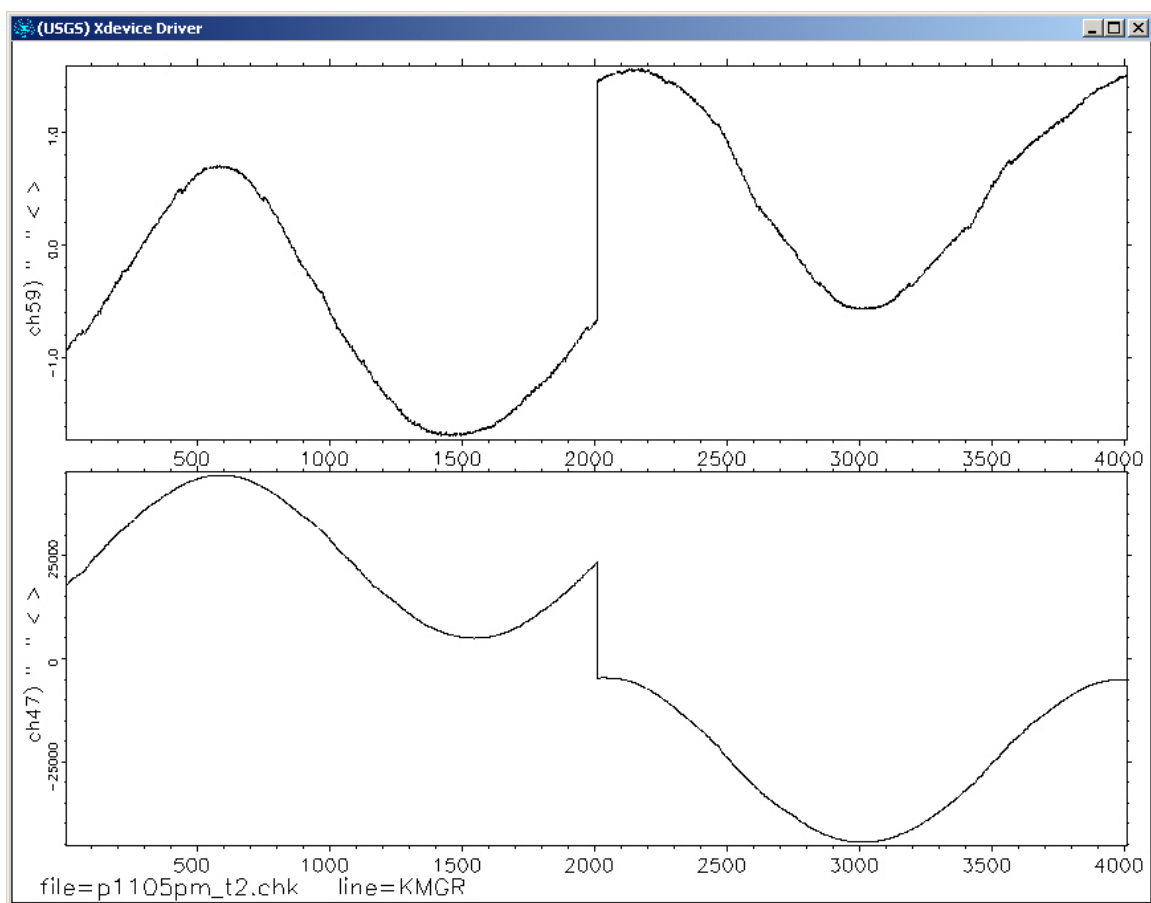


Figure 5.10. Example of the observed 2 nT residual after regression on the spin calibration data. Data from the X-axis of head 1(bottom frame) is compared to the Gxx gradient (top frame). Ideally Gxx, the difference between the head 1 X-component and the head 3 X-component, would be zero.



Figure 5.11. Severe winds forced us to scrub field operations on Nov. 15. The high-resolution survey over the 20 mm target continued, despite poor visibility and worsening conditions, until static build-up interfered with the NI electronics, causing persistent problems with the keyboard and video display. Sporadic electrical discharges threatened to damage the data acquisition system.

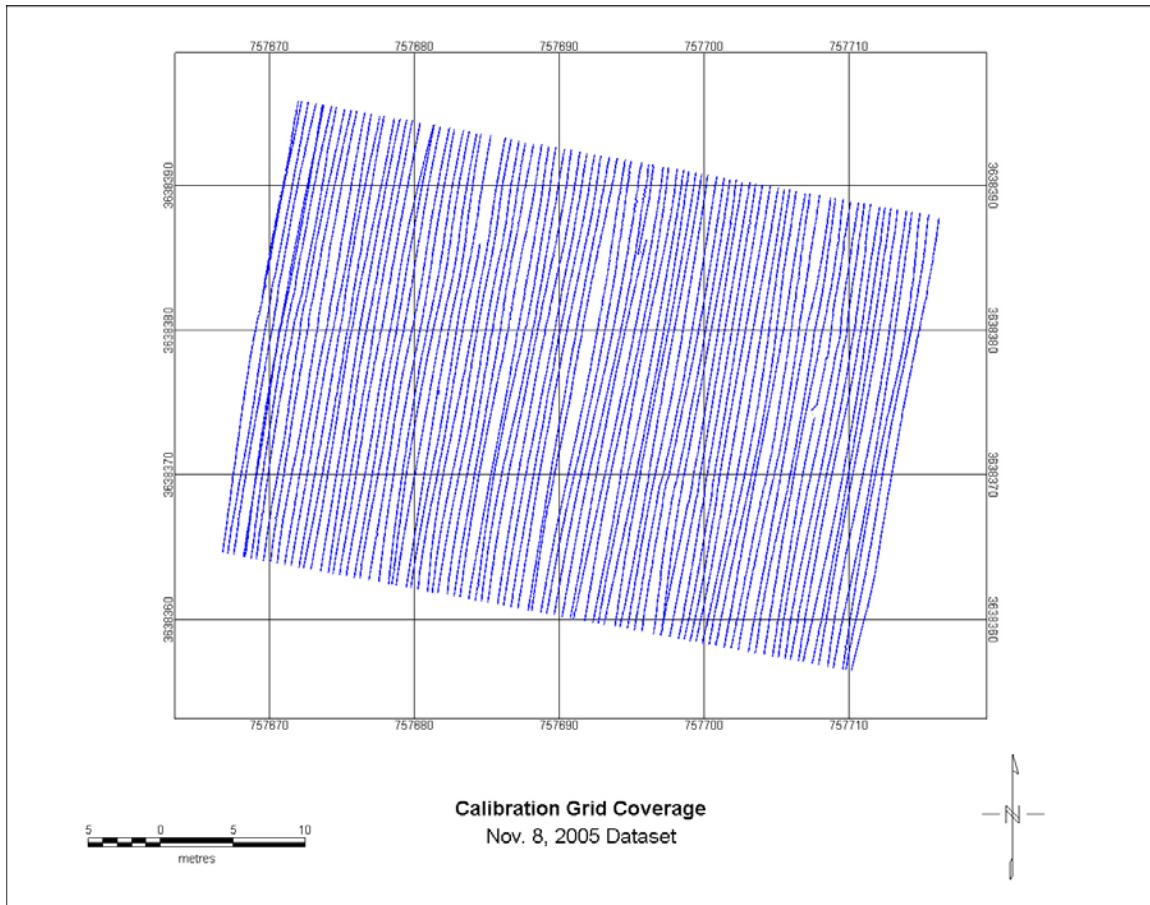


Figure 5.12_. The Calibration Grid was surveyed along lines spaced 0.5 m apart. The lines in the western half of the grid were taken in a south-to-north direction. The ones in the eastern half were taken in a north-to-south direction. A few lines are truncated because GPS fix quality changed from fix (acceptable) to float (unacceptable).

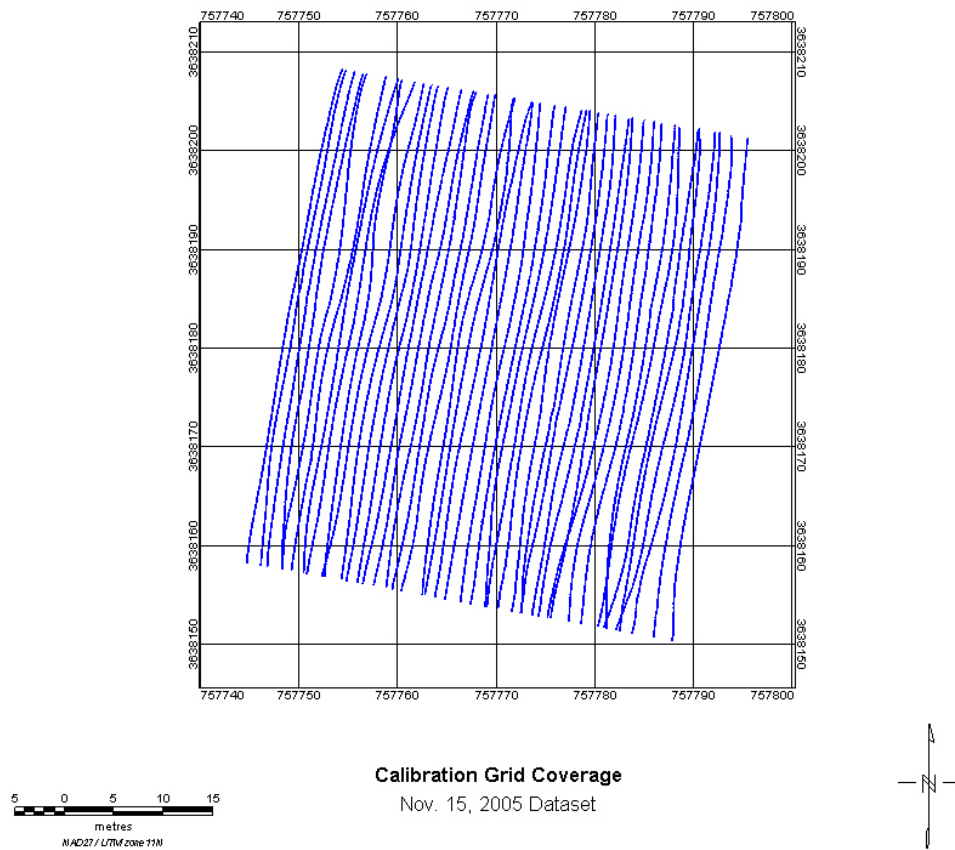


Figure 5.13. The Calibration Grid was re-surveyed along lines spaced 1.0 m apart. As with the Nov. 8 survey, the tractor was driven in racetrack mode: north-going lines are in the western half, south-going lines are in the eastern half. The coverage is more irregular than the previous survey because high winds caused the platform to crab along track.

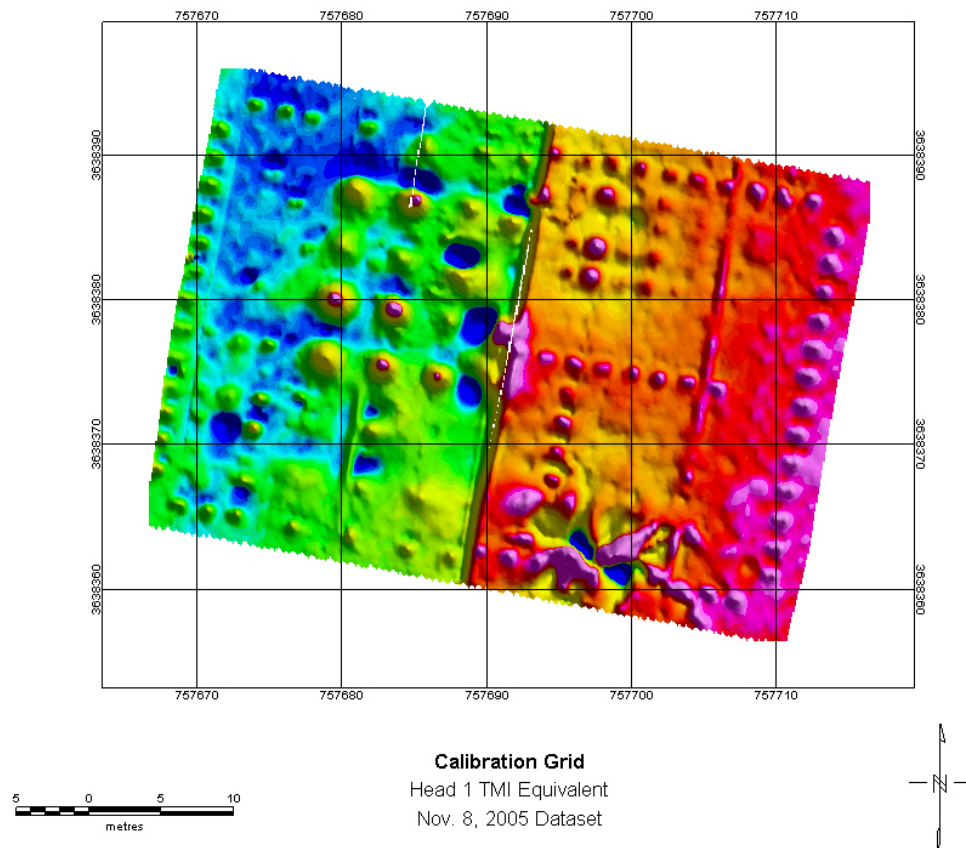


Figure 5.14. The equivalent total magnetic intensity as measured by Head 1. This image from raw field data displays both heading error (a directional amplitude shift) and a lag error (misalignment of marker anomalies). Both errors are removable in post-processing.

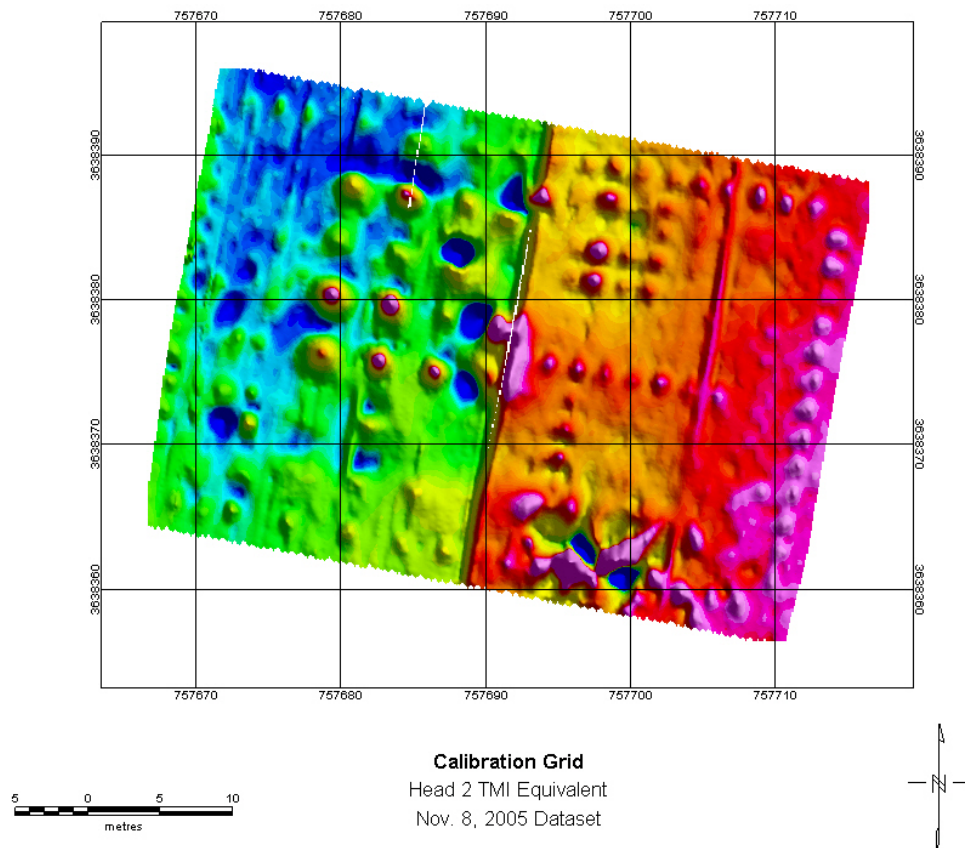


Figure 5.15. The equivalent total magnetic intensity as measured by Head 2. This image from raw field data displays a heading error (a directional amplitude shift). The lag error (misalignment of marker anomalies) has been corrected in this map.

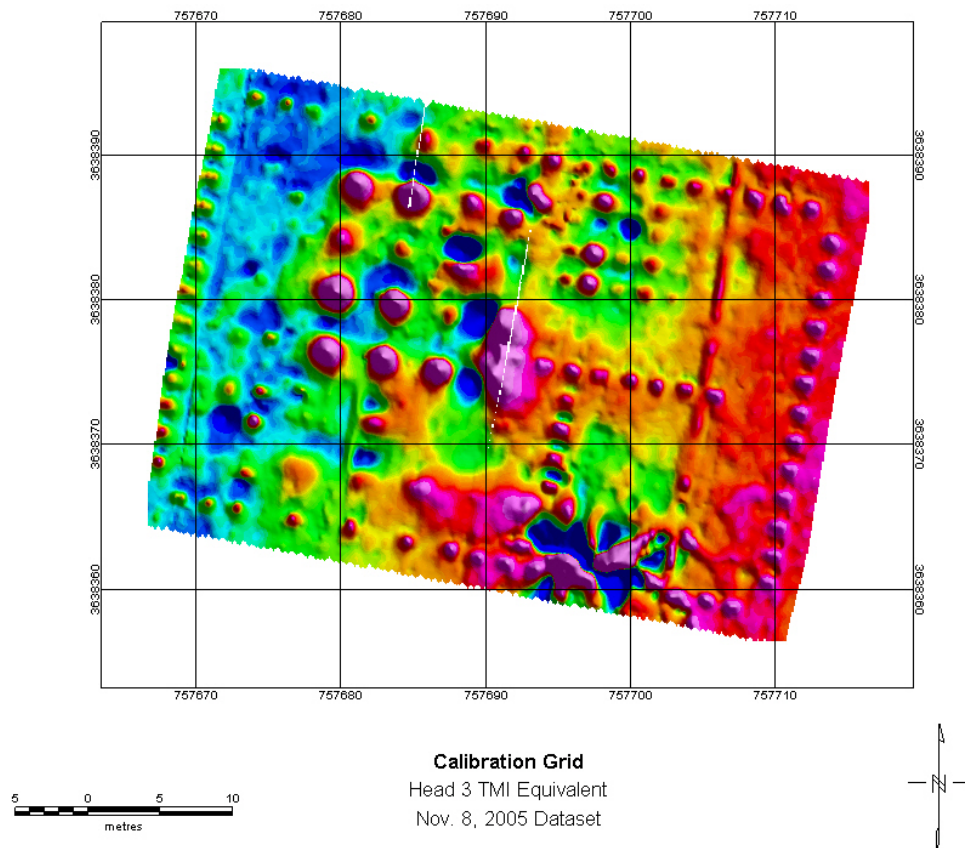


Figure 5.16. The equivalent total magnetic intensity as measured by Head 3. This image from raw field data displays a heading error (a directional amplitude shift). The lag error (misalignment of marker anomalies) has been corrected in this map.

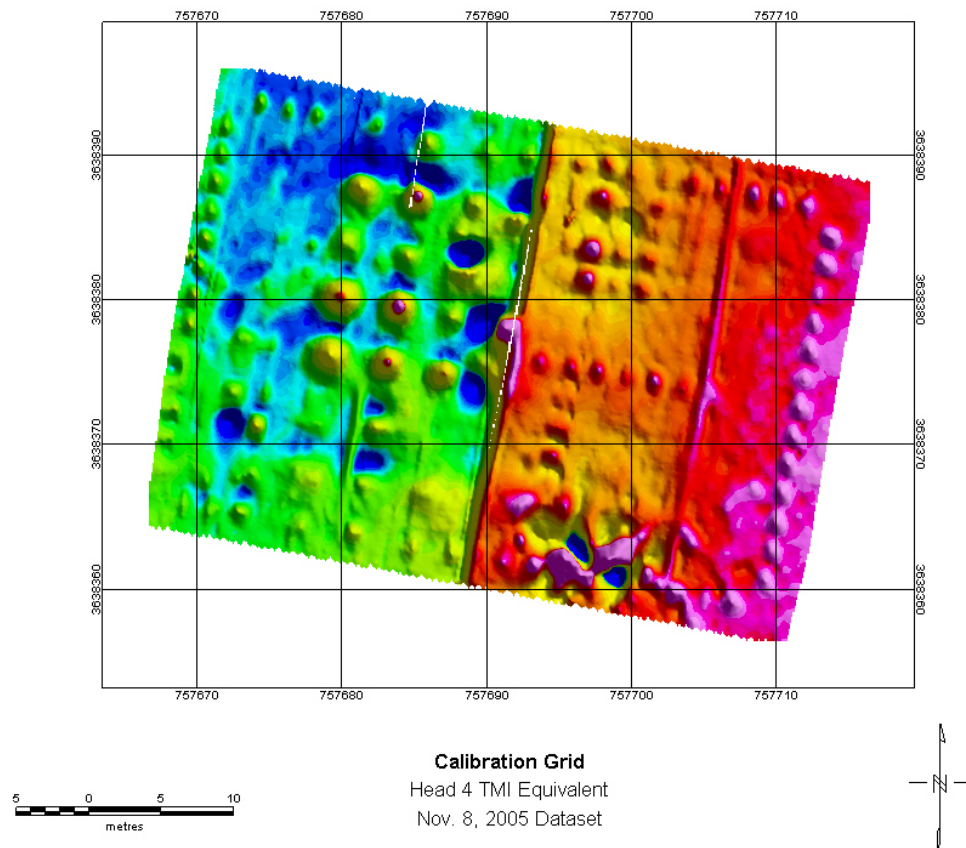


Figure 5.17. The equivalent total magnetic intensity as measured by Head 4. This image from raw field data displays a heading error (a directional amplitude shift). The lag error (misalignment of marker anomalies) has been corrected in this map.

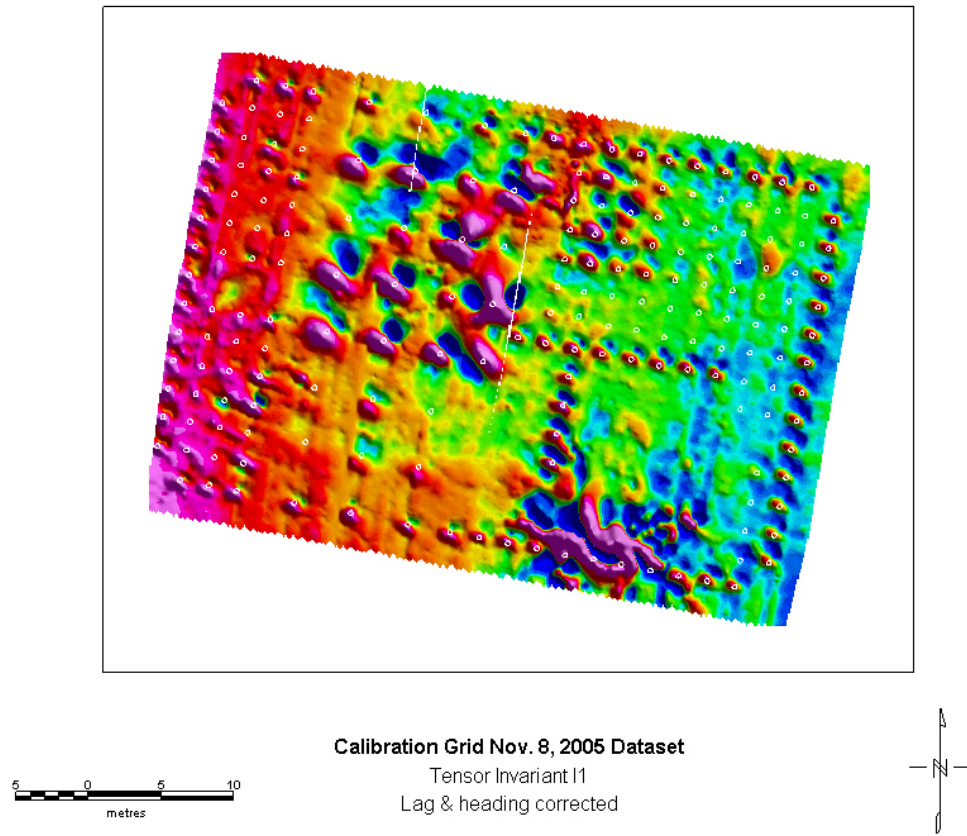


Figure 5.18_. Tensor I1 Invariant map of the Calibration Grid. The data have been lag corrected but not heading error corrected.

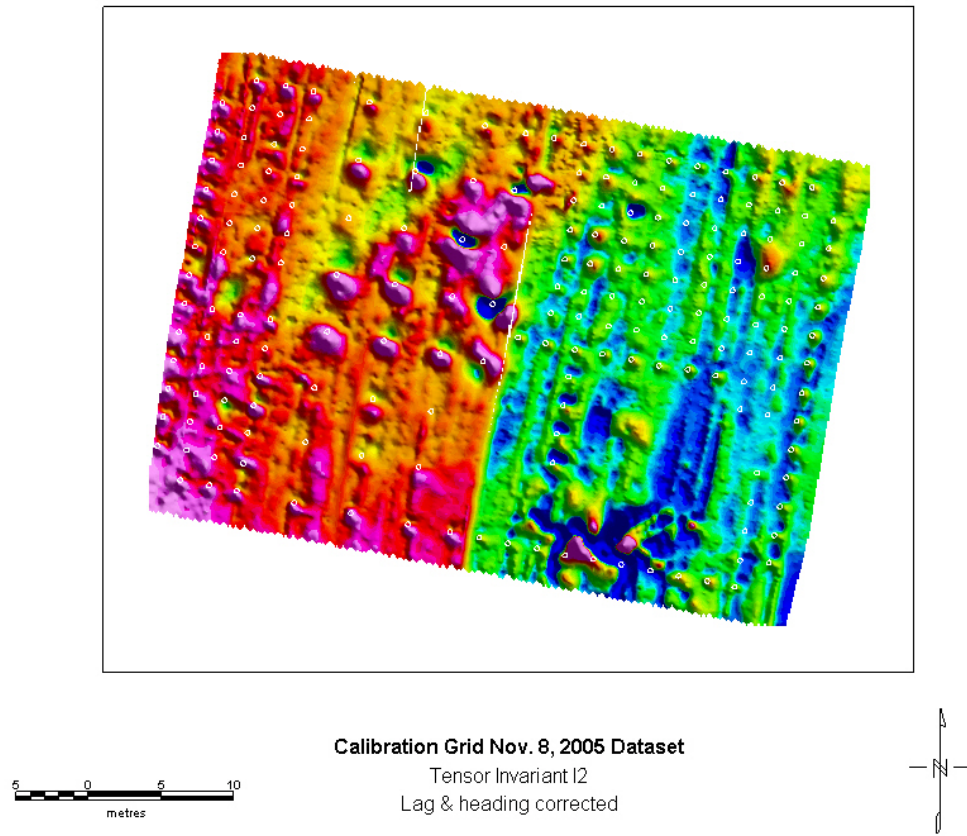


Figure 5.19. Tensor I2 Invariant map of the Calibration Grid. The data have been lag corrected but not heading error corrected.

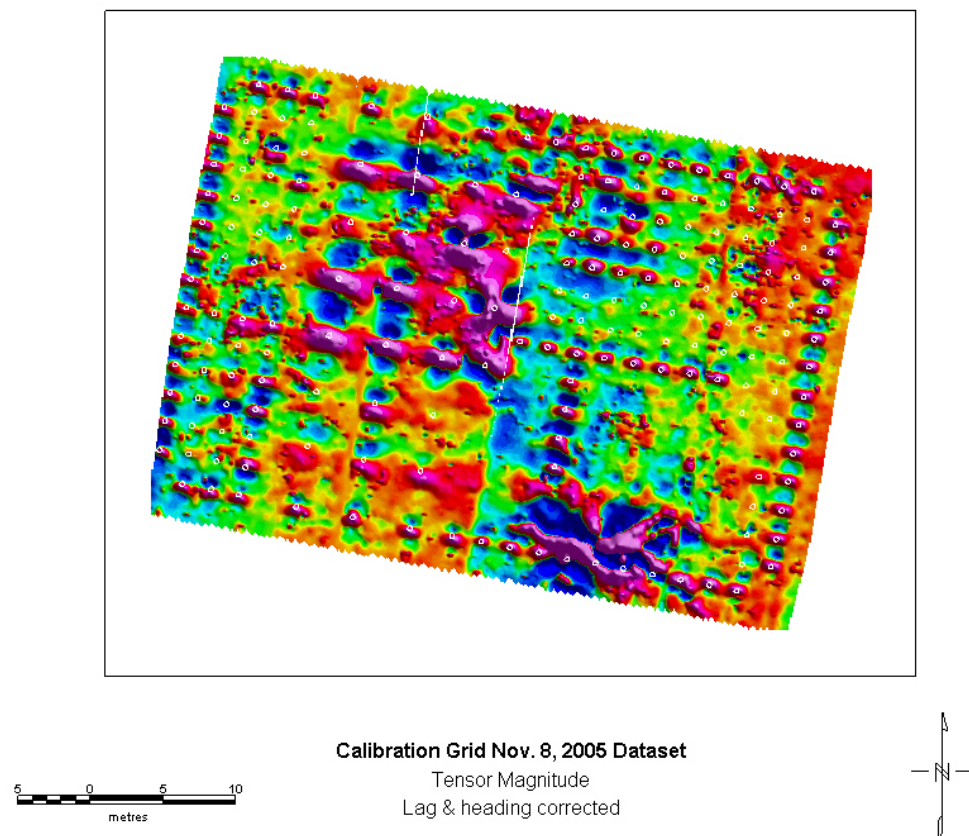


Figure 5.20. Tensor Magnitude map of the Calibration Grid. The data have been lag corrected but not heading error corrected.

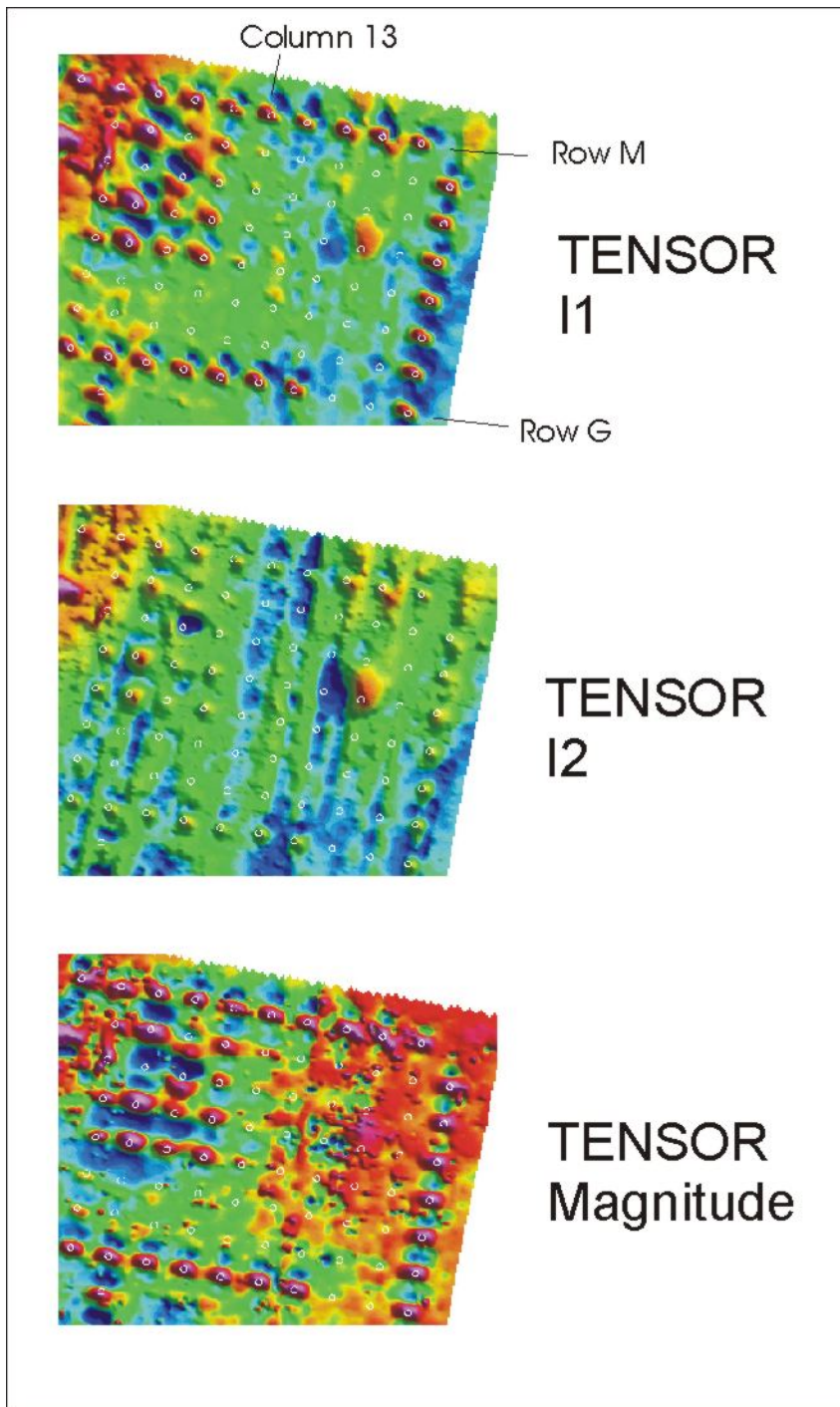


Figure 5.21. Tensor Invariant maps of the northeast corner of the Calibration Grid where many of the small targets are emplaced. Small white circles mark the location of targets.

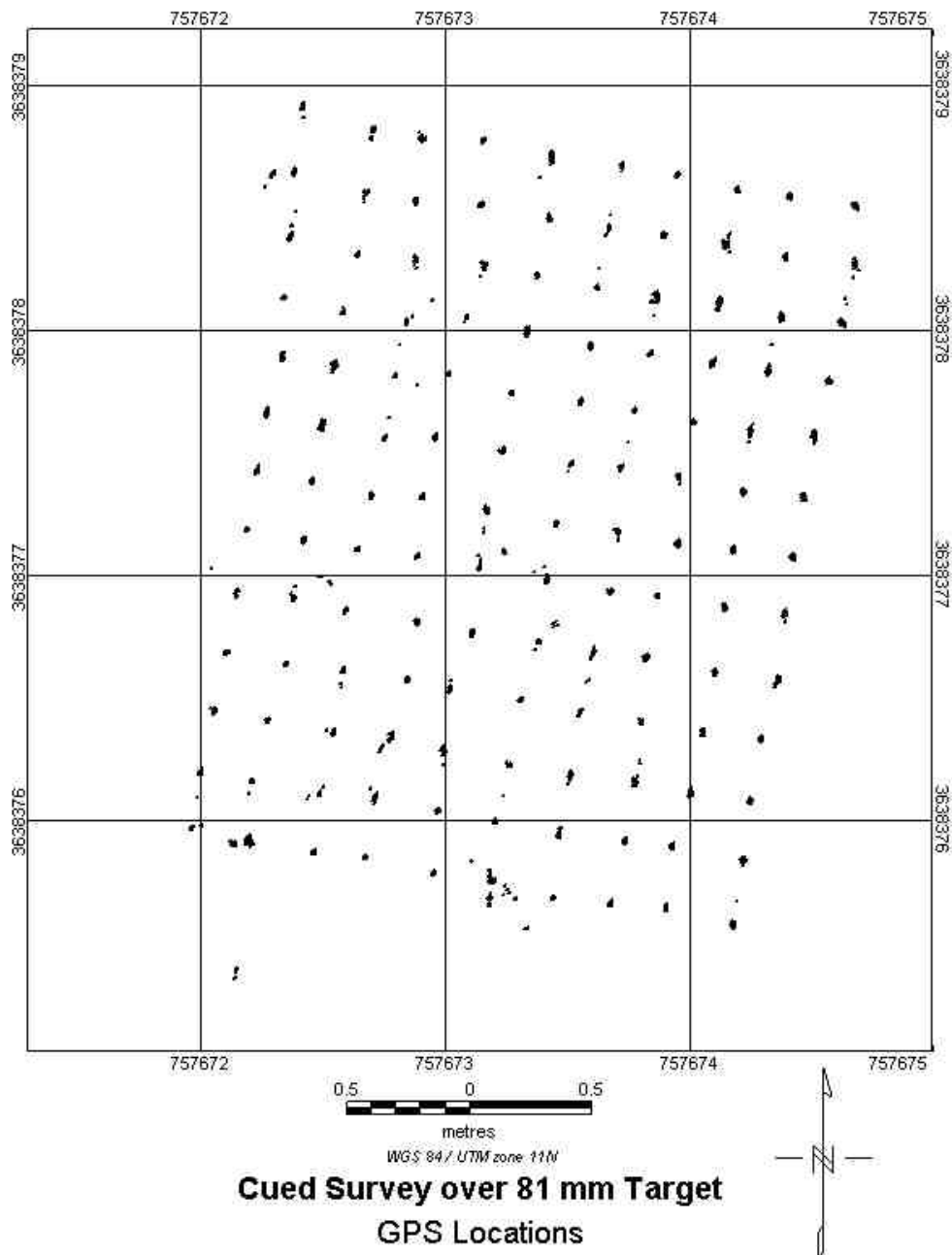


Figure 5.22. More than 600 GPS positions were recorded at each station. Positions which are 1 mm or less apart are plotted in this figure. Outliers not aligned with the main 13x10 grid are due to stagnant motion as the platform was reposition to a new station.

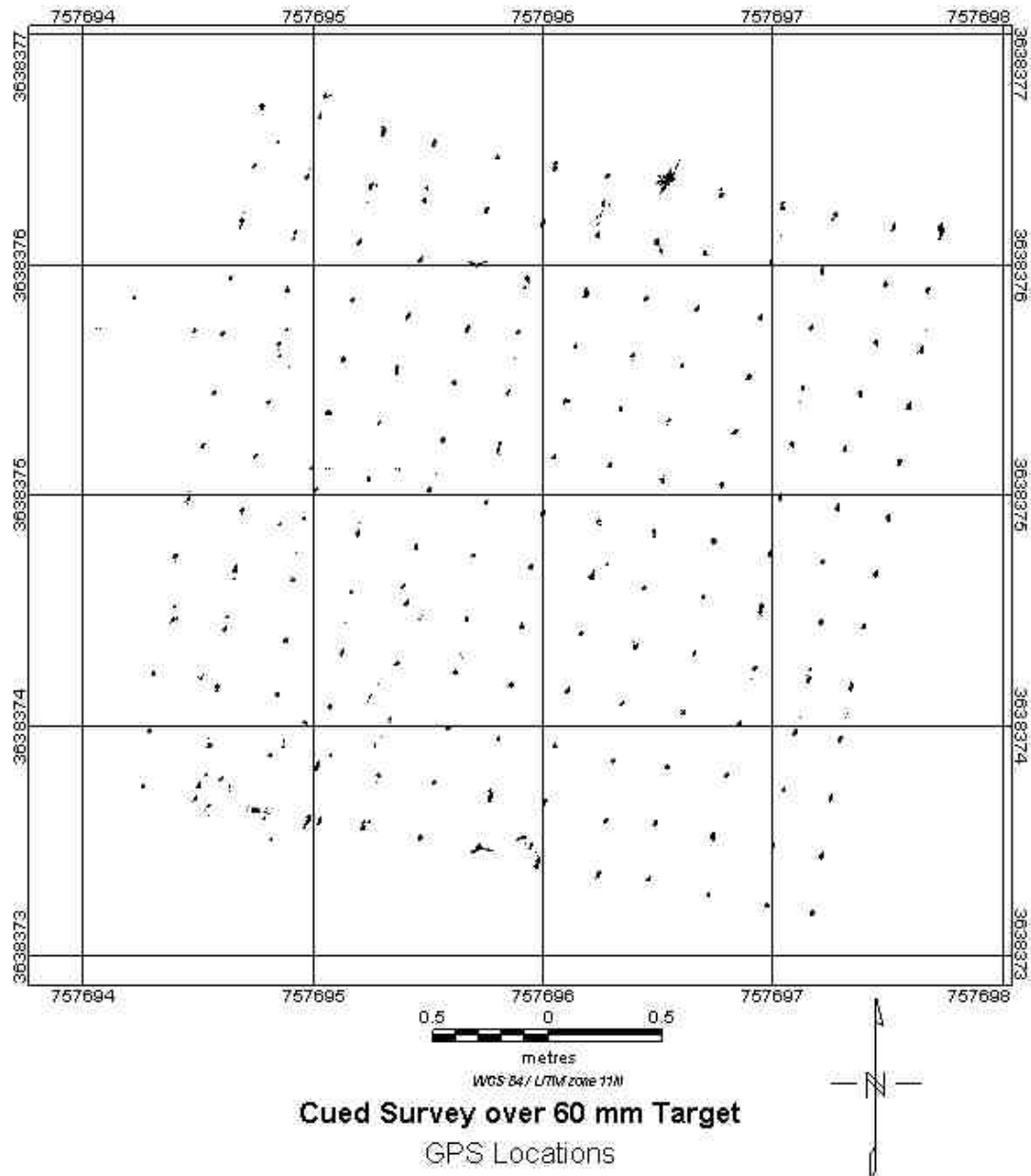
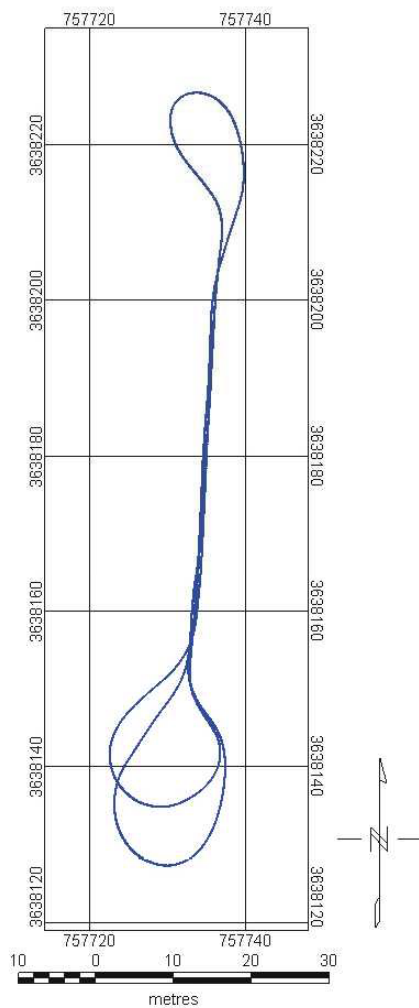
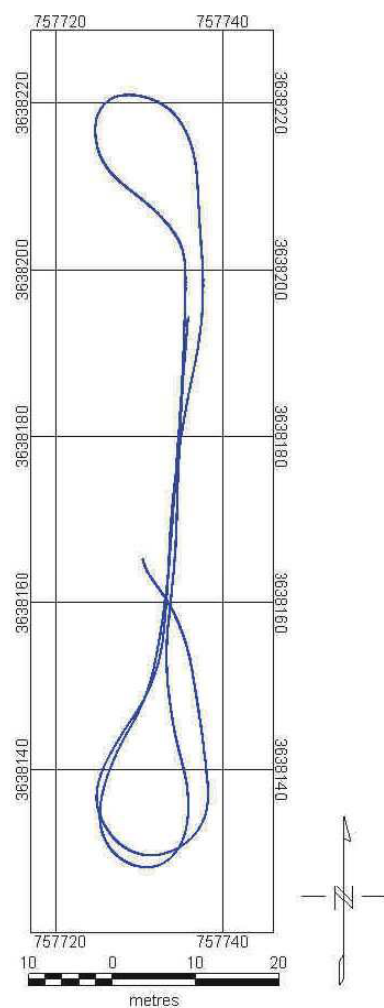


Figure 5.23. More than 600 GPS positions were recorded at each station. Positions which are 1 mm or less apart are plotted in this figure. Outliers not aligned with the main 13x13 grid are due to stagnant motion as the platform was repositioned to a new station.

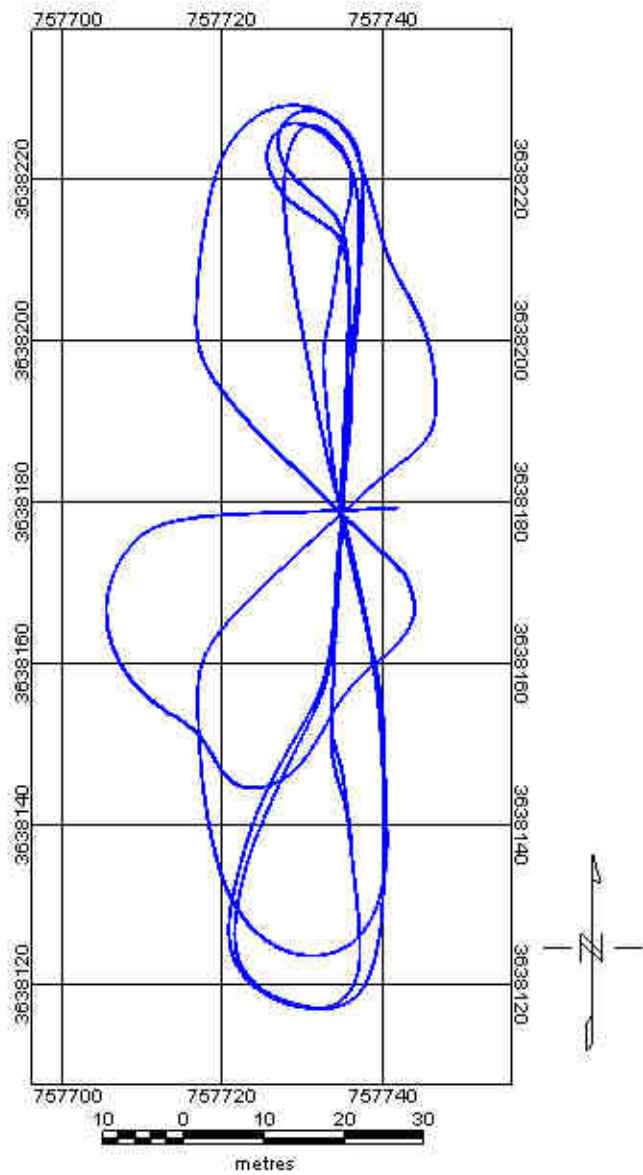


Lag Line Experiment
Nov. 7 Dataset



Lag Line Experiment
Nov. 9 Dataset

Figure 5.24. Lag line paths over a steel ball.

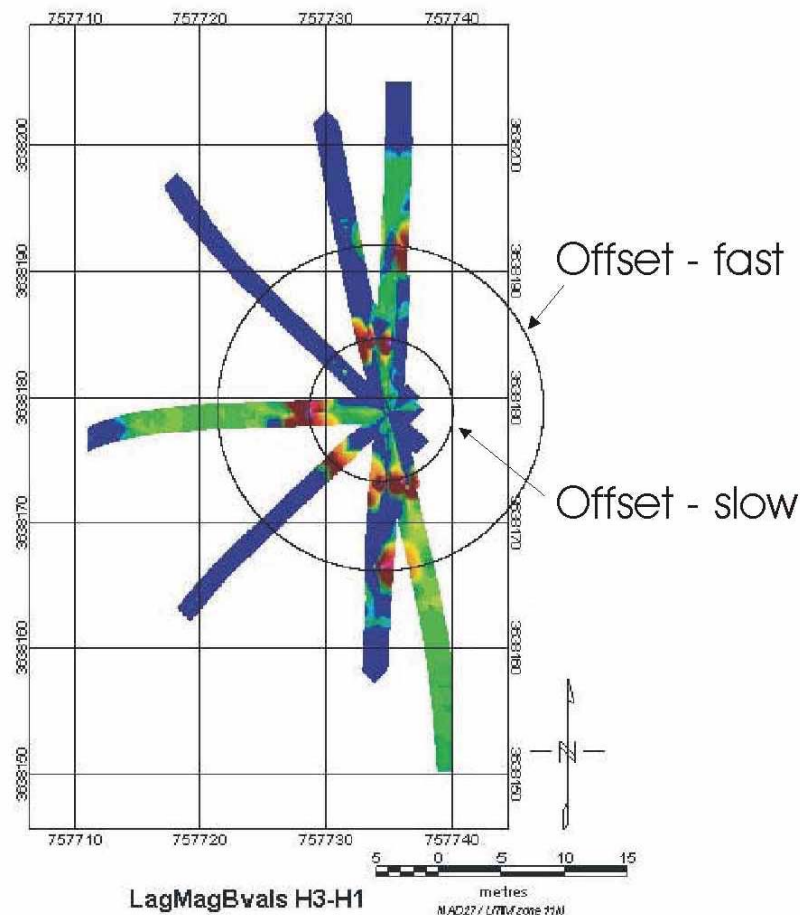


Calibration Rosette

Nov. 14, 2005 Dataset

Lag and Heading Error Experiment

Figure 5.25. Lag and heading error calibration rosette over a permanent (bar) magnet.



LagMagBvals H3-H1
Nov. 14 Dataset Slow and Fast Lines
baselines subtracted in Excel

UTM E (peak anomaly) (m)	UTM N (peak anomaly) (m)	DESC.	AVG VEL L (cm/s)	delT (m)	
757734.220	3638166.392	fast S-N	151.5	12.534	8.273
757735.372	3638191.888	fast N-S	157.5	12.988	8.246
757734.332	3638173.192	slow S-N	77.9	5.739	7.368
757734.906	3638184.262	slow N-S	72.8	5.350	7.354
757656.648	3638374.911	center (WGS84)			
-114:14:48.565310 E2:51:11.591860 Menter (Lon/Lat)					
757734.791	3638178.913	center (NAD27)			

Figure 5.26. Magnetic anomalies due to the magnet at the intersection of the lag lines do not coincide at the center, as expected. A timing delay causes an apparent spatial offset, the size of which is a function of the velocity of the platform.



Figure 5.27. Experimental set-up to measure system timing delays. A bar magnetic directly below the center of the GPS receiver antenna trip the reed switch at a proximity of 5 mm or less.

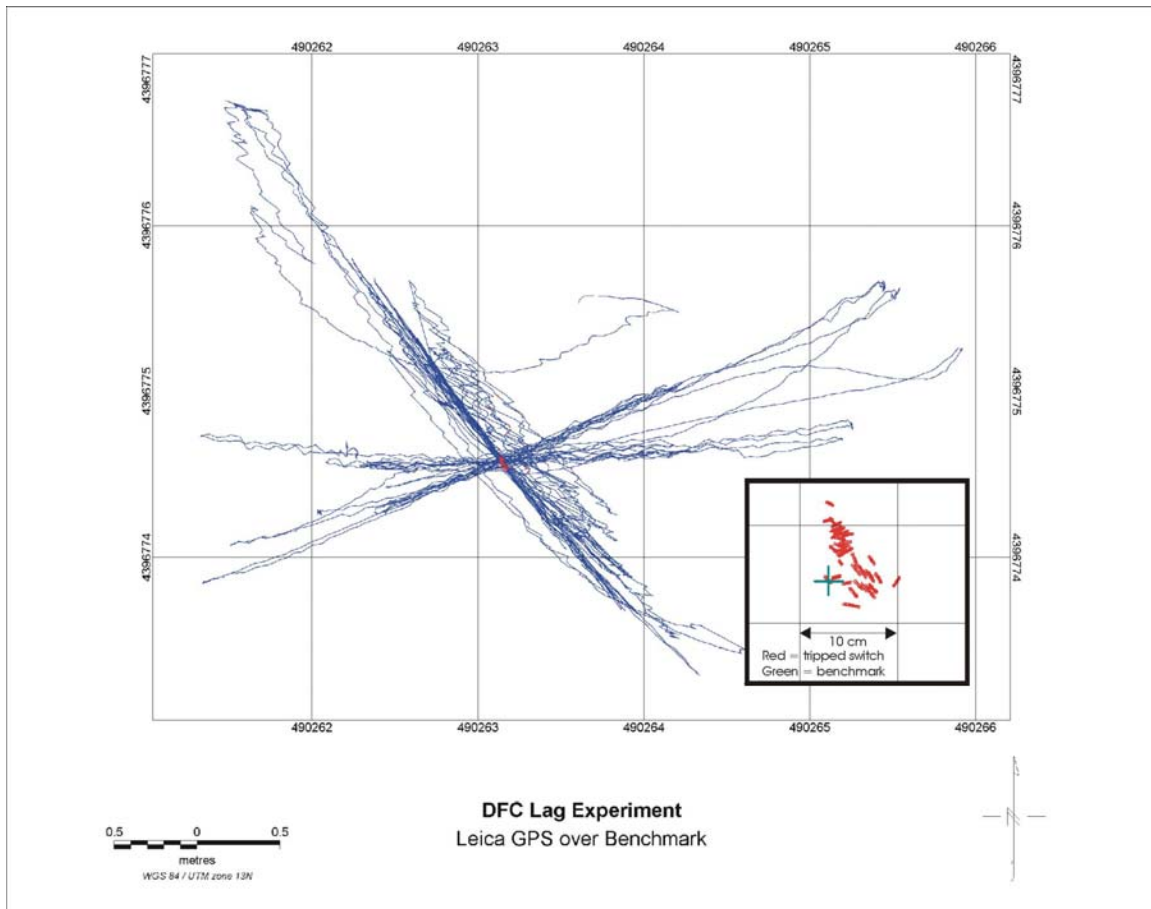
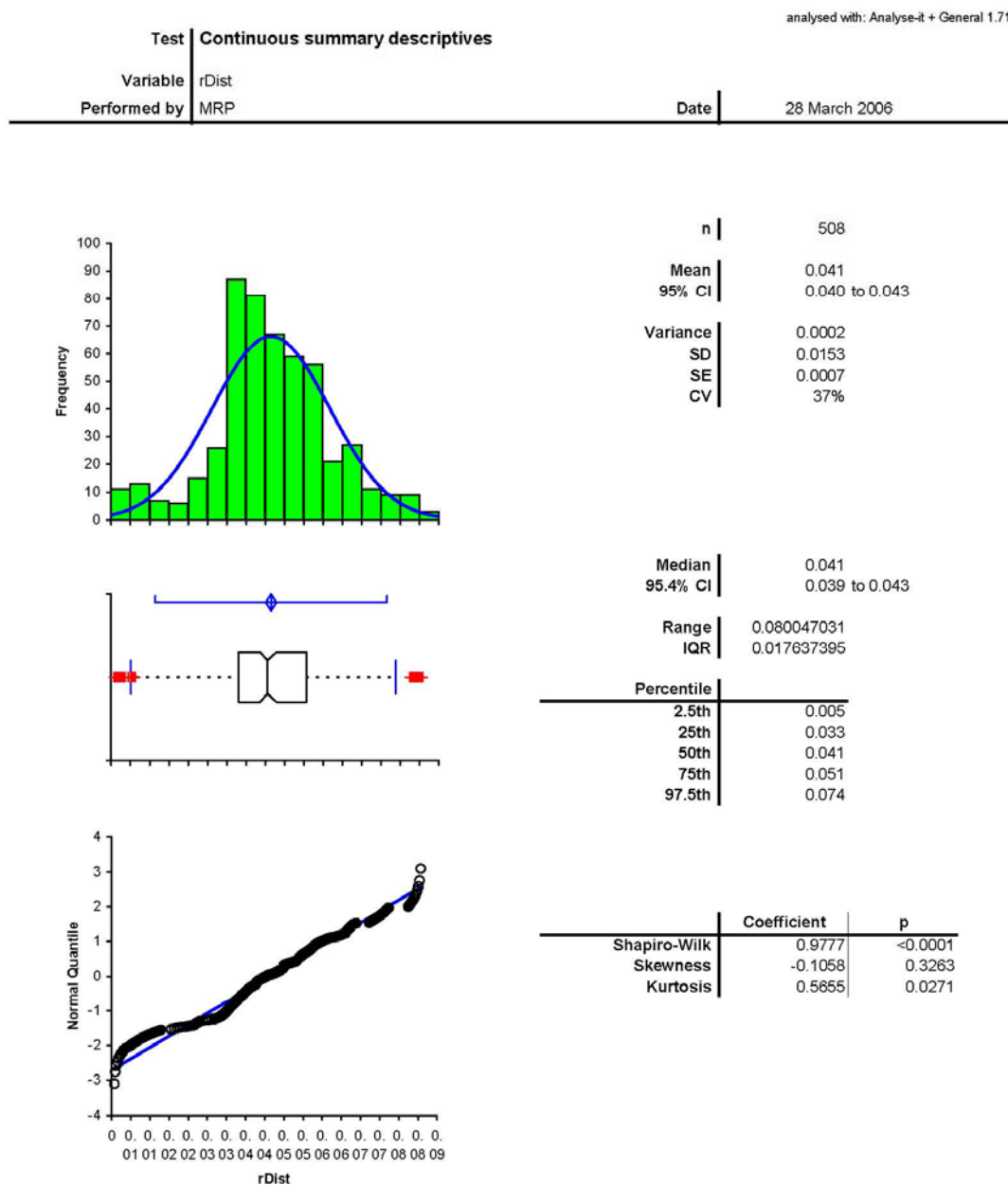


Figure 5.28. GPS positions along lag lines (blue) over a precise benchmark at the Denver Federal Center. The positions where the reed switch was triggered by the magnet under the GPS antenna are plotted as red circles. The inset slows these positions on a 10-cm grid.



Page 1 of 1

Figure 5.29. Summary statistics of the GPS positions when the reed switch was triggered.

6.0 MAGNETICS MODELING AND INVERSION

TMGS directly measures all independent components of the magnetic gradient tensor and, therefore, it rejects a number of common-mode noises, such as diurnal variation and position errors in individual data points. As a result, the data will be of higher quality than current total-field anomaly data. In addition to the high accuracy achieved during the field acquisition, the multiple component data can be used in the post-acquisition processing to derive a coherent common signal that has a much higher signal-to-noise ratio (SNR). Work on data processing for deriving coherent signal has been reported previously. With increased data quality, it is then possible to approach the task of extracting parameters indicative of the geometry and magnetization distribution of buried metallic objects. For example, the ability to determine the quadrupole component of the source would be important to discrimination problems. The axial symmetry of most UXO items means that they will have a minimal quadrupole component, whereas irregularly shaped scraps will have a large quadrupole component.

Beyond the simple conceptual discussion, very little is available in the published literature on the relative strength of dipole and higher-order moments and how their responses manifest themselves in either total-field anomaly or magnetic gradients. Existing work invariably focuses on UXO-like objects and adopt a spheroid approximation. In the process, one large class of objects that may represent an important opportunity has been neglected. This is the class of irregularly shaped metallic objects that should be left in the ground.

A paper, *Numerical Modeling of Magnetic Moments*, is attached in the appendix and explains the theory upon which we hope to be able to extract diagnostic multipole data from TMGS data acquired in 2005 and 2006 at YPG when the calibration coefficients for the system are sufficiently accurate. We now have the ability to recover dipole and quadrupole moments from a total-field anomaly as well as gradient data and current work in a separate project examines the rule-based and stochastic approach to discrimination. The presence of large higher-order moments allows us to identify non-UXO's that should be left in the ground.

7.0 CONCLUSIONS AND RECOMMENDATIONS

7.1 Positioning

We had significant problems with GPS positioning both with ALLTEM and TMGS, although for different reasons. With ALLTEM we used a JAVAD RTK-GPS that provides a maximum position update rate of 1 per second. We also had “drop-outs” with this system and had to frequently sit and wait for “fixed” mode reacquisition before resuming data acquisition. Further, the positions that were recorded were not all accurate. Some of this appears to be loss of “fixed” mode and substitution of “float” mode locations which are not sufficiently accurate. We may also have had some software buffer problems in which the position written into the data header was not the most recent information. This caused some of our moving data to be “split” or shifted in

ways that are simply too tedious to try to manually adjust in OASIS Montaj. In response, we have decided to abandon use of the JAVAD and move to the Leica GPS owned by the Crustal Imaging and Characterization Team and therefore not exclusively dedicated to this project. We have rewritten the ALLTEM LabVIEW data acquisition software to accommodate the Leica GPS that has a 20 Hz position update rate, and plan to test our position data prior to the next YPG deployment. We think this will correct the obvious gross position errors.

TMGS positions are handled differently from ALLTEM positions. TMGS position data are written to separate files and associated with the data files in post-processing by matching time stamps. The time stamps were not accurate and caused headaches with respect to correctly recovering positions for the TMGS. We expect to have that problem fixed and tested prior to our May, 2006 deployment to YPG.

There yet remains a problem, however, that is demonstrated in the discussion in Section 5.7 above. That is, every RTK-GPS system uses algorithms to “improve” or interpolate positions on the fly. Various algorithms behave differently. Static GPS positions can usually be relied upon to be within the manufacturer’s specifications, but dynamic locations can be off by a few centimeters – and some systems in some cases by more than this. An error of a few centimeters is not much from a detection point of view, but may be unsatisfactory from a target discrimination point of view. We think that many GPS vendor personnel do not know or understand the details of what their own systems are doing internally and may be erroneously convinced that the dynamic positions provided by their systems are more accurate than they actually are. SERDP/ESTCP has recognized the position problem and has sponsored a workshop on precisely this topic.

We would like to evaluate laser positioning, which should be more accurate, and may recommend that ALLTEM and TMGS adopt laser positioning if our evaluation indicated a worthwhile advantage.

7.2 ALLTEM

ALLTEM had some prototype problems in the field that included broken wires and connectors, loose boards, and high-frequency coherent noise that we have not been able to identify. Nevertheless, we are generally pleased with the data that the system produced. We have added four more receiving loop antennas and a new switching matrix, new boards, and new software control so that we can select the channels that seem to provide the most diagnostic information about targets as determined from the algorithms discussed in section 4.0 above. Thus ALLTEM as deployed in 2006 will be more flexible and should also be more robust than it was in 2005.

Though ALLTEM was far more stable than VETEM at YPG and its response to the ground was much less, system drift and ground response remain as issues for both the lower limit of target detection and the lower limit for target parameter extraction leading to the ability to discriminate. We have pushed the Tx moment nearly as high as we can without very challenging engineering problems, and we are operating in a range of

“tradeoff” between on-the-fly signal averaging, spatial data density, and operating speed. We don’t see a large improvement here in dynamic data acquisition. Some adjustments could still be made to the cube and coil dimensions and placement. This could be guided by a combination of modeling using the new forward modeler described in section 4, and practical size considerations. We are recommending the addition of thermistors to the Tx coils because we are convinced that mechanical expansion of the Tx windings with heating of the windings is causing “leakage” of the primary field into the Rx channels and that this could be tracked by knowing the Tx loop temperatures and correcting in post-processing, but have not had sufficient time to implement this. A more difficult engineering approach would be to actively change the differential Rx loop gains on the fly to minimize the primary signal leakage changes. Another approach that we did not investigate for lack of time is the possibility of active electronic “bucking” of the primary in place of, or as a supplement to, symmetric Rx coil bucking. This might be relatively straightforward except for large signal amplitudes in that the primary signal is ideally a simple voltage square wave. The system drift, after the first 15 minutes or so, is mostly slow so that over a period of a few minutes a linearly interpolated correction appears to be quite satisfactory. This is relatively easy to do on a line-by-line basis for dynamic data if the recoded lines extend beyond the boundary of the target-occupied grid and assuming the ground conditions are relatively uniform on each line. For the high-density “tic-tac-toe” data, however, the drift is both larger, because of the greater time interval, and harder to remove because at the ends of each line the signal is generally being influenced by a nearby target. Thus, our tic-tac-toe data are influenced by drift and also perhaps by topography. The cart “tilted” quite a bit on some lines.

In addition to thermistors and more accurate positioning, we think an array of height-above-ground sensors as well as accelerometers and inclinometers might pay dividends in our ability to derive target parameters from both static and dynamic data.

Finally, we recommend the acquisition of a significant suite of static target data using some of the most common UXO items. This could be beneficial in matching the parameters extracted from our data by means of the processing/inversion algorithms described in Section 4.0 above and for other investigators who may want to study the merits of ALLTEM data for target discrimination.

7.3 Cart

The present cart, constructed of plywood and not considered the “final solution,” acquitted itself well with one minor and one major exception. The major exception was wheels and bearings. This may be seen by examining Table 1.1. Wheel bearing failures were common. We have now replaced all bearings having balls and races with bushing bearings to distribute the load over a large area. The bushings should be adequate for the low speeds we will use. Tests are pending. We had filled three tires with a foam that set to a solid to avoid punctures in our tires. This had two undesirable outcomes. First, the 6 pound tires became 75 pound tires, and the foam, after a time, shrank away from the wheel hubs causing wobble that contributed to the less serious problem -- the cart does not track straight behind the towing tractor. Thus, even when the driver kept the tractor

very closely on the desired line, the cart track might deviate as much as ± 50 cm from the desired line. This can be somewhat reduced by using a very long straight approach into each line, but that adds extra time and terrain constraints place an upper limit on the ability to extend lines. In May, 2006, we will try to use air-filled tires with a puncture sealant. The wobbly foam-filled tires will be a back-up. In addition, the tongue attachment to the front steered wheel is being modified to add a triangular brace with the intention of forcing the front wheel to track more in-line with the tractor.

7.4 Visual Data Inspection

Fully automated data processing and inversion of geophysical data is a highly desired objective. It reduces the man hours spent on data processing and may produce less “subjective” and more consistent results and do it with less experienced and trained personnel. However, as noted in Section 4, the ability to extract target parameters will have an effective cutoff depth that is not as deep as the ability to detect a target, especially so if detection is based on visual observation of 2D or 3D maps produced from data by a gridding algorithm such as those used in OASIS Montaj or Surfer and where the user can adjust the color mapping, shaded relief, artificial illumination and viewing perspective to make features “pop out” from the noise. It may be that some at least qualitative target information can be extracted by viewing the images. An example is the 155 mm target buried at 1.5 m deep at grid location B4 . This location is indicated by a black arrow in Figure 3.21. The signal is near the SNR limit for this along track excitation and observation. For the horizontal excitation and observation across track, shown in Figure 3.20, the target signal has dropped below the SNR. This suggests that the target is ferrous and longer along track than perpendicular to track. It is not likely that an automatic algorithm, especially one that uses thresholding, could tell this. We plan to use both automatic processing/inversion algorithms and human examination on the Blind Test Grid data set.

8.0 REFERENCES

Gill, P. E., Murry, W., and Wright, M. H., 1986, Practical Optimization, Elsevier, Amsterdam, 401 p.

Jackson, J. D., 1999, Classical Electrodynamics, 3rd edition, Wiley and Sons, Hoboken, NJ, 808 p.

Oden, C. P., 2006, Calibration and Data Processing Techniques for Ground Penetrating Radar Systems with Applications in Dispersive Ground, PhD Thesis, Geophysics Department, Colorado School of Mines, Golden, CO, USA, 249 p.

Oden, C. P., Wright, D. L., Powers, M. H., and Olhoeft, G. R., Rittgers, J. B., Irons, T., and Meininger, A. J., 2006, Estimating Soil Properties under Ground-Coupled GPR Antennas, in Eleventh International Conference on Ground Penetrating Radar, Columbus, Ohio, submitted.

Olhoeft, G.R., Powers, M.H., and Capron, D.E., 1994, Buried object detection with ground penetrating radar: *in* Proceedings of Unexploded Ordnance (UXO) Detection and Range Remediation Conf., Golden, CO, May 17-19, 1994, pp.207-233.

Zhdanov, M. S., 2002, Geophysical Inverse Theory and Regularization Problems, Elsevier, Amsterdam, 628 p.

9.0 APPENDIX – PAPERS

Two draft papers are attached:

1. *ALLTEM for UXO Applications – First Field Tests*
2. *Numerical Modeling of Magnetic Moments for UXO Applications.*

ALLTEM FOR UXO APPLICATIONS – FIRST FIELD TESTS

*David L. Wright, Craig W. Moulton, Theodore H. Asch, Philip J. Brown II, S. Raymond Hutton,
U.S. Geological Survey, Denver, CO
Misac N. Nabighian, Yaoguo Li, Colorado School of Mines, Golden, CO*

Abstract

The ALLTEM system is a multi-polarization electromagnetic induction (EMI) system that uses a continuous triangle-wave excitation to drive each of three orthogonal (H_x , H_y , and H_z axes) transmitting coils. Received data are recorded on multiple simultaneous receiver channels. Multi-polarization excitation and received target data have potential advantages for determining location and orientation, and for discriminating between unexploded ordnance (UXO) and non-UXO objects. Tests at the Denver Federal Center (DFC) showed high sensitivity to the conductive ground, but buried target signatures can be recognized in the data in real time from time decay shapes. Tests at the UXO Calibration Grid at the Yuma Proving Ground (YPG), Arizona, demonstrate good detection, orientation, and composition sensitivity to buried UXO and non-UXO targets, good system stability, and much less sensitivity to the ground than at Denver. Discrimination between ferrous and non-ferrous targets is particularly simple. Multiply polarized data and time constant extraction from the data provide additional target information.

System Description

The ALLTEM system is unusual in that the transmitting (Tx) loops are driven by a continuous triangle current waveform and the resulting electromagnetically induced target responses are treated in the time domain. The measured quantity is the voltage in receiving (Rx) induction loops. This is theoretically equivalent to an integration of the voltage measured by a conventional EMI system that relies on a rapid current turn-off in a Tx loop. Practically, the use of a triangle wave results in much smaller early-time voltages induced in the Rx loops, reducing dynamic range demands on the receiver. Another useful consequence is that ferrous and non-ferrous targets show distinctly different waveforms (Wright et al., 2005). The UTEM system developed at the University of Toronto some years ago was a pioneer in the use of a triangle waveform in EMI systems (West et al., 1984) and has a theoretical advantage of emphasizing highly conducting targets buried in a less conductive host (Smith and Annan, 1998). ALLTEM is intended to obtain the advantages of triangle wave excitation in a system whose dimensions, characteristics, and geometry are appropriate to UXO applications.

Beyond detection of metal objects, the ability to discriminate between UXO and non-UXO targets is a highly sought after goal, because in many cases more than 70 per cent of range clearance costs are attributed to digging up harmless scrap metal that could have been left in the ground. An ideal UXO EMI system would not only have a very high probability of detection, but also the ability to discriminate irregular or “plate-like” shapes from “rod-like” ferrous objects that likely are UXO. Some UXO items are composites of ferrous and non-ferrous parts, but, unlike landmines, there is little incentive to eliminate ferrous materials, thus the great majority of UXO items have significant ferrous metal content. As we have already mentioned, a very useful consequence of the triangle waveform is an ability to easily distinguish between ferrous and non-ferrous metals. As a further aid to discrimination, we have designed ALLTEM with a multi-axis capability. There are three orthogonal Tx loops, an array of five Rx loops on the top and bottom of a 1 m cube, and Rx loops on each of the four vertical sides of the cube as shown in Figure 1. Voltage outputs of loops on opposite sides of the cube are subtracted to remove the large primary field response. Consequently, the system measures field differences.

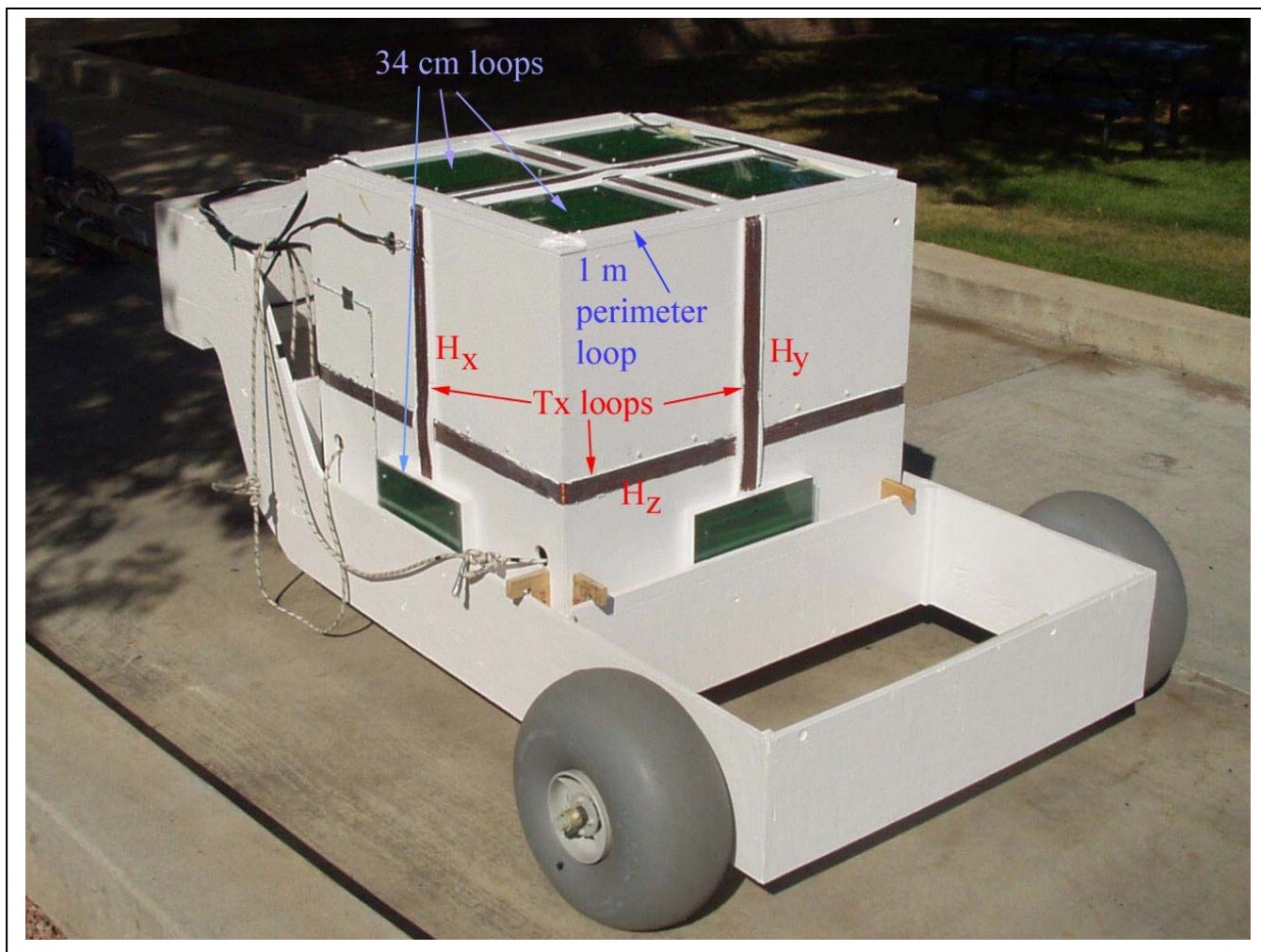


Figure 1: The ALLTEM 1 m cube mounted on a cart. The Tx loops produce magnetic fields in three directions (H_x , H_y , H_z). The top and bottom faces contain a 1 m square Rx loop around the perimeter and four 34 cm printed circuit board Rx loops on 50 cm centers. Each vertical face has one 34 cm Rx loop to measure fields in the two horizontal directions (H_x and H_y). Because a transmitter is always on, opposite Rx loops are paired as gradiometers to cancel the primary field.

The triangle waveform frequency can be varied, within limits, under software control, but for several reasons we have settled on 90 Hz for field work. First, a half-period at 90 Hz is long enough to measure time decays for most UXO objects. Second, higher frequencies require higher driving voltages to maintain the same current amplitude. Third, averaging waveforms over three cycles at 90 Hz greatly reduces 60 Hz interference. To minimize 60 Hz interference, the triangle wave frequency should be $(n+1/2) \cdot 60$ Hz where “n” is an integer, i.e. 30 Hz, 90 Hz, 150 Hz, etc. Finally, 90 Hz allows us to do some waveform averaging before recording yet retain good spatial data density while moving at speeds up to or slightly faster than 1 m/s.

The Tx loops are each 63 turns and the current waveform that we apply to these loops is symmetric about zero amperes. The amplitude is variable under software control, but we generally run using a peak amplitude of 8 A. The peak Tx loop moment in this case is thus about $500 \text{ A} \cdot \text{m}^2$. Each Rx loop has 200 turns. A higher voltage gain is applied to the 34 cm Rx loop outputs than to the 1 m Rx loops so that the voltage inputs to the digitizer for the same target are comparable.

The digitizer has eight simultaneous channels digitizing to 24 bits at a rate of 100 kilosamples/s. The 90 Hz triangle wave frequency is derived from the digitizer clock frequency to keep everything phase locked. The three-cycle averaged data may be further averaged under software control from one to 10 times before recording. A spatial data interval of 20 cm or less is used for each recorded channel along a line to ensure that each Rx gradiometer loop pair has more than one “look” at even the smallest and shallowest target it may pass over.

The data acquisition software, written in National Instruments LabVIEW, allows the operator to select the receiver channel/s to display in real time and view raw waveforms or a strip-chart style display of sums and differences between amplitudes near the beginning and end of the waveforms. The latter style can be useful for ferrous/non-ferrous target discrimination. All viewing options are also available when playing back recorded data. Illustrations are given below in the discussion of field results.

It is common for TEM systems to implement one or several “time-gates” with digital or analog signal averaging to improve the signal-to-noise ratio (SNR) in each time gate. However, we have chosen to record all the points along the waveforms at the full 10 μ s/sample rate. This is possible because mass storage has become inexpensive and the data rates can be managed. After waveforms are recorded, any desirable form of digital data processing can subsequently be implemented. To improve SNR we may average waveform groups provided that we retain adequate spatial data density while doing so. Averaging waveforms before writing to mass storage reduces file sizes.

In order to most faithfully preserve waveform shapes it would be ideal to dispense with all analog hardware filters, but in most environments, especially the noisy Denver metropolitan area, we find that we cannot remove all filters. Three types of hardware filters exist in the system. A high-pass filter with a cut-off at 1 Hz blocks any amplifier DC offsets. A Bessel 2-pole low-pass filter, designed for little or no overshoot when a voltage step is applied, and whose cutoff frequency is selectable at 5, 7, 17, or 90 kHz limits high-frequency noise. We almost always use 5, 7, or 17 kHz to reduce radio (Very Low Frequency stations in the 20+ kHz range and other) interference. There is also a 60 Hz hardware notch filter to further reduce 60 Hz interference. When possible, we avoid using the 60 Hz filter because it introduces significant distortion “droop” on the recorded waveforms. The 60 Hz filter must be used in our building at the DFC, however, because the 60 Hz interference would otherwise swamp the smaller target signals and render them undetectable. The digitizer we are using has a powerful 50 kHz low pass 8th order “brick wall” filter to prevent any possible aliasing. Some researchers have noted that this brick wall filter distorts fast time-domain transients. We have not encountered this because with our triangle wave and our low-pass hardware filters, we have little spectral content close to or exceeding 50 kHz.

Denver Federal Center Tests

The first outdoor tests of the ALLTEM system were done at the Denver Federal Center. The earth response was much stronger than we had expected. This might be due to an unusually wet spring season that increased soil conductivities. When we buried a steel sphere and a brass sphere, we noted that the soil was moist right up to the surface. By subtracting a waveform recorded where there were no targets we could easily discern the signatures of the brass and steel spheres and distinguish between the two (Figure 2), but the response to the earth was sometimes as strong as the response to the targets and was clearly quite sensitive to the height of the coils above the ground. In order to assess the geometrical relationship between height and earth response, we performed an approximate analysis based on Nabighian’s equivalent “smoke ring” formulation (Nabighian, 1979). Figure 3 shows the ALLTEM cube suspended from a tree branch during our tests. Figure 4 shows relative voltage calculations based

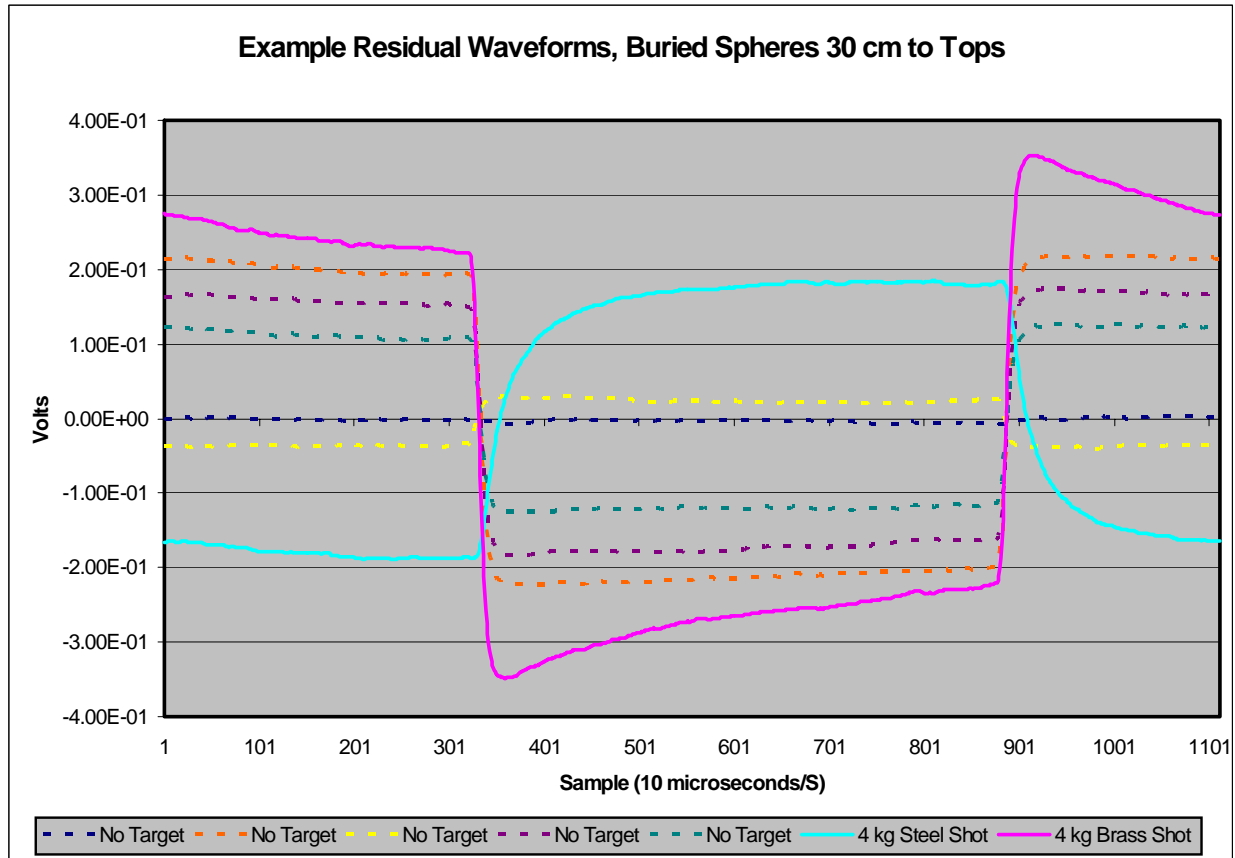


Figure 2: This figure demonstrates the difference between the target signatures for a brass and a steel sphere (both 4 kg) and also the strong and variable earth response at the DFC, shown by the dashed data.



Figure 3: The suspended ALLTEM cube.

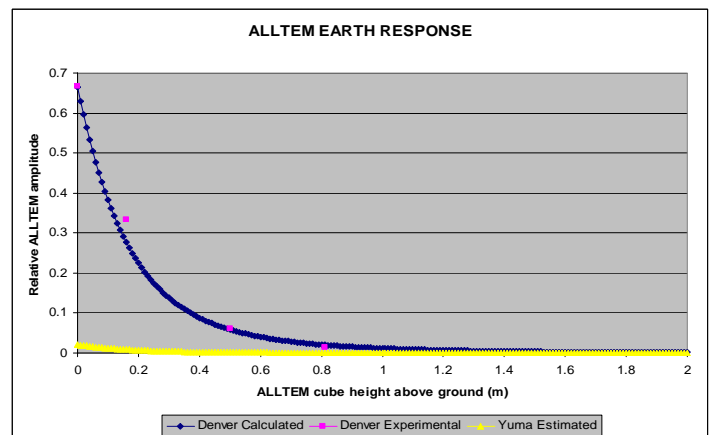


Figure 4: Response vs. height above ground.

on the smoke ring approximation. The blue curve is the normalized voltage response based on the model. The pink dots are measured data. The agreement is clearly quite good. The yellow curve is a calculation based on an expected difference between the earth electrical conductivity at YPG and at the DFC. Specifically the calculation assumes that the electrical conductivity of the ground at YPG is a factor of 10 less than at the DFC. If this were true, the magnitude of the earth response at YPG should

be a factor of 30 less than at the DFC. Whether or not this is precisely correct, the earth response at YPG was indeed much less than at the DFC. Measured DC earth conductivities at the DFC have been as high as 200 mS/m. Reported values at YPG have been in the neighborhood of 10 mS/m. The only remaining surprise to us is that the earth response does not decay to zero with time as we expected.

Yuma Proving Ground Calibration Grid Tests

The U.S. Army Corps of Engineers, with support from the Strategic Environmental Research and Development Program, has built standardized UXO test ranges, one of which is located at the YPG. During October, 2005, the ALLTEM system was operated over the Standardized UXO Calibration Grid at YPG (Figure 5).

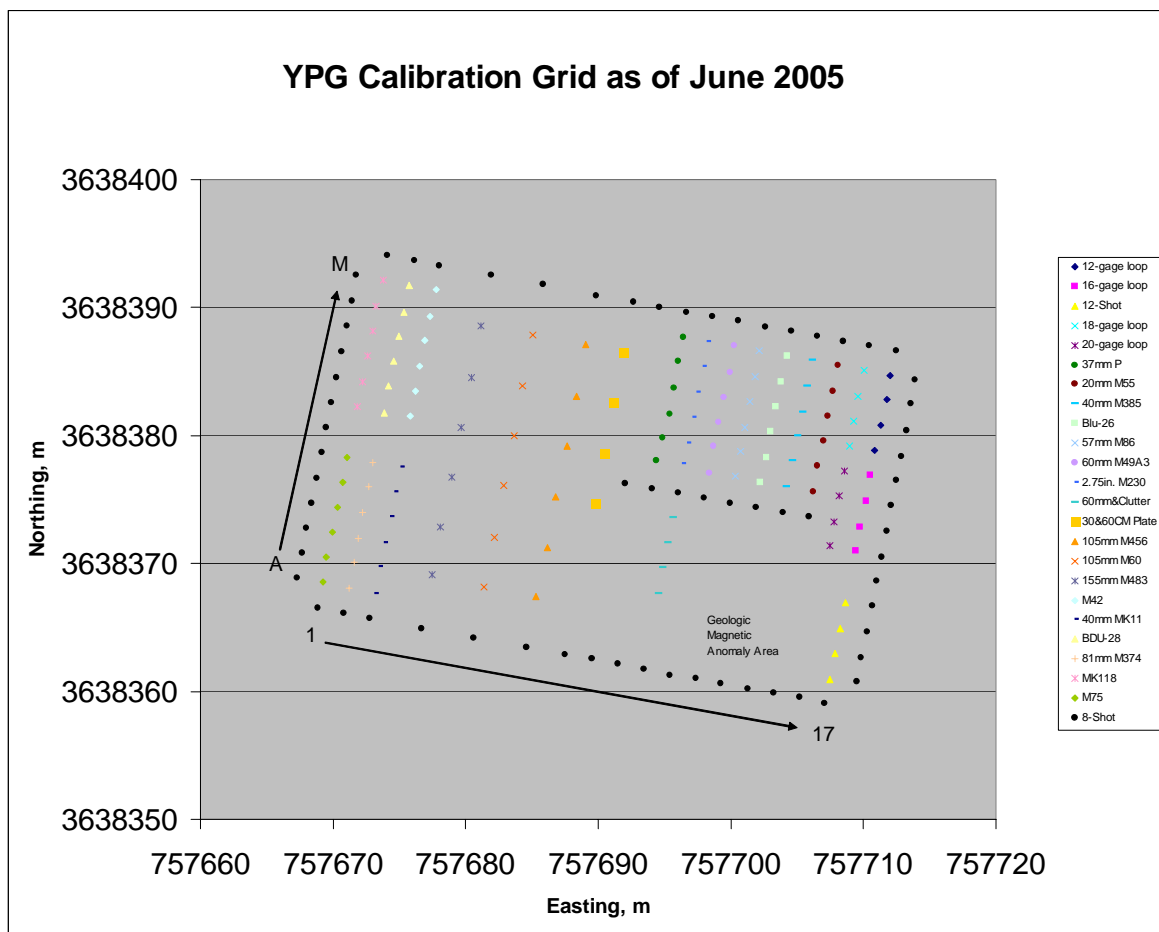


Figure 5: This figure shows the Calibration Grid in the most recent configuration. The grid was modified from the original configuration to remove targets from the region annotated “Geologic Magnetic Anomaly Area.” The targets were moved to the west side of the grid. The legend at the right hand side identifies the targets. Figure courtesy of U.S. Army Environmental Center (USAEC).

We tested ALLTEM in several ways at YPG. Not all of the data have been quantitatively analyzed as of the writing of this paper, nor can we show all the permutations and combinations that were used. However, we can say that we are quite pleased, overall, with the performance of the system. The system response was calibrated at least every morning and afternoon by repeated occupation of a

given position and data were recorded while the system was static with no target, a steel sphere target, and a brass sphere target, which were mounted above the cube on a rigid plastic tube. Dynamic position errors and offsets were tested by towing the system while recording target and GPS data. In addition, the cube was raised about 1 m off the ground and primary fields were minimized or “nulled” by adjusting the voltage gains applied to opposing coils after the system had been allowed to thermally stabilize for over an hour. We discuss system drift below. ALLTEM was then run three times over the grid at 0.5 m nominal line spacing at a speed of about 1 m/s. On the first survey the horizontal Tx coil, generating a vertical magnetic field (H_z), was driven. On the second survey the H_x (magnetic field along line) Tx coil was driven, and on the third survey the H_y (magnetic field across line) Tx coil was driven. Then three targets -- a 20 mm M55 projectile, a 60 mm M49A3 mortar round, and an 81 mm M374 mortar round -- were chosen and a 3-m square grid, at 25 cm station spacing, was run over each of the three targets using manual placement of the cart at each station. Finally, the entire grid was run again at a reduced speed of about 40 cm/s while ALLTEM multiplexed through all three Tx polarizations.

Vertical Polarization

Figure 6 shows a map made from raw unleveled ALLTEM data when the H_z Tx coil was driven and the received H_z gradient recorded from the 1 m square receiving loops is displayed.

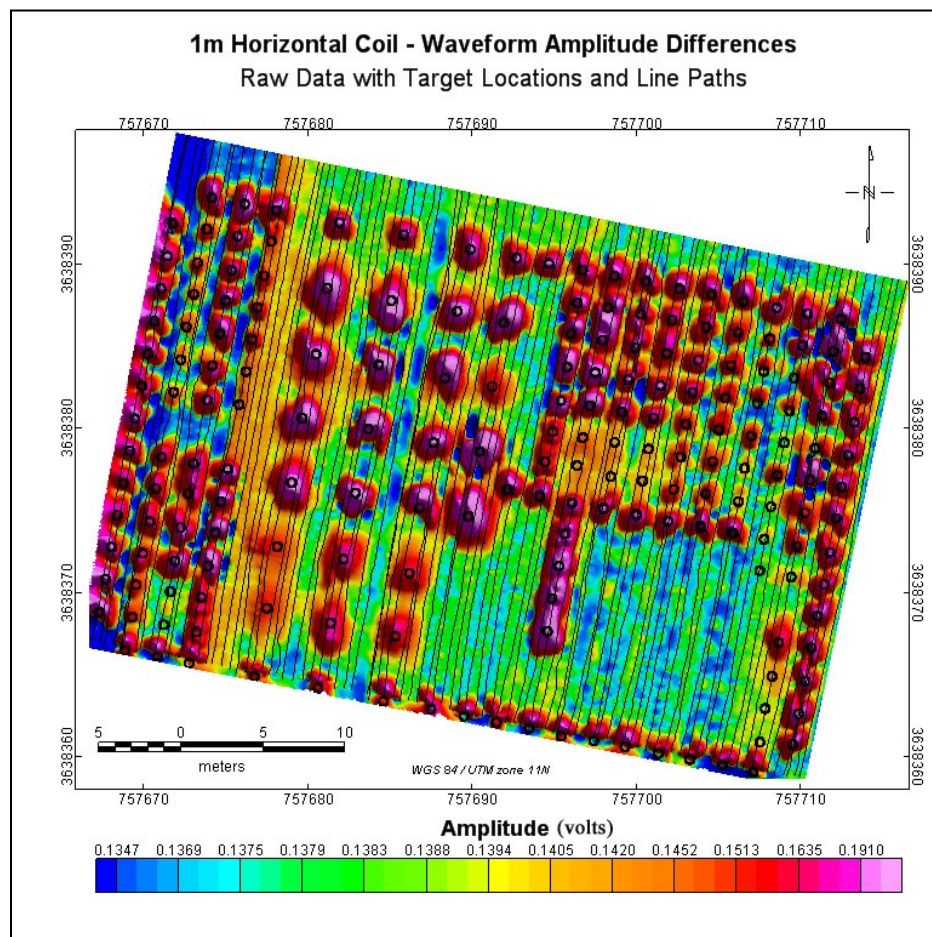


Figure 6: An amplitude difference map from raw unleveled ALLTEM data. Most of the targets, marked with small black open circles, have been detected. The line trajectories, not always straight, are also shown. The system appears to be relatively stable. The one obvious “tear” follows a 1 hour delay.

We were quite pleased with what we saw in Figure 6, especially compared to our VETEM system results of 2003. VETEM detected 90 percent of the targets, but only after extensive data processing which was necessary because we operated VETEM with an overlapped Tx/Rx loop configuration that was mechanically very difficult to keep sufficiently stable, and because VETEM responded very strongly to the earth, as indeed it was designed to do (Wright et al., 2004). The delay of one hour noted in the caption of Figure 6 resulted from the failure and replacement of a wheel bearing. The type of bearing we used proved inadequate and needs to be replaced, perhaps with (non-metallic) bushings.

Horizontal Excitation with Vertical Gradient Detection

When the excitation is in the H_y direction, across track, and the vertical field gradient is measured, the mapped data look like Figure 7.

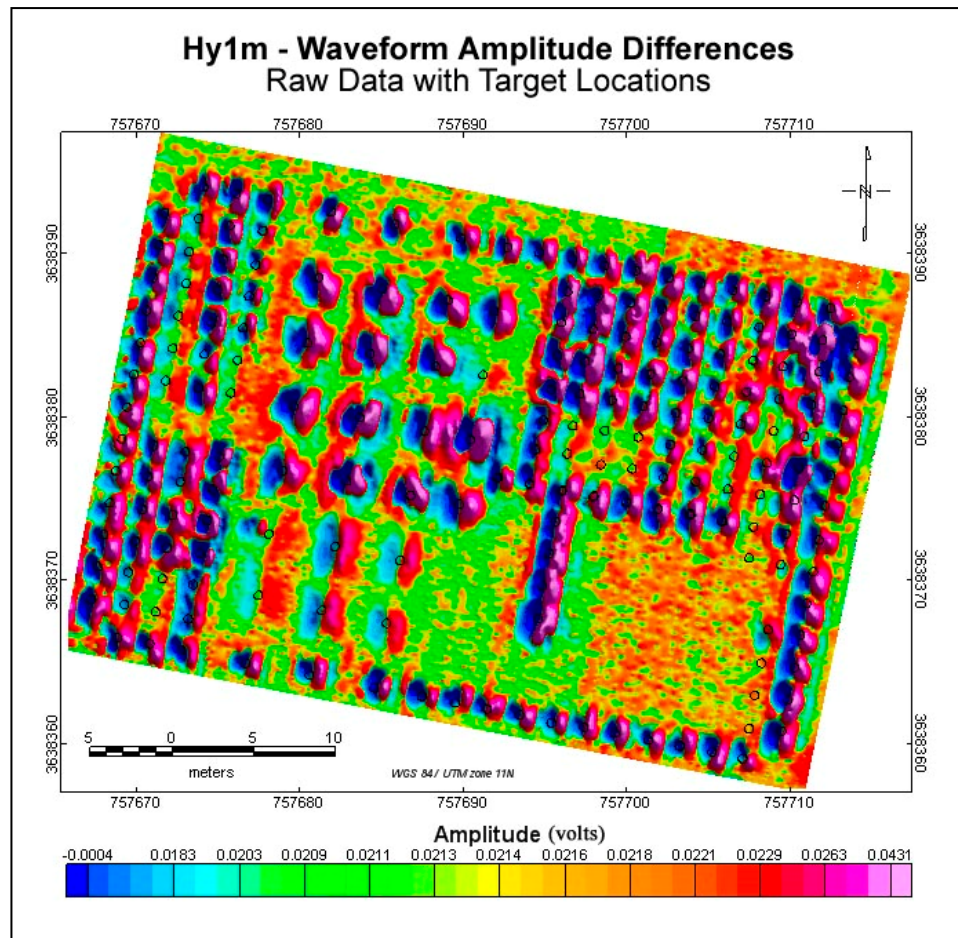


Figure 7: An amplitude map of raw data obtained when the cross track (H_y) Tx coil is driven and the vertical magnetic field gradient is recorded. Target responses are positive when the driving coil is to the right of the target and negative when it is to the left of the target. These responses are superimposed on a non-zero DC level that has not been removed. If a spherical target were bisected by the plane of the Tx coil, there should be zero response, so target locations are approximately on zero crossings.

Horizontal Excitation with Horizontal Gradient Detection and an Undocumented Target

Another polarization combination is shown in Figure 8, where the H_y horizontal Tx coil is driven, as in Figure 7, but the horizontal gradient is the measured data. This combination adds a horizontal spatial derivative and looks “bumpier” across track. This is consistent with modeled data.

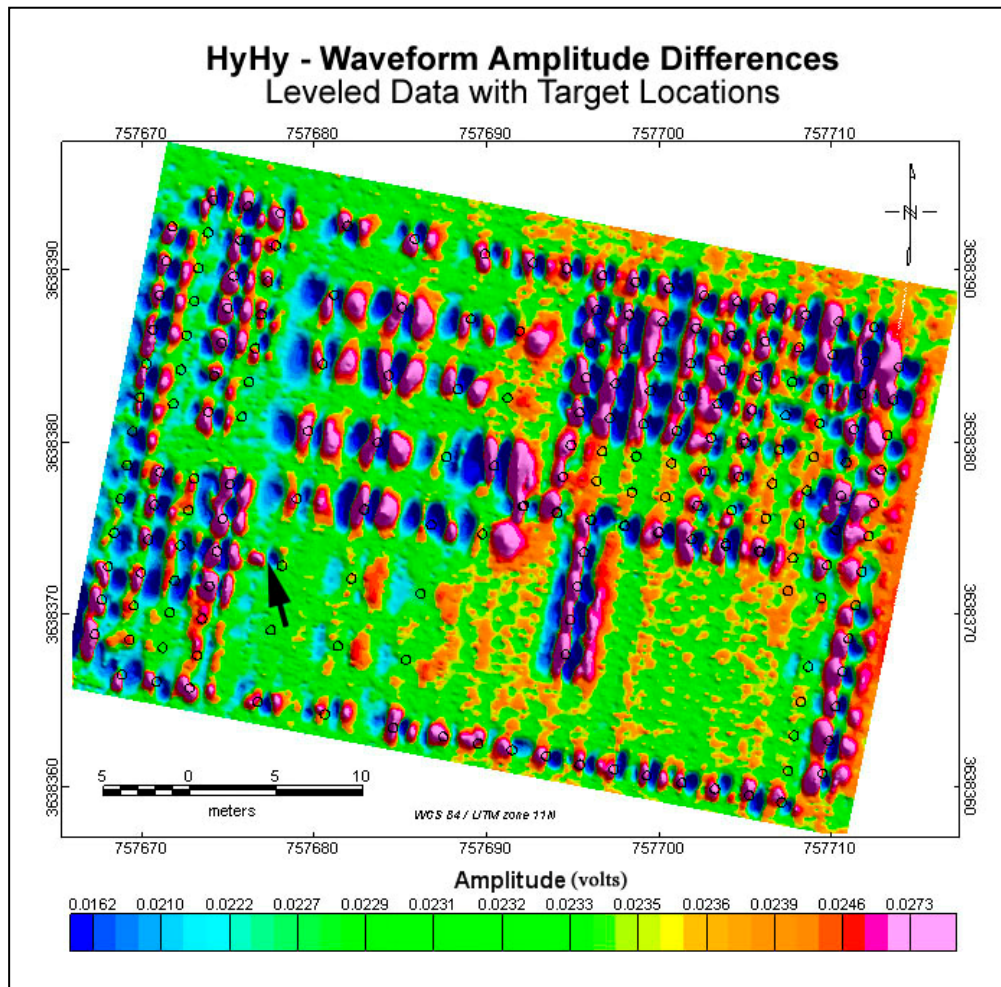


Figure 8: A leveled amplitude map for the case where the cross track (H_y) Tx loop is driven and the H_y horizontal gradient received data are displayed. The black arrow points to the location of a probable small, shallow, undocumented target. The horizontal gradient data shown here are less responsive to the deep target, but very responsive to the undocumented, relatively shallow target.

One utility of multiple polarization data is illustrated by our identification of what we think is a small, shallow, undocumented target slightly to the grid WNW of a documented 155 mm M483 projectile. The M483 is buried 1.5 m deep. Its signature is broad and intersects the signature of the shallower undocumented target in the vertical polarization data of Figure 6. In Figure 6 the undocumented target signature appears as an indistinct lobe extending west from the signature of the M483 projectile. Figure 7 also shows evidence of this target. It was not on the surface or we would have seen it. We understand from Mr. George Robitaille, USAEC, that we were the first to call attention to this object.

Benchmark EMI Data

Apparently, the undocumented target is not related to the recent reconfiguration of the grid, because we also see evidence of it in the benchmark EM-63 data obtained over the original calibration grid configuration (Figure 9). Figure 9 is unleveled EM-63 amplitude data from channel 2, an early time gate. Early time data are more responsive to small targets such as a 20 mm M55. The maps produced from the EM-63 data show the majority of the targets on the Calibration Grid as it was originally

configured, including several 20 mm M55's. The EM-63 data show a few shifts, presumably due to instrument drift or instability.

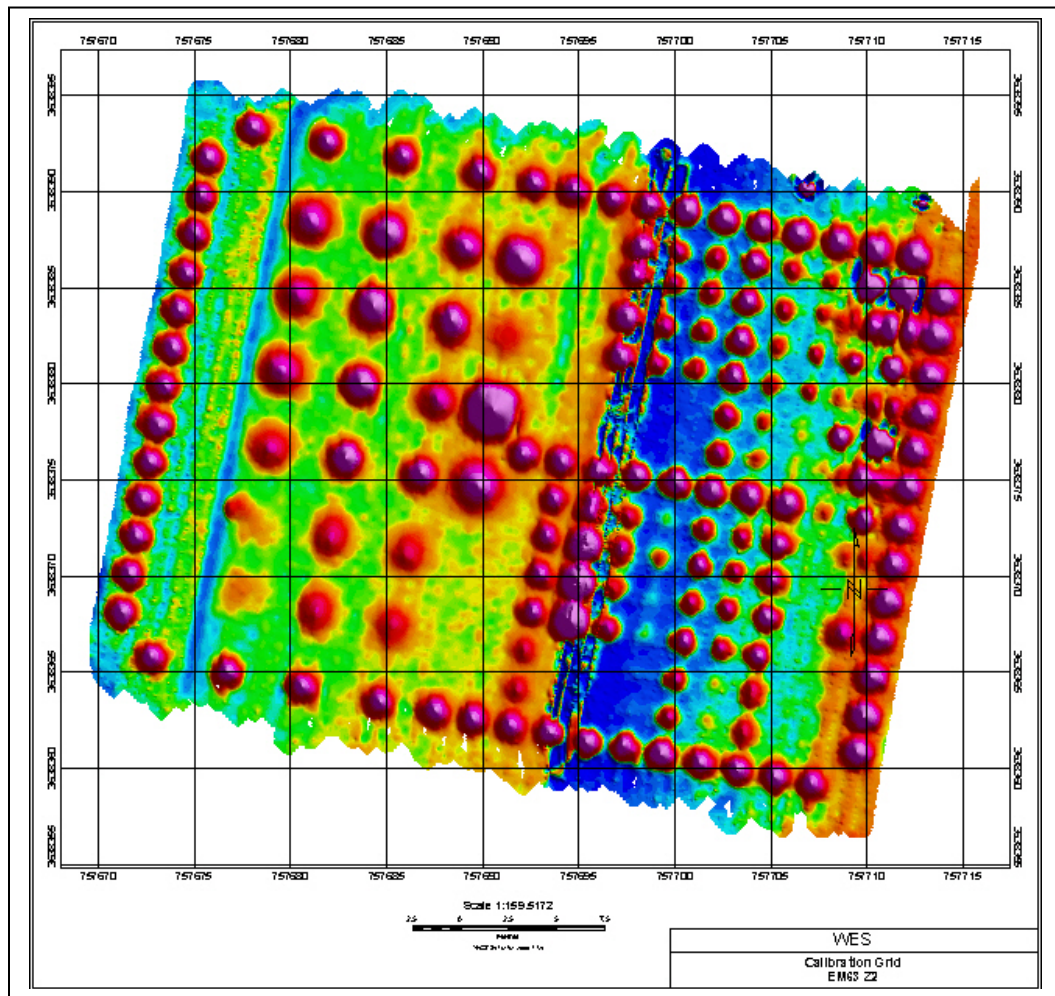


Figure 9: This signal amplitude map of channel 2 EM-63 data (volts) was furnished to us by Mr. Ryan North, U.S. Army, Engineer Research and Development Center, Vicksburg, MS. Note that this map is of the Calibration Grid in its original configuration. Some targets have since been moved. Evidence of an undocumented target is in the first lane of targets to the right of the west boundary markers.

Stationary Square Grid (Tic Tac Toe) Data

Data over 3 m by 3 m squares on 25 cm station spacing were taken with all three polarizations over a 20 mm M55 projectile, a 60 mm M49A3 mortar round, and an 81 mm M374 mortar round. The cart was stationary when data were recorded and waveforms were averaged to increase the signal-to-noise ratio (SNR). The cart was positioned by hand. The purpose was to provide data that could demonstrate what could be derived from data with a high SNR and relatively small station spacing. In this “cued” mode, target discrimination is the main objective rather than detection alone. Figure 10 shows an example of vertically polarized data over the 60 mm M49A3 mortar round. This target is buried in a horizontal orientation along the grid north, i.e. magnetic north, at a depth of 0.25 m to its center. The SNR for this target appears to be quite good. The target response pattern is a “double peak” and the maximum value is not directly over the target. This is a consequence of a spatial convolution of the target characteristics and the magnetic field patterns of the Tx and Rx loops. The southern peak is

slightly higher. The likely explanation is that the M49A3 has a magnetic asymmetry. It has ferrous tail fins (to the south), but has non-ferrous parts, including some non-metallic parts in the nose. Pattern

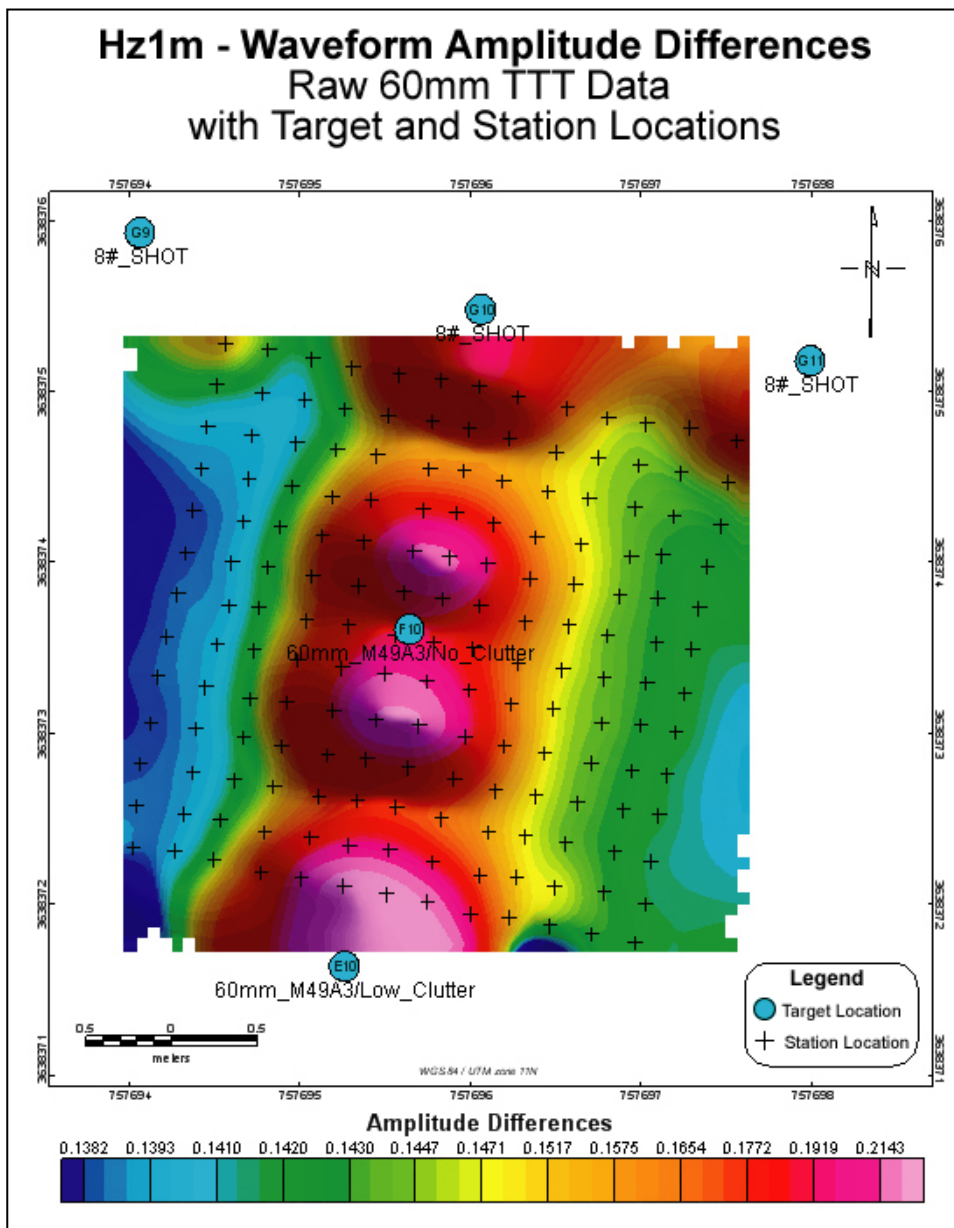


Figure 10: This map shows an amplitude (volts) spatial pattern over a horizontal 60 mm M49A3 mortar round (box at right) when the mortar round is illuminated with a vertical magnetic field and the vertical magnetic field gradient is observed. The small crosses are the station locations (25 cm centers).

asymmetry for this type of UXO was previously observed in laboratory data (Wright et al., 2005). Data for the other polarizations and other targets also appear to have relatively good SNR.

Data Preprocessing

The ALLTEM data acquisition program permits the ALLTEM operator to watch data in real time. In addition, we can use the same LabVIEW program for waveform visual playback, with or without digital filtering and background removal. When we prepare data for mapping using Geosoft Oasis montaj,

preprocessing is done using a combination of LabVIEW and Oasis montaj. Typically, the following steps are done in LabVIEW:

- Strip ASCII headers from a line file and build waveform arrays.
- Pull the GPS Latitude/Longitude from stripped ASCII headers.
- Convert the HH.MMmmmm formatted GPS data to HH.MM.SS.ssss format (for Oasis).
- Remove redundant GPS values (typically generated before the cart starts moving and if data are written more than once between GPS position updates) and replace with Oasis null values (*).
- Build arrays of amplitude picks from the raw waveforms.
- Output the amplitude picks and corrected GPS to text files.

The above steps may involve filtering and background removal, or not. The following steps are done in Oasis montaj:

- Convert Latitude/Longitude to projected XY (Universal Transverse Mercator in meters).
- Interpolate null GPS values.
- Correct for GPS and system latency.
- Correct for GPS antenna to ALLTEM antenna offset.

The amplitude maps shown in this paper were made using Oasis montaj.

Waveforms and Time Constants

One version of the LabVIEW playback software we have written allows the user to watch waveforms as a slider is moved along the records from a chosen file (line). For waveforms of interest, a portion of a waveform can be selected with cursors and a single and double exponential fit can be performed on the selected portion of the data. This is only preliminary to a more systematic mode of extracting information from waveforms, but is instructive. Figure 11 shows a screen grab of residual (background subtracted) waveforms along line 11.

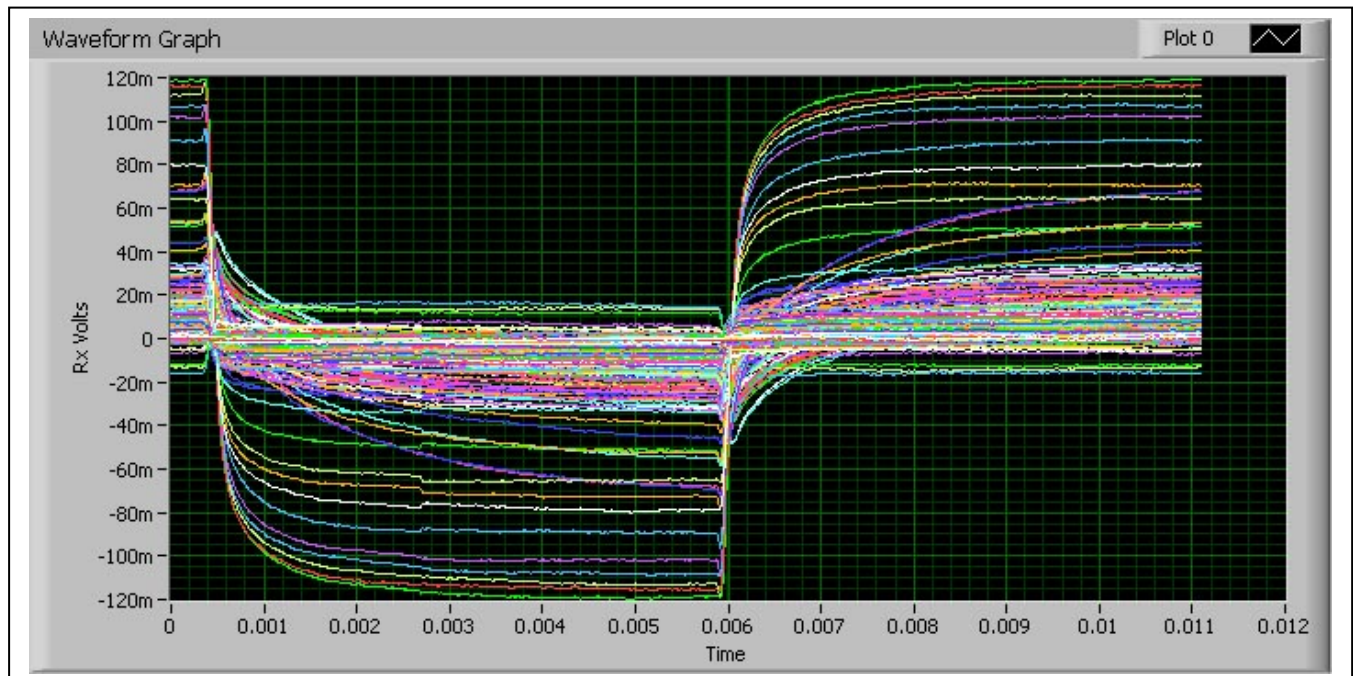


Figure 11: This graph shows the residual waveforms along line 11 on the Calibration Grid. Line 11 passes over the second lane of targets to the right of the boundary markers in Figure 6. On this line the sensors pass over spherical marker shots, 81 mm M374's and BDU-28 targets that have a combination of ferrous and non-ferrous parts. Decay rates and initial deflection polarities differ appreciably.

Figure 12 shows residual waveforms at a given location in the upper panel. The selected waveform in the file is indicated by the cursor in the bottom panel. The bottom panel also shows two amplitude profiles along the profiled line. Figure 13 shows one of the waveforms with cursor locations

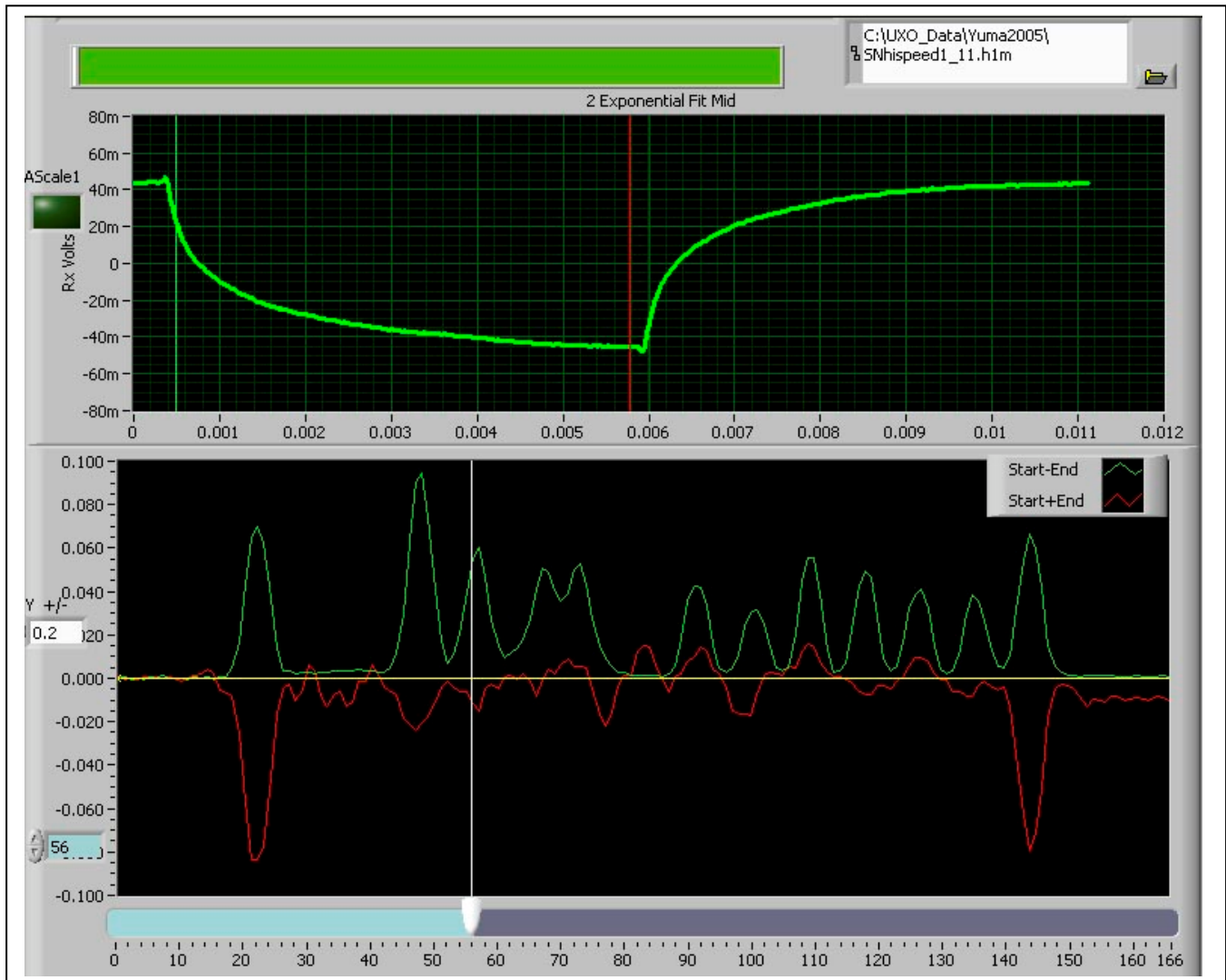


Figure 12: This screen grab shows a residual waveform (Rx voltage vs. time in seconds) and two cursors (upper panel) at the 56th waveform (cursor in bottom panel). The bottom panel plots are the sum (red) and the difference (green) of the amplitudes at the upper panel cursor locations. For high SNR the deflection polarities are opposite for most ferrous targets. Composite targets give inconsistent results.

shown in the top panel. The bottom panel shows the portion of the data between the green cursor and red cursor in the upper panel, and a single exponential curve fit and a two-exponential curve fit with the exponentials plotted. Two exponentials usually fit the data very well. The early portion of the waveform and the corresponding fast exponential may be strongly influenced by our low-pass filter.

Ground Response at YPG

In the tests at the DFC, the response to the ground was very pronounced with amplitudes of hundreds of mV (see Figure 2). We have noted above that the ground response at the YPG Calibration Grid was much smaller, but it was not zero. We have selected portions of two lines that have no targets,

subtracted a background and plotted the resulting waveforms in Figures 14 and 15. Amplitude changes of up to about +/- 16 mV are observed on the portion of line 49 we selected.

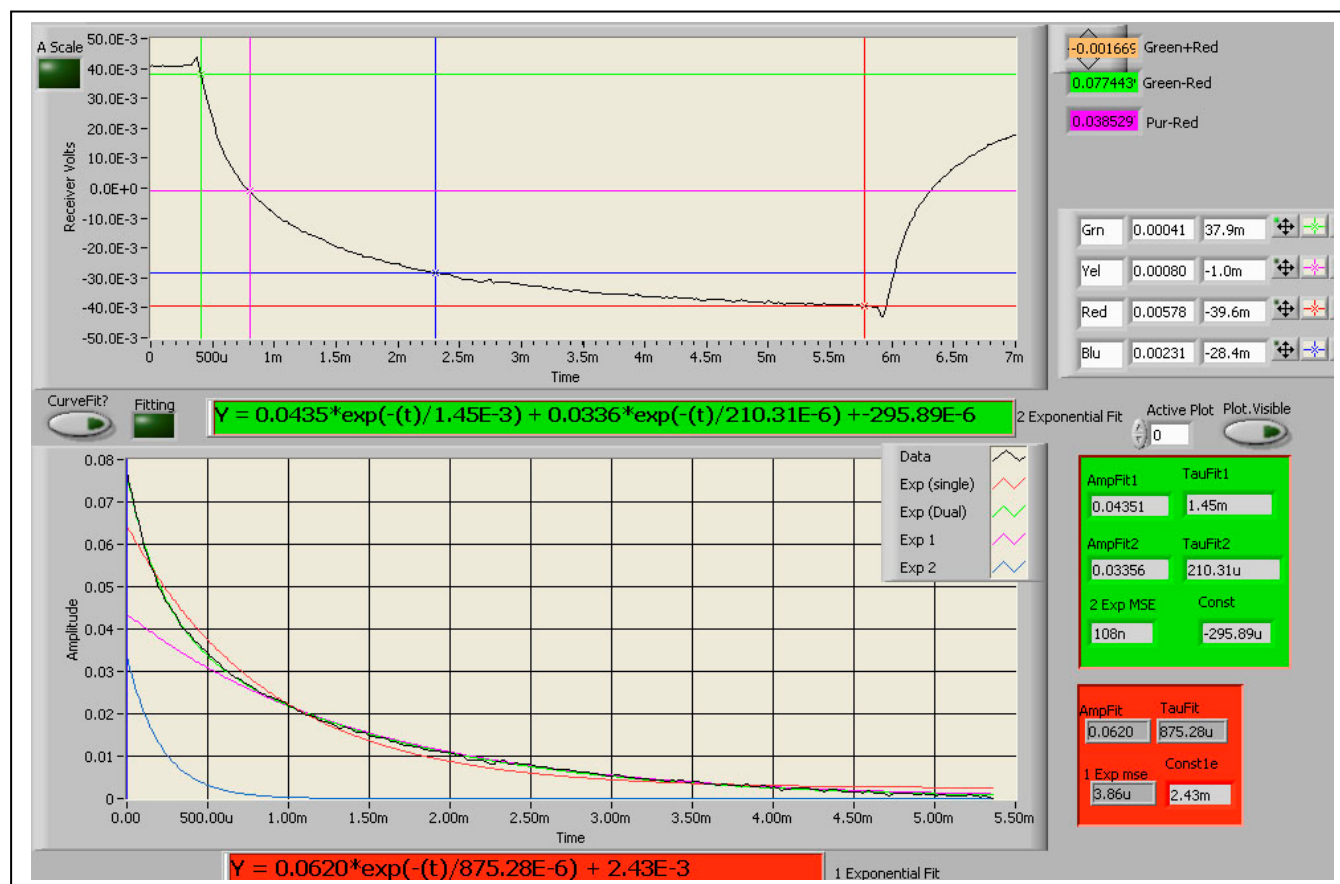


Figure 13: This figure shows a waveform over an 81 mm mortar round in the top panel. The bottom panel shows the data (black line) selected from between the green and red cursors in the top panel. Single (red) and dual-exponential fit (green), along with the dual-exponential subcomponents (purple and blue) are also plotted. Time constants and fit parameters are printed in the green and red rectangles at the right.

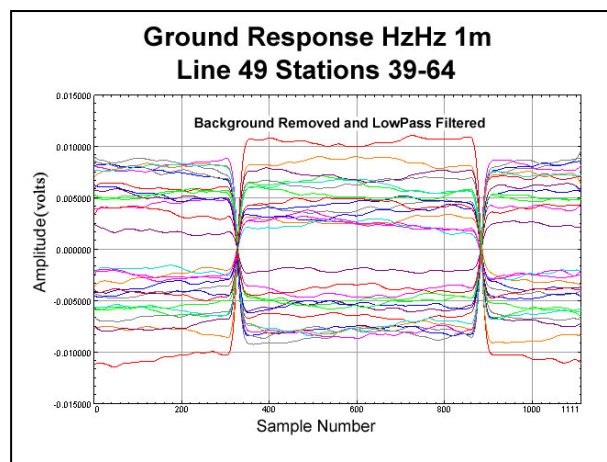


Figure 14: Ground response on Line 49.

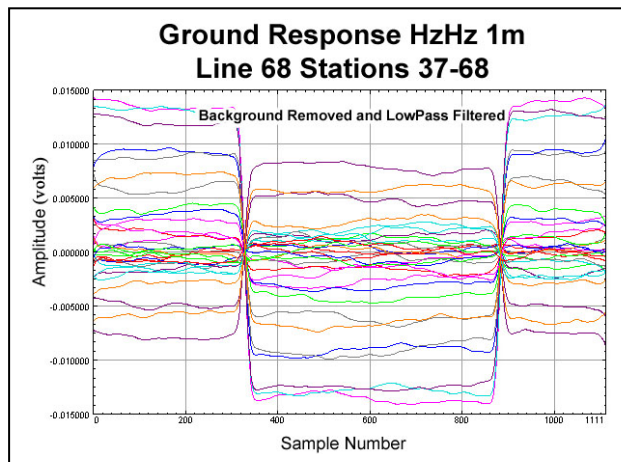


Figure 15: Ground response on Line 68.

The portion of line 68 that we ran showed a few larger amplitude deviations from the background, as seen in Figure 15. The segment of Line 68 that we chose to plot is in the area from which targets were moved. In Figure 6 this area does appear to be “bumpier” than most other target-free parts of the Calibration Grid. We speculate that this might be due to the fact that the ground had recently been disturbed leaving either modified ground conductivity, or small topographic bumps that were not particularly noticeable to the eye. We have also considered the possibility that ALLTEM might be responding to magnetic properties of the ground, but laboratory measurements we have made do not seem to indicate this. ALLTEM is responding qualitatively similarly at YPG and at the DFC and the difference is consistent with a difference in electrical conductivity of about an order of magnitude. The variable ground response can set a lower limit on our ability to detect targets and this limit might be higher than the limit that would be imposed by electronic system noise and external radio frequency interference. Since the ground response we are observing behaves like a square wave after background subtraction, it is qualitatively similar to what would be induced by errors in cancellation of the primary fields in the Rx loops. Thus it can also limit our ability to calculate accurate time constants from our data. We expect to have to account for the effects of the ground in our data inversion.

Conclusions

ALLTEM performed very well at the YPG. The ALLTEM SNR and system stability are much better than for our VETEM system when VETEM was operated with overlapped antennas at the YPG. Additionally, the sensitivity to the ground is much less than was encountered with VETEM. We now have some high quality data with multiple polarizations and we are working on methods for taking advantage of the multiple polarization data for target discrimination. The triangle wave excitation does have certain advantages including immediate visual separation of ferrous from non-ferrous targets and an ability to get good late-time SNR for ferrous targets because of their non-zero late time value when using a triangle wave excitation. We are working on system deconvolution as a step in data processing for target discrimination, but simple background removal does provide us with waveforms that can produce high quality target maps with minimal processing. Several further system improvements are planned, including mechanical enhancements. We will consider methods of accounting for the ground response of the system which involves both ground electrical conductivity and surface unevenness on the scale of the cart. We may elect to add an array of acoustic sensors to the platform to dynamically record the relationship of the cart to the ground surface. We did have a few problems with GPS, including dropouts and a less than fully adequate update rate, at YPG and are considering either upgrading the GPS or going to a laser tracking system. Much of the remaining work will be development of methods for target inversion, both adapting existing methods developed by others and developing new methods specific to ALLTEM data.

Acknowledgements and Disclaimer

This research was supported wholly by the U.S. Department of Defense, through the Strategic Environmental Research and Development Program (SERDP). We also acknowledge Yuma Proving Ground personnel and the support of several at the Aberdeen Test Center, without whose cooperation and support we could not have worked at the Yuma Proving Ground.

Any use of trade, product, or firm names in this paper is for descriptive purposes only and does not imply endorsement by the U.S. Government.

References

- Nabighian, M.N., 1979, Quasi-static Transient Response of a Conducting Half-Space: An Approximate Representation: *Geophysics*, vol. 44, p. 1700-1705.
- Smith, R., Annan, P., 1998, The use of B-field measurements in an airborne time-domain system: Part I. Benefits of B-field versus dB/dt data: *Exploration Geophysics*, vol. 29, p. 24-29.
- West, G.F., Macnae, J.C., and Lamontagne, Y., 1984, A time-domain electromagnetic system measuring the step response of the ground: *Geophysics*, vol. 49, p. 1010-1026.
- Wright D.L, Asch, T.H., Moulton, C.W., Smith, D.V., Hutton, S.R., Wallin, E., Brown, P.J., Nabighian, M.N., 2004, Test results from two prototype electromagnetic systems at the SERDP standardized UXO test site at Yuma Proving Ground, Arizona, *in* Proceedings of the Symposium on the Application of Geophysics to Engineering and Environmental Problems, February 26, 2004, Colorado Springs, CO, p. 1702-1713.
- Wright, D.L., Moulton, C.W., Asch, T.H., Hutton, S.R., Brown, P.J., Nabighian, M.N., Li, Y., 2005, ALLTEM, A triangle wave on-time time-domain system for UXO applications, *in* Proceedings of the Symposium on the Application of Geophysics to Engineering and Environmental Problems, April 3-7, 2005, Atlanta, GA, p. 1357-1367.

Numerical modeling of magnetic moments for UXO applications

Vinicio Sanchez, Colorado School of Mines

Yaoguo Li, Colorado School of Mines

Misac Nabighian, Colorado School of Mines

David Wright, U.S. Geological Survey

ABSTRACT

The surface magnetic anomaly observed in UXO clearance is mainly dipolar and, consequently, the dipole is the only magnetic moment regularly recovered in UXO applications. The dipole moment contains information about intensity of magnetization but lacks information about shape. In contrast, higher-order moments, such as quadrupole and octupole, encode asymmetry properties of the magnetization distribution within the buried targets. In order to improve our understanding of magnetization distribution within UXO and non-UXO objects and its potential utility in UXO clearance, we present a 3D numerical modeling study for highly susceptible metallic objects. The basis for the modeling is the solution of a nonlinear integral equation describing magnetization within isolated objects. A solution for magnetization distribution then allows us to compute magnetic moments of the object, analyze their relationships, and provide a depiction of the surface anomaly produced by different moments within the object. Our modeling results show significant high-order moments for more asymmetric objects situated at depths typical of UXO burial, and suggest that the increased relative contribution to magnetic gradient data from these higher-order moments may provide a practical tool for improved UXO discrimination.

Keywords: Inhomogeneous magnetization, Multipole, Magnetic moments, Numerical modeling, UXO discrimination.

1. INTRODUCTION

UXO contamination is a world-wide problem that exists not only in regions of armed conflicts, but also in countries such as Canada and USA, where it occurs in military training and firing ranges ^[1]. An estimated 15 million acres in the USA are contaminated with UXO ^[2]. With technology as of year 2001, cleaning time-frame was estimated in the decades, and cost in the tens to hundreds of billions of dollars ^[3]. Cost is mainly driven by the digging of non-hazardous materials, with as much as 70% of the UXO remediation cost taken by these operations ^[4]. False alarms can account for as much as 97% of the holes dug, in extreme cases if no effort is invested in discrimination ^[5]. This general scenario clearly points to the need in UXO discrimination work for improvements in success ratio.

Magnetic dipole and spheroids have been the fundamental models for UXO discrimination ^[6, 7, 8, 9] using magnetometry. Applicability of dipole has been justified by the magnetic response of a buried metallic object being dominated by a dipolar field. A representative example of the state of practice is work by Nelson ^[10] that used a prolate spheroid of “similar size and aspect ratio” to actual ordnance to model the induced magnetization of the objects and compared the results to actual measurements using ordnances. The discrepancies between actual measurements and modeled responses were justified by a remnant signature. Although this and similar approaches have had relative success in discrimination by recovering the information about magnetization intensity of a causative body, the dipole-based model lacks information about size, orientation, and symmetry of the body, thus hampering a more successful discrimination effort.

The asymmetry information is contained in higher-order moments. It is well known that a body bound by a second degree surface (i.e., a spheroid) is homogeneously magnetized only when oriented parallel to a homogeneous inducing field, and has a zero quadrupole moment. A more accurate representation of UXO items is a body of revolution with no fore-aft symmetry. This asymmetry implies an inhomogeneous magnetization distribution within any given UXO item and the presence of magnetic moments higher than the dipole. This has been recognized by previous studies ^[7, 11], but few quantitative analyses are available.

The variability and asymmetry of magnetization increase dramatically within irregularly shaped fragments. As a result, these items tend to possess significant higher-order moments. Although the presence of stronger higher-order moments in irregular bodies is well recognized in classical physics, little work is available in the UXO literature that quantifies the strengths and contributions of these moments. Furthermore, there has been little effort in making use of these higher moments as a means for discrimination. This is partly due to the limitations imposed by the noise level in the total-field magnetic anomalies acquired in the current UXO clearance, and partly to the lack of theoretical results on relative contribution of quadrupole, octupole, and higher order magnetic moments to the surface magnetic anomaly. Recent advances in magnetic gradiometry^[11] are expected to increase the signal-to-noise-ratio (SNR) of magnetic data significantly. The availability of such data makes it feasible to recover higher-order moments and raises the possibility of their use in UXO discrimination.

In order to lay the foundation for utilizing the high-order moments, we carry out modeling of the magnetic response for a variety of highly susceptible objects. Such objects include three-dimensional models representing UXO and non-UXO (fragment) objects. We first model the magnetization distribution within these objects using a nonlinear integral equation and then calculate the dipole and higher-order moments (quadrupole and octupole) arising from the inhomogeneous magnetization distribution. This approach accounts for the self-demagnetization effect and thus provides accurate depiction of the magnetic source in the buried objects. Based upon such modeling, analysis of the behaviour of dipole, quadrupole, and octupole fields enables us to quantify and catalogue the relative strengths of the magnetic moments for different classes of metallic objects.

In this paper, we first present the integral equation solution of magnetization distribution within highly susceptible objects. We then use this method to solve for the magnetization within different metallic objects and calculate their dipole, quadrupole, and octupole moments based on the solution. These moments are then used to study their relative contributions to surface data.

2. NUMERICAL MODELING OF 3D OBJECTS WITH HIGH SUSCEPTIBILITY

We now proceed to modeling of magnetization within highly susceptible objects. Without loss of generality, we focus on the induced magnetization. Any remanent magnetization preserves part of magnetization history and therefore has its origin in some form of induced magnetization during the formation process. The induced magnetization phenomenon occurs because the magnetic domains in a magnetic material tend to align with the direction of the inducing field^[12]. The ease with which domains align, and therefore strength of induced magnetization, depends strongly on the magnetic susceptibility of the material^[13].

Assuming a linear and isotropic material, magnetization is given by the product of magnetic susceptibility κ and total magnetic field \vec{H} ,

$$\vec{M} = \kappa \vec{H}, \quad (1)$$

where the magnetic field \vec{H} includes both the inducing field \vec{H}^0 and the secondary field produced by the magnetization distribution. The relation between magnetization and susceptibility is therefore nonlinear since the susceptible object has an anomalous field that depends on the magnetization that, in turn, is a function of \vec{H} .

In some geophysical applications susceptibility is small and the resulting secondary magnetic field is much smaller than the inducing field. In such cases, the magnetization can be approximated by the product of susceptibility and the inducing field directly. This is the Born approximation^[14]. In highly magnetic materials, however, $|\vec{H}| < |\vec{H}^0|$ because the secondary field internal to the magnetic material opposes the inducing field. Consequently, the actual magnetization is smaller in magnitude than the above approximation. This phenomenon is termed self-demagnetization^[14]. The self-demagnetization effect refers to the extent to which the induced field is reduced, due to shape of the susceptible body and orientation relative to the inducing field, by superposition of the secondary field produced by the magnetization inside the body. Because the internal demagnetization field for a magnetic body is strongly dependent on the shape of the body, approximation of the demagnetization effect for a body of irregular shape by the demagnetization of a spheroid of known demagnetization factor leads to considerable errors^[13, 15, 16, 17]. For higher susceptibility values in

a finite, non-spheroidal body the demagnetization field within the body can be strongly inhomogeneous ^[13, 15]. This magnetic phenomenon is more pronounced for bodies with large aspect ratios or highly irregular shapes.

The effect of self-demagnetization has been examined extensively in applied geophysics, especially in mineral exploration ^[18, 19]. One approach to the solution of this problem has been to compute demagnetization factors for bodies of simple shapes with analytic solutions such as cylinders ^[20], spheroids ^[21], or rectangular prisms ^[15]. More complicated objects require numerical modeling. Sharma ^[15] developed an integral equation approach for this purpose. More recently, Levievre and Oldenburg ^[22] formulated the problem using a differential equation approach. This approach is suitable for distributed susceptibility over a region. In our study, we deal with isolated, irregular objects and choose to adopt an integral equation approach following Sharma ^[15] for its simplicity.

Consider an isotropic metallic object situated in the earth's inducing field. Since the inducing field is relatively weak, the above mentioned linear relationship between the magnetization and magnetic field holds true. The total magnetic field within an object is given by,

$$\vec{H} = \vec{H}^o + \vec{H}^a, \quad (2)$$

where \vec{H}^o is the inducing field defined by the International Geomagnetic Reference Field (IGRF)^[23], and \vec{H}^a is the secondary field produced by the magnetization \vec{M} . The secondary field is given by,

$$\vec{H}^a = \frac{1}{4\pi} \iiint_V \vec{M}(\vec{r}') \nabla \nabla \left(\frac{1}{|\vec{r} - \vec{r}'|} \right) dV, \quad (3)$$

where $|\vec{r} - \vec{r}'|$ is the distance between source and observation points.

Combining Equations (1) and (3) with (2) yields an integral equation for the magnetic field,

$$\vec{H}(\vec{r}) = \vec{H}^o(\vec{r}) + \frac{1}{4\pi} \iiint_V \kappa(\vec{r}') \vec{H}(\vec{r}') \nabla \nabla \left(\frac{1}{|\vec{r} - \vec{r}'|} \right) dV, \quad (4)$$

This equation is valid for any observation point \vec{r} in the entire space, including inside the source body, whereas the integral part concerns with only the source region. Knowing the field in the source region allows the calculation of the magnetic field in the whole space. Restricting \vec{r} to be within the volume V , i.e., considering \vec{H} on both sides of eq.(4) to be the same function defined inside the source body, yields a Fredholm integral equation of the second kind ^[24]. This integral equation can then be solved to obtain the magnetic field \vec{H} inside the source body, which then defines the magnetization as a function of position within the object. For the purpose of modeling magnetic anomaly on the surface, we can proceed with eq.(3). The magnetic flux intensity measured in a magnetic survey is given by $\vec{B}^a = \mu_0 \vec{H}^a$, where μ_0 is the free-space permeability.

Eq. (4) has an analytic solution only in special cases such as when the region V is defined by a spheroid. In general, we must solve it numerically. We have chosen to use the method of moments ^[25] and a point-collocation scheme. In this approach, we discretize the source body into a set of cuboidal cells and assume that both magnetic field and magnetization within each cell is uniform and equal to that at the center of the cell. Figure 1 displays four examples of such discretized objects. The cells in these models are between 0.25-0.75cm on a side. With such a numerical discretization, the continuous integral equation takes on the following matrix form,

$$\vec{H}^m = \vec{H}^o + \frac{1}{4\pi} \sum_{s=1}^n \kappa^s \vec{H}^s \cdot \iiint_{V_s} \nabla^2 \left(\frac{1}{\vec{r}_{ms}} \right) dV_s, \quad (m, s = 1, 2, 3, \dots, n), \quad (5)$$

where \vec{r}_{ms} represents the distance between cells ‘m’ and ‘s’, and κ^s and \vec{H}^s are respectively the susceptibility and magnetic field in the cell ‘s’, and n is the number of cells in the discretized object. Eq.(5) represents a linear system of $3n$ equations and $3n$ unknowns since there are three magnetic-field components for each cell. The resulting matrix system can be solved using a number of suitable linear solvers. The obtained solution yields the values of the effective magnetization components of all the cells in the body.

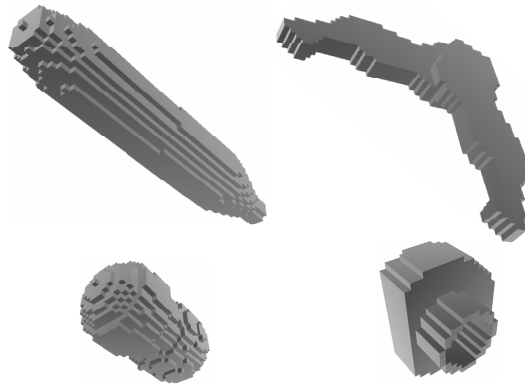


Figure 1. Examples of cuboidal models. Models are not to scale. (Top row) 81mm projectile and “boomerang”. (Bottom row) 40 mm grenade, and trimmed, hollow fragment.

Approximating a body with a set of small cuboidal prisms offers the possibility of computing the magnetization distribution for bodies of arbitrary shapes, regardless of material magnetic susceptibility. The accuracy of the solution is dependent upon cell size (thus on the fit of cuboidal-cell models to the boundaries of modeled objects), material susceptibility, and validity of the assumption of uniform magnetization within the cells. Based on these considerations, one may be tempted to approximate the object to a high degree with finer cells in order to obtain a better solution. However, there are computational aspects to consider before taking this approach. In numerically evaluating the above equations there are two fundamental issues: (1) a trade-off between accuracy in fitting the body boundary and computational cost, and (2) a rapid increase in rounding errors with increasing size of the coefficient matrix ^[26]. In other words, discretization error decreases as the number of cells increases, but both round-off error and CPU time increase with increasing number of cells. Numerical tests carried out for this study have shown that a cell size of 0.25-1.0cm produces sufficiently accurate results, and the solution can be obtained on a standard PC with reasonable amount of computational cost.

3. UNDERSTANDING RELATIVE QUADRUPOLE AND OCTUPOLE CONTRIBUTIONS

We now proceed to the evaluation of relative contributions of quadrupole and octupole moments of buried metallic objects to total-field anomaly and to gradient tensor data. We consider two general groups of objects, regularly-shaped objects without fore-aft symmetry (UXO), and irregularly-shaped non-UXO objects (fragments). We start by creating a small catalog of numerical 3D models of UXO and fragment items. This catalog includes items such as hand grenades, 40mm grenades, 60mm mortars, metallic spigots, irregular fragments, and so on. Each UXO model is axially symmetric solid of revolution created with a complete rotation of the object’s profile over the axis of symmetry. The models of fragments are either strongly asymmetric or are truncated versions of otherwise-symmetric models. All objects used in this study are assumed to be made of the same highly susceptible material. UXO as well as scrap metal are generally made of steel, whose typical susceptibility values range from several hundred to over a thousand SI units ^[27]. We have chosen to use the susceptibility value of 260 SI units for all models. The susceptibility value is of fundamental importance because, when the susceptibility is above 1.0, magnetic response of an object is strongly non-linear with respect to the susceptibility due to the self-demagnetization effect. Above about 100 SI units, however, the magnetization saturates and increasing susceptibility produces only a slight variation on the magnetic response.

For each digitized model, we first obtain the integral equation solution of magnetization under an assumed inducing field direction. We then calculate the dipole,

$$m_i^{(1)} = \iiint_V M_i dV, \quad (6)$$

quadrupole,

$$m_{ij}^{(2)} = \iiint_V (M_i x_j + M_j x_i) dV, \quad (7)$$

and octupole magnetic moments

$$m_{ijk}^{(3)} = \iiint_V (M_i x_j x_k + M_j x_i x_k + M_k x_i x_j) dV, \quad (8)$$

of the modeled objects from the magnetization distribution. Each of the three indices i, j , and k indicates the three orthogonal axis directions. The definition of multipole moments depends upon the choice of a reference point within the source body. In our work, we choose this point to be the geometric centroid of the magnetization distribution.

3.1 Comparison of a UXO and a Fragment model

To understand the contribution of the quadrupole and octupole to the surface responses, we first examine the computed total response, and its constituent components due to the dipole, quadrupole, and octupole of two highly susceptible objects. The first is an 81mm M57 projectile and the second is an irregularly shaped fragment referred to as a “boomerang” (see two top items shown in Figure 1). The projectile’s longest axis and the boomerang’s plane both lie in the horizontal plane. The projectile points towards north and the boomerang’s wings point to north and east, respectively. The magnitude of the inducing field is 50,000 nT with an inclination of 65° and declination of 25° . The horizontal measurement plane is 0.80m above the centroid of the models, and the data sampling interval is 10cm both in northing and easting directions. Plots of tensor components in this Section are arranged according to the order in the gradient tensor. The total-field anomaly is plotted, for comparison purposes, in the lower left corner of the figures.

Figures 2 and 3 show the total responses of the UXO and fragment, respectively. The total response is calculated by summing the exact fields from all cells in each model. Both data sets appear to be strongly dipolar. For the particular case of a sphere, the dipole will be oriented in the direction of the inducing field. For other object shapes, the dipole tends to align in the direction of the object’s longest axis with the deviation from this direction being larger for asymmetric objects^[9]. In these plots, therefore, it is possible to qualitatively infer a dipole oriented approximately in the north-south direction in the case of the 81mm projectile, and a dipole pointing in the north-east direction for the boomerang. However, detailed examination of the plots indicates presence of strong non-dipolar components.

Figures 4 and 5 show the dipole responses for the two objects. When comparing the signal amplitudes with those in Figures 2 and 3, it is apparent that the total response is dominated by the dipole, as expected. Table 1 shows the magnitude and orientation of the computed magnetic dipoles. Given the inducing field direction, the orientation of the dipole is closer to the direction of the longest axis in the case of the 81mm projectile. For the boomerang, however, the dipole is rotated towards the east, the orientation of the second wing.

Inducing Field: Inclination Declination	65° 25°	Dipole		
		Magnitude (Am ²)	Inclination	Declination
81mm projectile		0.452	15.5°	3.1°
Boomerang		0.244	18.1°	19.4°

Table 1. Comparison of dipole parameters for an 81mm projectile and a Fragment (boomerang)

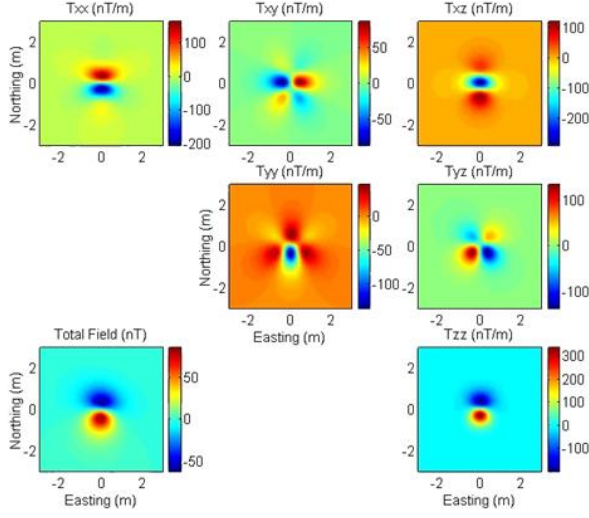


Figure 2. Total response for 81mm M57 projectile

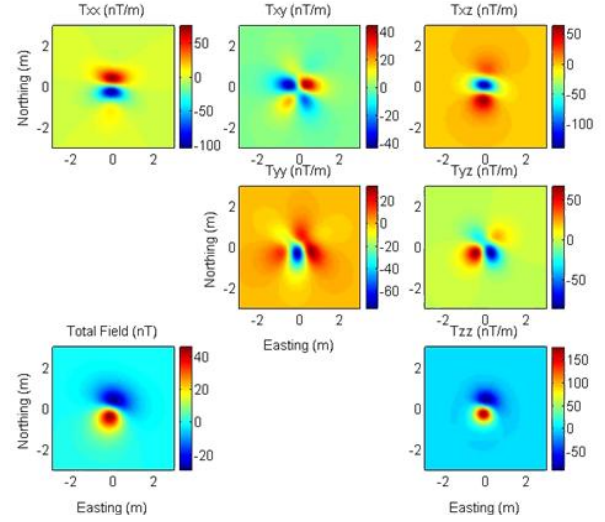


Figure 3. Total response for fragment (boomerang)

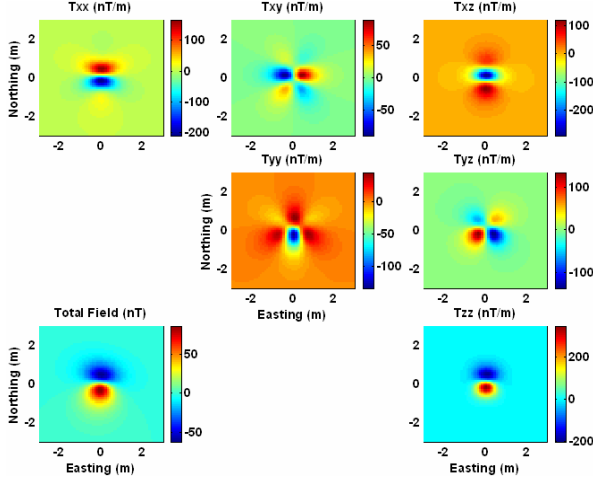


Figure 4. Dipole response for 81mm M57 projectile

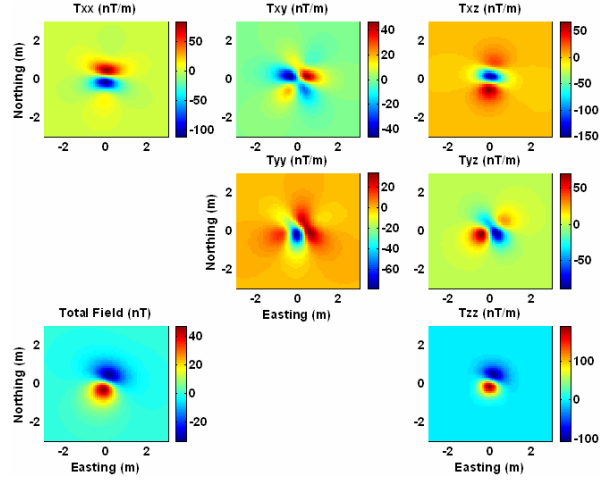


Figure 5. Dipole response for fragment (boomerang)

The volume of the boomerang is 80% of that of the 81mm projectile, but we find that the dipole magnitude for the boomerang is only 54% of the dipole magnitude for the 81mm projectile (Table 1). The main reason for this is the variable self-demagnetization in the two wings of the fragment item. One wing has a much stronger self-demagnetization effect because the inducing field is crossing that wing instead of being aligned with it. The decrease in the total strength of magnetization is reflected in the decreased dipole moment.

Figures 6 and 7 display the surface responses due to the quadrupole moment for the two objects. The fragment has larger quadrupole components than the projectile. This results in larger quadrupole contribution to the surface anomaly in the case of the fragment. This also holds true for the total-field anomaly. The highest-order moment considered in this study is the octupole. Total-field anomaly and gradient response of the octupole moment for the two items are shown in Figures 8 and 9. For the fragment the magnitude any of the octupole components is smaller than the magnitude of the largest component in the 81mm projectile, but large enough so that, combined octupole response in surface data is comparable to that from the 81mm projectile.

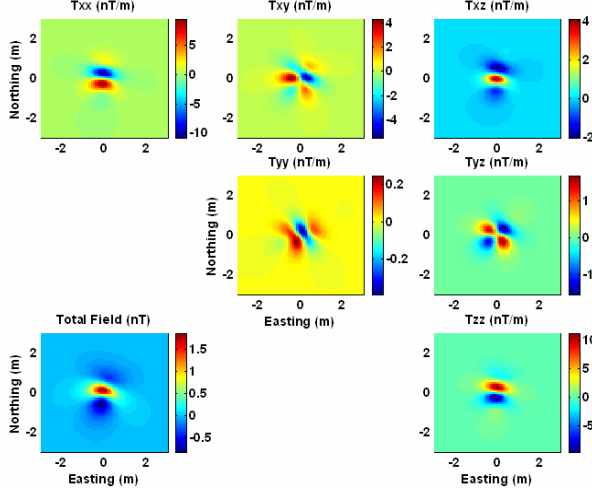


Figure 6. Quadrupole response for 81mm M57 projectile

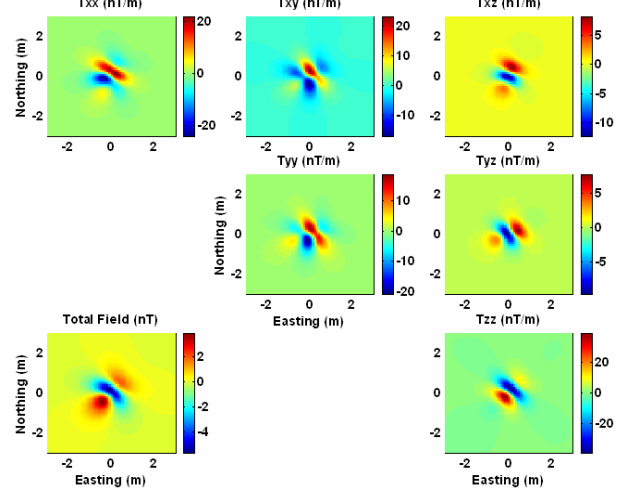


Figure 7. Quadrupole response for fragment (boomerang)

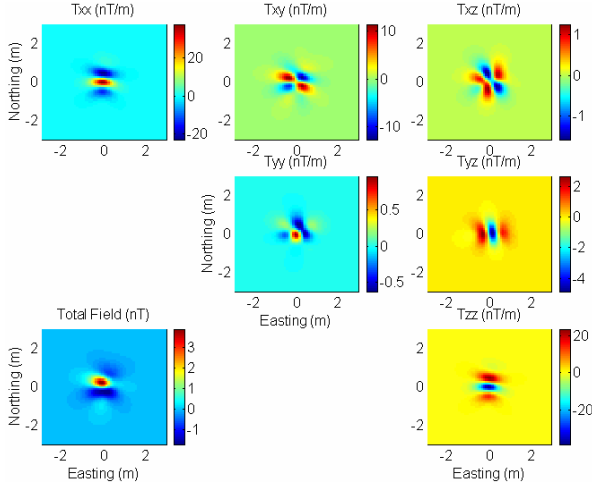


Figure 8. Octupole response for 81mm M57 projectile

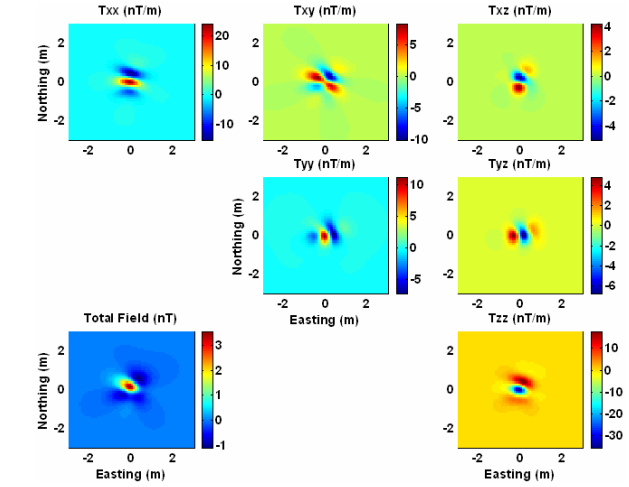


Figure 9. Octupole response for fragment (boomerang)

To quantitatively evaluate the relative strengths of the different magnetic moments and their responses, we examine the ratio of the L-2 norm of surface response maps. The quadrupole-to-dipole ratio (QDR) is defined as the quotient of L-2 norm of the quadrupole response over that of the dipole response, and the octupole-to-dipole ratio (WDR) is defined by the quotient of the norms of the octupole and dipole responses. These ratios are more useful than a simple comparison of strengths of different moments, since the responses due to different moments decay at different rate with distance from the source. Using these ratios we can catalog the objects according to the relative field strengths of different moments. For the pair of objects in question, the largest QDR for gradient data is 4.5% for the projectile and 45.9% for the boomerang. The maximum WDR is 12.2% for the projectile and 16.3% for the fragment. For the total-field anomaly the largest QDR for the projectile is 3.1% and 16.4% for the boomerang. The maximum WDR is 2.5% for the projectile and 4.4% for the fragment. This is the case for all the tested orientations of the inducing field.

From the given ratios we see first, that the fragment has significantly larger quadrupole response than the projectile, both in the total-field and the gradient data; and secondly, that the quadrupole response is higher in gradient data than in total-field data. A conservative noise level with mean zero and 2 nT of standard deviation is equivalent to about 16% of the L-2 norm of the total-field dipole response for the projectile at this depth. Thus, such a noise level reduces the chance of recovering any moment beyond the dipole. SNR for gradient data is estimated to be about twice

that for total-field anomaly data, due to the common-noise rejection features of the construction of the gradient systems. Such a noise level corresponds to 4.7% of the gradient dipole response by the L-2 measure, making it possible to recover quadrupole moments from gradient data.

3.2 Library of UXO and fragment items

To systematically investigate the magnetic moments and their field strength for different objects, we have constructed a catalog of models of UXO and fragments with regular and irregular shapes. To explore the variation of QDR and WDR for these items under different conditions, we have also computed the responses for a suite of relative orientations between the objects and the inducing field. This enables us to develop an understanding of the range of variation for these ratios. The simulation was carried out by fixing the items to lie horizontally and varying the orientation of the inducing magnetic field (defined by an inclination and declination). The magnitude of the inducing field was again 50,000 nT.

Item	Quadrupole/Dipole (2-Norm)			
	Total-Field	Magnetic Gradient		
		Minimum	Mean	Maximum
81mm M57	1.47	0.23	2.38	4.30
60mm mortar	1.49	0.24	2.28	3.97
50 cal	1.35	0.23	2.20	4.00
57mm projectile	1.58	0.25	2.11	3.54
100 series Fuze	3.32	0.81	3.30	4.96
60mm mortar (no fins)	0.82	0.20	1.02	1.68
Hand grenade	0.39	0.04	0.49	0.85
40mm grenade	0.41	0.05	0.51	0.85
Boomerang	10.60	6.77	19.38	34.32
Trimmed boomerang	8.67	5.74	16.02	26.41
Hollow spigot	3.94	0.53	4.28	6.71
Spigot	6.52	1.34	6.75	10.13
Trimmed spigot	6.11	2.35	6.48	9.61
Solid spigot	3.65	0.65	3.90	5.89
Pillbox	1.41	0.48	2.92	5.33
Fragment (trimmed and hollow)	2.40	1.74	2.54	3.45

Table 2. Comparison of quadrupole-to-dipole ratio (QDR) for UXO and non-UXO models. Inducing field has 65° inclination and 25° declination.

Table 2 summarizes the results of the computation of magnetic moments for a representative set of sixteen models, with a fixed inducing field direction having an inclination of 65° and declination of 25°. The centroid of all the objects is buried at 80cm from the closest approach to the sensor. The upper half of the Table contains UXO items. The lower half contains fragment (non-UXO) items. We compare the relative contributions of dipole and quadrupole to total-field anomaly and gradient data. The QDR and WDR are given in percentages. For the gradient data, we tabulate the minimum, mean, and maximum ratios of the five independent components. First, comparing two items with comparable volumes (240-260 cm³), the 60mm mortar without fins and the fragment (trimmed and hollow), we find that QDR for the fragment is between two and three times higher than for the mortar. Comparing the results of two items with similar dipole magnitude (~ 0.16 Am²), the 60mm mortar without fins and the spigot, we find that gradient data produce a maximum QDR of 10.1% for the fragment, which is six times the QDR of 1.7% for the UXO item. Such differences exist in general for the two classes of the items, and we can make the following important observations from the data in Table 2:

- 1) Maximum QDR is greater for gradient data than for total-field anomaly, with mean value being comparable to or larger than QDR for total-field anomaly data.
- 2) Mean and maximum QDR values are generally greater for fragments than for UXO objects. In some cases, there is an order of magnitude difference.
- 3) There is a small region of overlap for QDR between UXO and fragments. This is partly due to the fact that some fragments are only slightly asymmetric and small in size.

Although not presented here for brevity, data for WDR also show similar results and the above statements hold true as well. Thus, we find that there is a clearly definable difference in relative strengths of dipole and higher-order moment fields from UXO and fragment items. This difference is apparent in both total-field and gradient data, but it is more pronounced in the latter. Therefore, two important conclusions can be drawn from these simulations. First, the increased and detectable quadrupole responses from fragments may offer a viable tool for identifying these items. Thus it can be a potentially useful criterion for UXO discrimination. Secondly, the relative contribution of quadrupole and octupole is higher in gradient data than in total-field anomaly. This observation, coupled with the fact that gradient data have better SNR, means that gradient data would be more advantageous than total-field anomaly data if higher-order moments are used for discrimination.

To complete the simulation, we vary the inducing field direction as mentioned earlier. It is known that the strongest magnetization is obtained for objects with the largest aspect ratios when the inducing magnetic field is parallel to the longest axis of the body, which is the direction of weakest self-demagnetization effect. In contrast, an inducing field perpendicular to the longest axis of an object would induce the weakest dipole moment in that object. Figures 10 and 11 display ranges of the QDR and WDR for gradient data for a variety of assumed inducing field directions. All simulations use a constant ratio of closest approach to body length. Figure 10 shows that the conclusions obtained from Table 2 hold true for different orientations between the inducing field and modeled objects, i.e., the relative contribution of the quadrupole in a UXO to the surface measurements is small in comparison to that from a non-UXO object. This observation is valid even for the case of weakest magnetization when the inducing field is perpendicular to longest axis of the body. There is no significant overlap in the range of variation for UXO and fragments. Figure 11 shows a smaller relative contribution of the octupole for UXO objects than for non-UXO objects. The ranges of variation of this contribution only show a larger overlap between UXO and non-UXO objects for the special case of vertical inducing field. This agrees with the stated results earlier about axially symmetric objects having a small quadrupole but possibly important octupole.

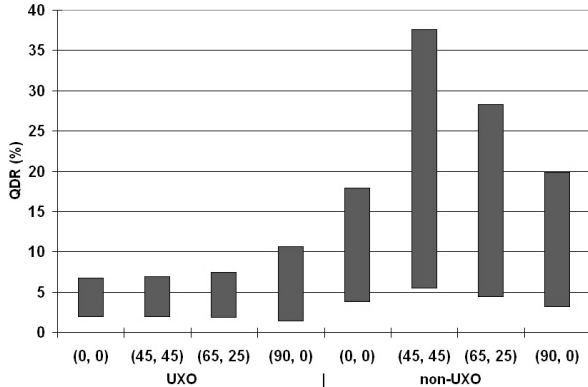


Figure 10. Range of quadrupole-to-dipole-ratio (QDR) for UXO and non-UXO items for different inducing field directions (inclination, declination).

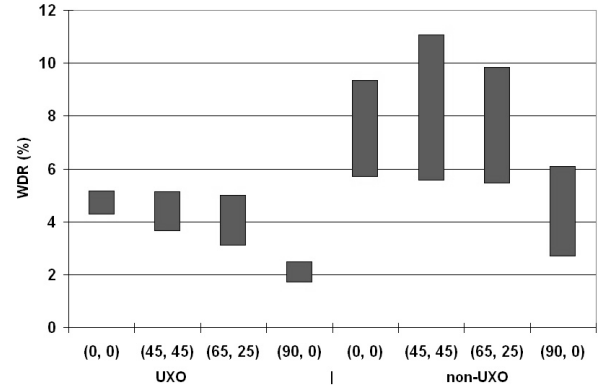


Figure 11. Range of octupole-to-dipole-ratio (WDR) for UXO and non-UXO items for different inducing field directions (inclination, declination).

4. CONCLUSIONS

We have presented an approach to numerical modeling of magnetization in highly susceptible UXO and non-UXO objects and its use in understanding the strengths and relative contributions of various magnetic moments in these objects. The magnetization is obtained by solving an integral equation that describes the self-demagnetization process within confined objects. The dipole, quadrupole, and octupole moments with respect to an object's centroid point are then calculated from the solved magnetization distribution. Such decomposition enables us to investigate the feasibility of using higher-order magnetic moments in UXO discrimination.

We find that there is a significant difference in the relative contributions of quadrupole responses from UXO and non-UXO objects. The relative contribution of the quadrupole from UXO items is in general much smaller than from non-UXO objects. The ranges of variation for the two classes of items have a small overlap. Furthermore, the quadrupole

component is relatively stronger in gradient data than in total-field magnetic data. We find that the contribution of the octupole is also important for non-UXO objects. Therefore, we conclude that there is a potential to improve the UXO discrimination effort by utilizing higher-order moments, and that the newly available tensor gradient data provide a viable opportunity for recovering quadrupole moments to be used in discrimination work.

5. ACKNOWLEDGEMENTS

This work was funded by the Strategic Environmental Research and Development Program (SERDP) under project **UX-1328**.

6. REFERENCES

- [1] Billings, S. D., “Discrimination and classification of buried unexploded ordnance using magnetometry”. IEEE Transactions on Geoscience and Remote Sensing, V. **42**, N. 6, June 2004
- [2] FAC. “Unexploded ordnance (UXO): An overview”. Fed. Advisory Comm. Development of Innovative Technologies, Washington, DC. 1996.
- [3] Committee on the Budget. “Environmental liabilities, DoD training range cleanup cost estimates are likely underestimated”. U.S. GAO, Committee on the Budget, House of Representatives, Washington, DC, Report to the Chairman, April, 2001.
- [4] Potter, John. “UXO Identification and Discrimination: View from the Field”. Presented at the Third Annual SERDP Symposium, December 3-5, 1997.
- [5] Putnam, J., “Kaho’olawe program management and technology”. In Proceedings, UXO Forum, New Orleans, LA. April, 2001.
- [6] McFee, J. E., “Electromagnetic Remote Sensing: Low Frequency Electromagnetics”. DRES Special Publication SSP 124. Defence Research Establishment Suffield Ralston, Alberta. pp.19-21. 1989.
- [7] Altshuler, T. W., “Shape and orientation effects on magnetic signature prediction for unexploded ordnance”. In *Proc. UXO Forum*, pages 282–291. 1996.
- [8] Butler, D. K., Cespedes, E. R., Cox, C. B., Wolfe, P. J.. “Multisensor methods for buried unexploded ordnance detection, discrimination and identification”. Technical Report 98-10, SERDP, September 1998.
- [9] Billings, S. D., Pasion, L. R., Oldenburg, D. W., “Discrimination and Identification of UXO by Geophysical Inversion. Phase II: Inversion of Total-Field Magnetics Final Progress Report”. GIF-University of British Columbia. April 9, 2002.
- [10] Nelson, H. H., Altshuler, T. W., Rosen, E. M., McDonald, J. R., Barrow, B., Khadr N., “Magnetic modeling of UXO and UXO-like targets and comparison with signatures measured by MTADS”. *Proc. UXO Forum*, pp. 282–291, 1998.
- [11] Doll, W. E., Gamey, T. J., Beard, L. P., Bell, D. T., “Airborne vertical magnetic gradient for near-surface applications”. The Leading Edge. Society of Exploration Geophysicists. 2006.
- [12] Jackson, J. D., *Classical electrodynamics*. Third Edition. John Wiley & Sons, Inc. 1999.
- [13] Aharoni, A., *Introduction to the theory of ferromagnetism*. Oxford Science Publications. International Series of Monographs on Physics. **93**.1996.

- [14] Born, M., *Principles of optics: Electromagnetic theory of propagation, interference and diffraction of light*. 7th Edition. Cambridge University Press. 1999.
- [15] Sharma P. Vallabh., “Rapid computation of magnetic anomalies and demagnetization effects caused by bodies of arbitrary shape”. *Pure and Applied Geophysics*. **64**. pp.89-108. 1966.
- [16] Sharma, P. Vallabh. “Short Note: Demagnetization effect of a rectangular prism”. *Geophysics*. **33** (132-134). 1968.
- [17] Eskola, T., Tervo, T., Puranen, R., “Calculation of magnetostatic anomalies and demagnetization factor by means of the method of subareas”. *Geol. Surv. Finland, Rep. Invest.* **16**. 1977.
- [18] Lee, T. J., “Rapid computation of magnetic anomalies with demagnetization included, for arbitrarily shaped magnetic bodies”. *Geophys. J. R. Astr. Soc.* **60**, p.67-75. 1980.
- [19] Traynin, P., Hansen, R. O., “Magnetic modeling for highly permeable bodies with remanent magnetization”. *63rd Ann. Internat. Mtg. Soc. of Expl. Geophys.*, pp.410-413. 1993.
- [20] Bozorth, R. M., Chapin, D. M., “Demagnetization factors of rods”. *J. Appl. Phys.* **13**, 320. 1942.
- [21] Stoner, E. C., Demagnetization factors for ellipsoids. *Phil. Mag.*, V.**36**, pp.803.2. 1945.
- [22] Levievre P. G., Oldenburg, D. W., “Magnetic forward modeling and inversion for materials of high susceptibility”. *Society of Exploration Geophysicists. Expanded Abstracts*. 2002.
- [23] International Geomagnetic Reference Field (IGRF), <http://swdcwww.kugi.kyoto-u.ac.jp/igrf>. 2005.
- [24] Kaufman, A. A., *Geophysical field theory and method, Part A*. Academic Press. San Diego, California. 1992.
- [25] Harrington, R. F., *Field computation by moment methods*. The Macmillan Company, New York. 1968.
- [26] Wilkinson, J. H., “Error analysis of direct methods of matrix inversion”. *J. Assoc. Comput. Machines*. **8**, 281. 1961.
- [27] Lide, D. R., *CRC hanbook of chemistry and physics*. CRC Press, 82 edition. 2001.